Ayaz Arif Khan

Dielectric reliability and spin dependent transport in Co-Fe-B/MgO/Co-Fe-B magnetic tunnel junctions

Bielefeld University

Reviewers:
Prof. Dr. Günter Reiss
Prof. Dr. Walter Pfeiffer

BIELEFELD UNIVERSITY, DEPARTMENT OF PHYSICS
THIN FILMS AND PHYSICS OF NANOSTRUCTURES

Ph.D. thesis

First printing, March 2011

Contents

Declaration

I hereby declare that this submission is my own work and that, to the best of my knowledge and belief, it contains no material previously published or written by another person nor material which to a substantial extent has been accepted for the award of any other degree or diploma of the university or other institute of higher learning, except where due acknowledgment has been made. Text and figures were partly taken from the corresponding publication originate directly from this work.

A. A. Khan
Bielefeld University

Acknowledgement

It is a genuine pleasure to express my gratitude towards the individuals who supported and motivated me during this work. To begin with, I am immensely grateful to my supervisor Dr. Jan Schmalhorst and Prof. Günter Reiss for their constant encouragement and continuous support, for believing in my abilities right from the beginning and giving me an opportunity to work in his group. Jan Schmalhorst has been a patient and kind teacher who has Inspired the essential aspects of a good researcher in me. I have learned greatly from his straightforward approach to research. I would like to acknowledge the university of Azad Jammu and Kashmir Muzaffarabad for financial support.

I am very grateful to Prof. Markus Münzenberg (Göttingen University) for the HRTEM measurements and for a fruitful collaboration. These measurements proved indispensable to this thesis.

My sincere thanks to Prof. Dr. Andreas Huetten and P. D. Dr. Andy Thomas for their support and discussion at the early stage of this work. A note of deep appreciation to my office mates Dr. Camilia Albon and Dr. Karsten Rott. Thanks to their sense of humor, their patience with my numerous phone conversations to Pakistan, we shared innumerable laughs together.

My genuine thanks and appreciation to individuals (Oliver, Drewello, Danial, Volker Höink, Camilia, Karsten) who introduced me to the deposition and measurement equipment, used in this work. A word of thanks to A. G Venkatesh for making available his expertise on bonding the sample for measurement and the accompany we had at late hours while performing our individual experiments specially on weekends. I am rarely grateful to each

and every one of them. A word of thanks to all of my colleagues and friends for their friendship, their support, their encouragement, and their help in maintaining my sanity. I would also like to thank administrative staff for their support. Aggi Windmann our favorite secretary, deserves a special mention for taking care of all my office related issues. A word of thanks to the administrative staff of UAJK Muzaffarabad for taking care of all my scholarship related issues.

I am forever grateful to my parents. They always worked hard to support me during my studies. I would like to thanks my sisters for her prayers, my uncles and cousins for their moral support. I wish to express my love and gratitude to my daughter Zukhruf Ayaz and my son Ammar Ayaz who sacrificed my presence during my stay in Bielefeld, Germany. I am eternally indebted to my wife whose moral support, exemplary patience and prayers have sustained me to complete this work.

Finally, Bielefeld is a beautiful city. One can enjoy here the life of a village and a city at the same time. Now the time is coming closer to leave this nice city and I have good feelings to find my new ways and sadness to leave Bielefeld.

1

Introduction

The experiments described in this thesis relate to the recently emerging and rapidly growing field of spin electronics or spintronics. This area of study allies electronics and magnetism. It uses the spin of the electron to obtain new proporties or functions. These developments concern a new type of non-volatile memories. In contrast, conventional electronics is based on the use of an electric field to act on the charge of electrons. The electronic spin gives rise to the magnetism of solids, but also provides a means to influence the electrons by a magnetic field. Thus, in ferromagnetic (FM) materials, the motion of an electron depends on its spin orientation with respect to local magnetization. This gives rise to interesting new effects to the field of spintronics.

Spintronic effects occur on a length scale in which spin is conserved, called the spin diffusion length, which is of the order of a few nanometers. Another milestone in the spintronic was the observation of the tunnel magnetoresistance effect in magnetic tunnel junctions which have a thin layer of an insulating material sandwich between two FM materials as shown in Fig. 1. The dielectric reliability of the insulating layer is a major reliability concern in spintronic devices. Currently, the understanding of materials, physics, and reliability at the nano, or atomic, level is vital to the proper design and manufacturing of these devices.

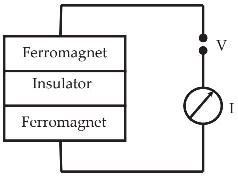

Figure 1: Schematic illustration of a magnetic tunnel junction.

1.1 Spintronics: Historical overview

Spintronics is a novel research field involving the study of active control and manipulation of spins in solid state systems[1]. The emerging spintronics technology may offer higher density of integration, nonvolatility, faster operating speed and lower power consumption compared to traditional semiconductor technology.

Until now, the most significant success in spintronics was achieved in high capacity hard disk drives, particularly, in continuing advances in read head sensor technology. The spintronic effect that played a primary role in their success is known as giant magnetoresistance (GMR). It was first reported in 1988 by two European research groups independently: one led by[2] Albert Fert in France and the other by[3] Peter Grünberg in Germany. The discovery of GMR promptly triggered marvelous research efforts on magnetoelectric multilayers and devices. The physics behind today's fast expansion of spin electronics has also been known for quite some time. The cornerstone is the 'two currents' conduction concept proposed by Mott[4] and used by Fert and Campbell[5] to explain specific behaviours in the conductivity of the ferromagnetic metals such as Fe, Ni, Co and their alloys. Historically, advances in magnetoelectric devices have been attributed to new discoveries and evolutionary improvements in magnetoresistance (MR). A sensing device with a higher MR ratio can detect weaker and smaller signals. This is key to higher capacity and performance.

In 1990, materials exhibiting GMR over a range of $5-20\%$ at low fields (spin valve) were developed to make ultrasensitive magnetic field sensors. They came into use in computer hard drive (HDD) read heads in 1998, thus marking the first industrial application of spintronic components. Currently, the principal application of spintronic devices is magnetic data storage, with an information density growth rate faster than that corresponding to Moore law[6]. Another milestone in spintronics was the observation of the tunnel magnetoresistance (TMR) effects in magnetic tunnel junctions at room temperature. The effect was first observed in 1975 by a French scientist, Michel Jullière, at low temperatures in semiconducting magnetic junctions based on Germanium[7]. However, interest in tunnel junctions really took off only after 1995 when

[1] S. A. Wolf et al., Science **294**, 1488 (2001); I. Zutic et al., Rev. Mod. Phys. **76**, 323 (2004); and P. Seneor et al., J. Phys.: Condens. Matter **19**, 165222 (2007)

[2] M. N. Baibich et al., Phys. Rev. Lett. **61**, 2472 (1988)

[3] G. Binasch et al., Phys. Rev. B **39**, 4828 (1989)

[4] N. Mott, Adv. Phys. **13**, 325 (1964)

[5] A. Fert et al., Phys. Rev. Lett. **21**, 1190 (1968)

[6] from the introduction of GMR read-heads in 1997 to 2007 a 17 month doubling of data storage density was registered, increasing from approximately 1 to 600 Gbit/in^2

[7] M. Julliere, Phys. Lett. **54A**, 225 (1975)

tunnel magnetoresistance was observed at room temperature in alumina-based amorphous junctions, which displayed magnetoresistance amplitudes of up to 81%[8]. As the TMR ratio exceeded the GMR ratio, HDD companies began developing TMR based read heads. In 2004, Seagate Technology announced the first HDD product equipped with TMR read heads (utilizing TiO_x as a tunnel barrier). Now, many HDD products incorporate TMR read heads with AlO_x, or MgO as a tunnel barrier. However, the TMR ratio applied to this first generation MRAM is not high enough for next-generation applications. Much higher TMR ratios are required to achieve higher densities and faster data sensing, particularly when the MTJs are integrated into leading silicon technologies. To realize the next generation HDD drive with density greater than 1000Gb/inch^2, enormous progress has been made in the materials used to make the tunnel barrier. Thanks to recent progress in ultra-thin film science and engineering, a more promising barrier material (MgO) has been discovered and has advanced quickly, now poised for the next generation spintronic applications.

1.1.1 *Evolution of TMR effect in magnetic tunneling junctions*

Tunnel magnetoresistance has a history longer than GMR. This subsection provides an overview of the evolution of TMR in MTJs. The MTJ is a multilayered thin film structure, composed of a stacked inner hard ferromagnet, followed by an insulator and completed by an outer soft ferromagnet or vice versa. As discussed in previous subsections, the first ever realised MTJ was a Fe/Ge/Co hybrid heterostructure. Subsequently the use of amorphous alumina (Al_2O_3) allowed it to achieve much higher TMR at room temperature(RT). Many groups have steadily improved the properties of Al-O-barrier MTJs since these first RT demonstrations. The TMR ratio monotonically increased year by year and reaching a maximum amplitude of about 81% in 2007, as shown in Fig. 2. During the process of increasing the TMR ratio, theoretical studies on spin dependent tunneling on MTJs found that the TMR ration became much higher than that predicted by Jullière's phenomenological model when the tunneling was co-

[8] H. X. Wei et al., J. Appl. Phys. **101**, 09B501 (2007)

herent[9]. For perfectly ordered (001) oriented Fe/MgO/Fe MTJ, the first principle calculation predicted that the TMR ratio could reach several 1,000%. This stimulated tremendous activity in the experimental investigation of electronic and magnetic properties of MgO based MTJs. Immediately following their predictions, Bowen *et al.*[10] were the first to obtain a relatively high MR ratio in Fe(001)/MgO(001)/Fe(001) MTJs at RT (30%), but the room temperature MR ratios obtained in MgO-based MTJs did not exceed the highest obtained in Al-O-based MTJs. The main difficulty at this early stage of experimental attempts was the fabrication of an ideal interface structure. It was experimentally observed that Fe atoms at the Fe(001)/MgO(001) interface were easily oxidized[11]. Theoretically, it was found that when there were excess oxygen atoms in the interfacial Fe monolayer, the Fe states do not couple with the respective MgO states effectively. This prevents coherent tunneling of respective states and significantly reduces the MR ratio. Thus, coherent tunneling is very sensitive to the structure of barrier/electrode interfaces. Oxidation of even a monolayer at the interface significantly suppresses the TMR effect. Later on this problem was resolved using an ultrahigh vacuum thin film deposition system.

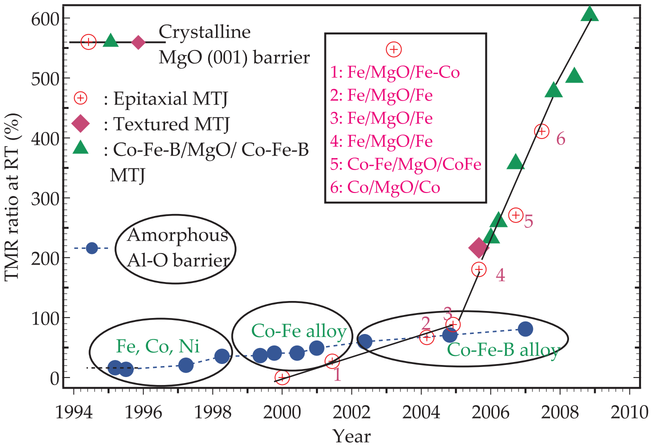

Figure 2: History of improvement in MR ratio with different ferromagnetic electrodes at room temperature (RT).

After a number of initial efforts to observe the enormous selectivity of the wave function symmetry in epitaxial junctions, two

[9] W. H. Butler et al., Phys. Rev. B **63**, 054416 (2001)

[10] M. Bowen et al., Appl. Phys. Lett. **79**, 1655 (2001)

[11] H. L. Meyerheim et al., Phys. Rev. Lett **2001**, 076102 (87)

breakthroughs were reported. One for epitaxial (001)-oriented Fe/MgO/Fe junctions[12] and the other for highly-textured sputtered Co-Fe / MgO / Co-Fe[13], showing TMR ratios of 180 and 220% respectively, thereby substantially exceeding the magnetoresistance of AlO_x based devices. Since then, the TMR reported for MgO based MTJs has steadily improved, in particular by using ternary Co-Fe-B alloys as ferromagnetic electrodes (see Fig.2)[14]. It is believed that high-quality MgO can be adequately stabilized between the as grown, amorphous Co-Fe-B electrodes, which, after annealing at temperature of almost 400^0 C, crystallize in the required bcc structure and are found to produce even higher TMR values by sputtering deposition at RT.

Currently, MTJs with an MgO barrier and Co-Fe-B electrodes are the most promising candidates for high density MRAM, because they have very high TMR ratios, probably because of the spin filtering effect originally predicted for fully epitexial Fe/MgO/Fe junctions. By far, the highest TMR ratios were reported by S. Ikeda et al.[15] (604% at room temperature and 1,144% at 5 K) in pseudo-spin valve MTJs. These MTJs are of great importance not only for device applications but also for clarifying the physics of spin-dependent tunneling. This is the subject of the present thesis.

1.1.2 *Applications*

The principal application of spintronic devices is magnetic data storage. Data sensing, or storage capacity of spintronic devices, link with magnetoresistance at room temperature. AMR devices having an MR effect of 1-2% at RT were used in the read head of HDD in the beginning. However, this application was to be short lived as in 1997 it was unseated by spin valve technology (low-field giant magnetoresistance). GMR spin-valve devices have MR ratios of 5-15% at RT and were used in the read heads of HDDs. This new read/write head was more sensitive than the AMR head used in many hard drives, despite the emergence of tunnel magnetoresistance (TMR) heads. In the next phase, Al-O-based MTJs had MR ratios of 20-70% at RT and have been used not only in HDD read heads but also in MRAM cells.

MgO-based MTJs have MR ratios of 150-600% at RT and are

[12] S. Yuasa et al., Nat. Mater **3**, 863 (2004)

[13] S. S. P. Parkin et al., Nat. Mater. **3**, 862 (2004)

[14] D. D. Djayaprawira et al., Appl. Phys. Lett. **86**, 092502 (2005)

[15] S. Ikeda et al., Appl. Phys. Lett. **93**, 082508 (2008)

expected to be used in various spintronic devices such as HDD read heads, spin-transfer MRAM cells[16] and novel microwave devices[17]. An overview of the application of spintronic devices is given in Fig. 3

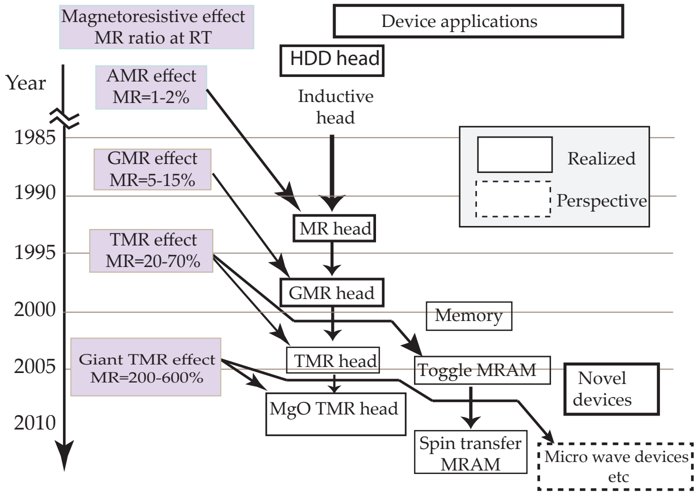

Figure 3: History and future prospects of MR ratio at room temperature and applictions of MR effect in spintronic devices. The Image taken from Yuasa et al. [J. Phys. D: Appl. Phys. 40, 337 (2007).].

1.2 This thesis

This thesis presents work conducted over the last three years. It covers several aspects of magneto-transport properties in Co-Fe-B/MgO/Co-Fe-B magnetic tunnel junction. The aim of this thesis was twofold. First, it was to investigate the dielectric reliability of MTJs under voltage stress. Since these MTJs are expected to be used in spin-transfer MRAM cells, which face several challenges for commercialization, one in particular relates to the magnetic switching issue. Recently, useful writing schemes (spin transfer switching) which enhance scalability, have been demonstrated. Thus, most of the switching schemes require a high current that flows through the MTJ. As such, the dielectric breakdown of magnetic tunnel junctions has become one of the crucial factors for MTJ-based applications. Second, I investigated the physics of spin dependent transport for this junction in order to improve the fu-

[16] J. Slonczewski, J. Magn. and Magn. Mater. **159**, L1 (1996)

[17] A. A. Tulapurkar et al., Nature **438**, 339 (2005)

ture performance of these devices.

The organization of the thesis is as follows. Chapter 2 provides an overview of the basic concept needed to understand the main physical phenomena involved in MTJ operation. Chapter 3 describes the growth of magnetic tunnel junction including growth techniques used, sample layer stacks, lithography, junction micro fabrication and characterization techniques. The intent of this chapter is that readers familiar with the deposition technique utilized be able to follow the complete experiments in the following chapters. The next chapters focus on specific research topics. Chapter 4 discusses the dielectric breakdown in MTJs. To better understand the microscopic mechanism of dielectric breakdown, the results has been analyzed in term of various expression for voltage dependent probability of breakdown. Both the E and 1/E models proposed in the literature were discussed, and both were found to yield a good description of the data in high field range where accelerated tests were performed. Chapter 5 describes the temperature dependence of the tunnel magneto resistance effect. We have demonstrated that direct spin polarized and magnon-assisted tunneling can explain the bias voltage and temperature-dependent transport properties for a barrier thickness of 1.8 nm. When increasing the barrier thickness, it was found that the results could not be interpreted based on the magnon assisted tunneling model alone. Instead, thermally or bias voltage activated additional unpolarized conductance contributions needed to be included. Inelastic processes in these junctions were studied using inelastic electron tunneling spectroscopy (IETS) measurements, which is the subject of chapter 6.

The appendix includes further details of the mathematical equations of the breakdown models, a brief overview of the analysis of temperature dependence in unpolarized conductance in magnetic tunnel junctions, a list of references, ordered alphabetically by first author, as well as a list of publications which I have (co-)authored.

2

Spin polarized tunneling: A review

In this chapter a tutorial overview of the fundamental physics behind tunneling, in particular focusing on spin-dependent tunneling, is presented to provide a coherent background of the experimental work presented. No attempt will be made to be complete or exhaustive. Instead , the reader is referred to suitable reviews.

2.1 Electron tunneling in thin films system

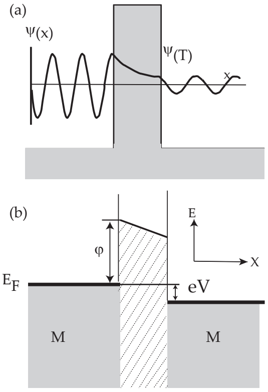

Figure 4: Tunneling in M/I/M junction. (a) Electron wave function decays exponentially in the barrier region. (b) diagram of a M/I/M structure with applied bias eV.

Electron tunneling is purely a quantum-mechanical phenomenon in which an electron can pass from one conducting electrode through an insulating layer into a second conducting electrode. The fact that an electric current can flow through an insulating layer, a concept forbidden in classical physics, is a direct consequence of the wave like nature of electrons in the quantum mechanical framework.

Generally, the tunneling process is described as a transmission probability of particles (e.g. electrons passing from one to another electrode) through a potential barrier (e.g. a thin film of insulating material like AlO_xor MgO).

A simple way to understand how tunneling is possible is by considering an electron wave which encounters a potential step, see Fig. 4. Though most of the intensity is reflected at the potential step, a portion decays exponentially through the barrier. For a sufficiently thin barrier, some intensity remains on the other side, and therefore, the electron will have the finite probability of being found on the other side of barrier. The most straightforward realization of this is a metal/ insulator/ metal (M/I/M) trilayer structure, commonly called tunnel junction.

In most studies, the tunneling phenomenon in M/I/M tunnel junctions are studied by observing the current (or its derivatives) as a function of applied voltage across the junction. As an illustration, an idealized junction has been consider, with an electrode-barrier system modeled as a step potential (Fig. 4b). Without the voltage across the junction, the two metals are in equilibrium, and the Fermi levels will be at the same energies for the two electrodes. When the bias V is applied across the junction, one Fermi level will be shifted by eV with respect to the other, where e is the electron charge. The number of electrons tunneling from one electrode to the other is given by the product of density of states at a given energy in the left electrode ,ρ_1, and the density of states at the same energy at the right electrodes, ρ_2, multiplied by the square of the matrix elements $|M|^2$. Essentially, this is the probability of transmission through the barrier. Furthermore, one has to take into account the probability that the states at the left electrode are occupied, described by the Fermi-Dirac function f(E), and the probability that the states at the right are empty, [1-f(E + eV)]. This results in a tunneling current, given by

$$I_{1\to 2} = \int_{-\infty}^{\infty} \rho_1(E).\rho_2(E+eV).|M|^2.f(E)[1-f(E+eV)]dE \quad (1)$$

One simple way to solve equation 4 has been shown by Simmons[18]. As an approximation of an arbitrary barrier, he assumed a rectangular energy barrier of mean height. Then, he used a step-function, i.e. the Fermi-Dirac function at T = 0K, and the WKB approximation (named after Wenzel-Kramers-Brillouin) to obtain the matrix elements of $|M|^2$. Simmon's approach only takes into account a symmetric M/I/M system with the same material and density of states on both sides. This simple model was extended by Brinkman et al.[19] describing an asymmetric M/I/M junction by using an additional asymmetry parameter $\Delta\varphi$. Neither of these models considers the dependence of the transport characteristics on the electronic density of states (DOS) in the electrodes. However, the simplified models of Simmons and Brinkman can qualitatively describe the experimentally observed I-V characteristics in spin-dependent tunneling elements at least for small bias voltage.

[18] J. G. Simmons, J. Appl. Phys. **34**, 1793 (1963)

[19] W. F. Brinkman et al., J. Appl. Phys. **41**, 1915 (1970)

2.2 *Spin-dependent tunneling*

As discussed before, electrons can tunnel through a thin insulator according to the law of quantum mechanics. Regarding the spin of these tunneling electrons, it is assumed to be conserved if the electron tunnels elastically. Spin dependent tunneling becomes important in the case of magnetic tunnel junctions (MTJs), where the insulator is sandwiched between two ferromagnets, as shown in Fig. 5.

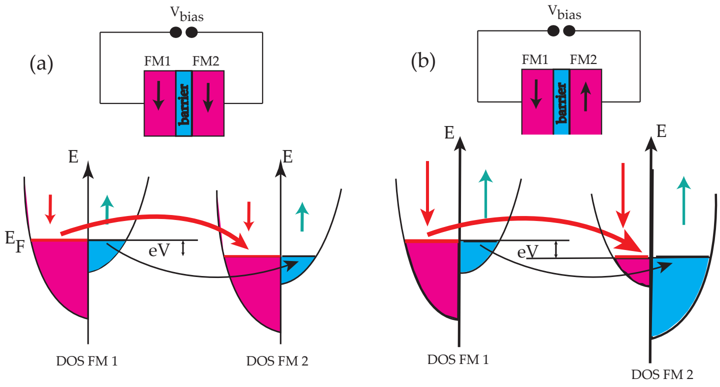

Figure 5: Schematic illustration of the physics behind TMR. (a): for parallel aligned magnetization as sketched in the left-bottom, electrons at the Fermi level with spin-up (↑) and spin-down (↓) are allowed to tunnel from majority to majority bands, and from minority to minority bands. (b): when the magnetization of the two ferromagnets is anti-parallel, tunneling takes place from majority to minority and from minorityto majority bands, leading to a reduction of total tunneling current. In terms of electrical resistance, this corresponds to a higher resistance when the magnetization of the two layers are oppositely aligned.

In such a device, the magnitude of the tunneling current depends on the relative orientation of the magnetization of both electrodes. When the magnetization of the two electrodes is aligned in parallel, a large current flows, while an anti-parallel alignment of the two electrodes results in a small current.

This can be understood from a few elementary arguments. (i) The tunneling current is in first order proportional to the product of the electrode's density of states at the Fermi level [N(E_F)]. (ii) In a ferromagnet, the ground-state energy bands in the vicinity of the Fermi level are shifted in energy due to exchange splitting, yielding unequal majority and minority bands for electrons with opposite spins. (iii) Assuming spin conservation for the tunneling electrons, there are two separate currents of spin up and spin down character. As a result, the current between electrodes with the same magnetization direction should be higher than for oppositely magnetized electrodes. This is further illustrated in bottom the panel of Fig. 5. Within this simple Jullière model[20], the resistance change is called tunneling magnetoresistance, and is given by:

$$TMR = \frac{R_{AP} - R_P}{R_P} = \frac{2P_1P_2}{1 - P_1P_2} \tag{2}$$

$P_{1,2}$ is the tunneling spin polarization determined by the relative difference in DOS at the Fermi level (for each electrode). However, it is important to note that not all electrons present at the Fermi level can efficiently tunnel through the barrier. This simple equation is not able to capture the physics behind a number of observations in MTJs. As we shall see later, the spherically symmetric s-like electrons have a much lower DOS at the Fermi level, and can dominantly tunnel through the barrier. The interface between the insulating tunnel barrier and the ferromagnets play an essential role. Nonetheless, this expression clearly demonstrates the presence of a magnetoresistance effect, and the relevance of the magnetic character of the electrodes.

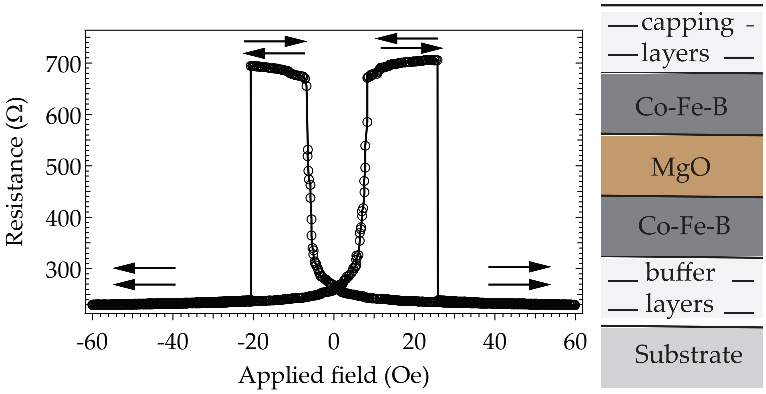

Figure 6: Resistance change in a magnetic tunnel junction consisting of Co-Fe-B(1.5 nm) / MgO(2.1) / Co-Fe-B(4 nm) as shown at right. The data are taken at room temperature. The arrows at left indicate the orientation of the Co-Fe-B magnetization.

An important characteristic marking the presence of magnetoresistance is the ability to independently manipulate the direction of the magnetization of the electrodes. In other words, to have easy access to a parallel or anti-parallel configuration of the two magnetic electrodes. This can be accomplished by a number of

[20] M. Julliere, Phys. Lett. **54A**, 225 (1975)

methods, although in this thesis two methods are used to change the hysteresis loop of one magnetic electrode in comparison to the other. The easiest method is to use two different thicknesses for the two electrodes [see Fig. 6]. This renders two different coercivities and switching fields.

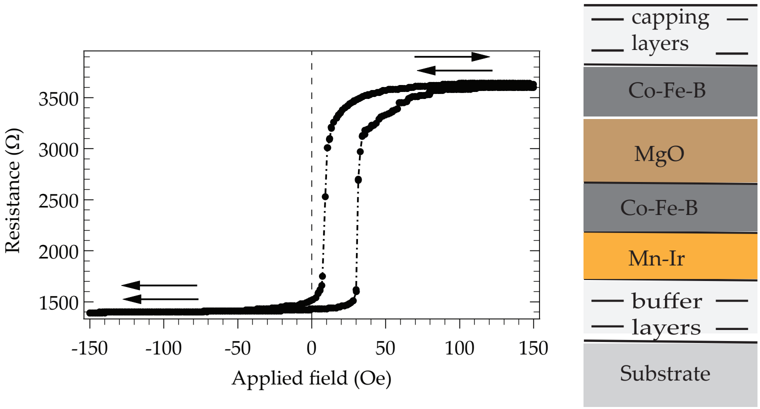

Figure 7: Resistance change in a magnetic tunnel junction whose bottom electrode is pinned by an anti-ferromagnetic Mn-Ir layer. The arrows at left indicate the orientation of the Co-Fe-B magnetization.

Another method commonly used is to fix or pin the direction of one of the ferromagnetic layers with an anti-ferromagnet like Mn-Ir. In this case, the hysteresis loop of the pinned layer shifts away from zero (see Fig. 7). This allows switching between the parallel and anti-parallel configuration.

2.3 *Modern notions on spin tunneling*

We will discuss some of the experiments which shed new light on the physics of MTJs. As mentioned earlier, no attempt will be made to be exhaustive. Excellent reviews on Spin tunneling in magnetic junctions, with a description of recent advances, are provided by Yuasa et al.[21] and Swagten et al.[22]

In 1971, Tedrow and Meservey[23] reported the first experiments on spin tunneling. In this case, only one electrode was ferromagnetic (Ni), the other being a superconductor (Al). They found that though minority electrons dominate the DOS at the Fermi level of Ni, majority electrons were tunneling through the thin AlO_x barrier. It was later suggested by Hertz and Aoi[24] in 1973 and by a

[21] S. Yuasa et al., J. Phys. D: Appl. Phys. **40**, R337 (2007)

[22] H. J. M. Swagten, *Spin tunneling in magnetic junctions.* (Elsevier, Oxford, UK, Vol. 17, Chap. 1, 2007)

[23] R. Meservey et al., Phys. Rep. **238**, 173 (1994)

[24] J. A. Hertz et al., Phys. Rev. B **8**, 3252 (1973)

Sterns[25] (1977) that, although the dominant species of electrons at the Fermi level of transition metal ferromagnets were spin-down d electrons, they did not couple well with the states over the barrier. Instead, highly dispersive s-like electrons had a much larger overlap integral with states in the barrier. This led to a larger transmission probability. Moreover, they also realized that the interaction between the s and d-electrons (s-d hybridization) lead to a suppression of the s-DOS in regions of large d-DOS, which is also the case at the Fermi level of a 3d transition metal ferromagnet. Accordingly, this induced a spin polarization of the s-DOS at the Fermi energy. After these initial experiments, Jullière[26] made the first prediction of a TMR effect. Given these demonstrations and predictions in spin tunneling, mainly due to technical difficulties, it took almost 25 years to do the first successful experiment with two ferromagnetic electrodes adjacent to a tunnel barrier. In all these experiments AlO_x was preferred as a barrier material, primarily since it allowed easy growth of a pin-hole free thin barrier by natural, thermal or plasma oxidation of Al thin films. This was particularly convenient for the Tedrow and Meservey's experiments, as they used Al as a superconducting bottom electrode anyway.

After the demonstration of TMR in MTJs, there were various attempts to verify the simple equation 2 given by Jullière which included the spin polarization (P) of the ferromagnetic electrode. It was found experimentally that the spin polarizations of 3d ferromagnetic metals and alloys based on iron (Fe), nickel (Ni) and cobalt (Co) were always positive and usually between 0 and 0.6 at low temperatures below 4.2K[27]. The MR ratios estimated from Julliere's model (using these measured P values) agree relatively well with the MR ratios observed experimentally in MTJs, but the theoretical values of P obtained from band calculations, however, do not fully explain the observed MR ratios in these junctions. Even the signs of P often differ between theoretical values and experimental results. This discrepancy, one of the most fundamental questions with regard to the TMR effect, is discussed in the following subsection.

[25] M. B. STEARNS, J. Magn. and Magn. Mater. **5**, 167 (1977)

[26] M. Julliere, Phys. Lett. **54A**, 225 (1975)

[27] R. Meservey et al., Phys. Rep. **238**, 173 (1994); and S. S. Parkin et al., Proc. IEEE **91**, 661 (2003)

2.3.1 *Tunneling through an amorphous barrier*

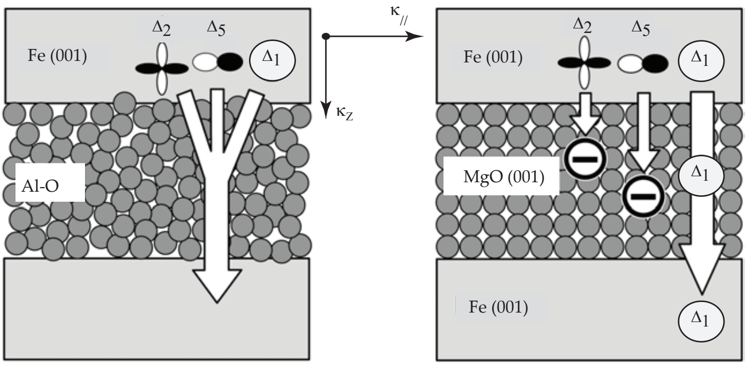

(a) (b)

Figure 8: Schematic illustrations of electron tunnelling through (a) an amorphous barrier and (b) a crystalline MgO(001) barrier.[adopted from Ref. 21]

This section elucidates an incoherent tunneling process through an amorphous barrier with 3d ferromagnetic electrode. Tunneling in MTJ with AlO_x barrier is illustrated schematically in Fig. 8. For these MTJs, Jullière's model with the spin polarization measured experimentally yield a maximum TMR of about 100% at low temperature. An MR ratio of about 81% at RT is therefore close to the Jullière's limit for the 3d-ferromagnetic electrodes if a reduction in P due to thermal spin fluctuations at finite temperatures is taken into account. While modeling the TMR effect in MTJ, Jullière assumed that the tunneling probabilities were equal for all Bloch states[28] in the electrodes which corresponds to a complete incoherence. This assumption is not valid in AlO_x based junction. The spin polarization P obtained from a first principle calculation of the DOS of the Co and Ni electrode is negative compared to the P value observed experimentally for these materials when they form a tunnel junction with Al-O tunnel barrier. This discrepancy indicates that the tunneling probability in actual MTJs depends on the symmetry of each Bloch state. The Δ1 Bloch states with larger P are considered to have higher tunneling probabilities than other Bloch states. This results in a positive net spin polarization of the ferromagnetic electrode. Because the other Bloch states, such as Δ2 states (P<0), also contribute to the tunneling current, the net

[28] Various Bloch states with different symmetries of wave functions exist in the electrode. Because of the tunnel barrier is amorphous, there is no crystallographic symmetry in the tunnel barrier. Due to this nonsymmetrical structure, Bloch states with various symmetries can couple with evanescent states in Al-O and therefore have finite tunneling probabilities. In 3d ferromagnetic metals and alloys, Bloch states with Δ1 symmetry (spd hybridized states) usually have a large positive spin polarization at E_F, whereas Bloch states with Δ2 symmetry (d states) often have a negative spin polarization at E_F.

spin polarization of the electrode is reduced below 0.6 in the case of the usual 3d ferromagnetic metals and alloys.

2.3.2 *Coherent tunneling*

The concept of coherent tunneling is schematically illustrated in figure 8b. One aspect which is highly unlikely in tunneling through an amorphous barrier is $k_{||}$ conservation of the electron wave vector. On the contrary, in a crystalline barrier, $k_{||}$ conservation is a distinct possibility. This also implies that a wave vector selected at one interface efficiently couples to a corresponding wave vector at the other interface. Keeping in mind that P is not constant over the whole Fermi surface, and the possibility of coherent tunneling, one may imagine that using a certain electrode-barrier interface in a certain crystallographic orientation would result in efficient electron tunneling for wave functions which have specific symmetries. Among other systems, such coherent spin tunneling behavior has been theoretically predicted for epitaxial Fe(001)/MgO(001)/Fe(001), and later, also for other bcc ferromagnetic electrodes based on Co, and CoFe alloys. In these tunnel junctions, one describes three kinds of evanescent states $\Delta 1$, $\Delta 2$, $\Delta 5$) which coherently tunnel between the MgO barrier and single crystalline Fe electrodes [see Figure 9[29]]. The choice for Fe (001) is made on the basis of the fact that the highly dispersive $\Delta 1$ is present at the Fermi level only in the majority spin channel, and absent in the minority spin channel. Moreover, as shown in Figure 9, this band has a relatively small attenuation coefficient in MgO(001), as compared to the $\Delta 5$, $\Delta 2^{/}$ bands.

In a tunnel junction, these two factors play a key role in determining the tunnel conductance for the parallel and anti-parallel configuration. For instance, in the anti-parallel configuration, the fact that majority $\Delta 1$ states efficiently tunnel through the barrier but cannot couple with the DOS of the other electrode due to the absence of such a band at the Fermi level. This is shown in Fig. 9. In the case of bcc Co(001), the situation is even more interesting. Here, for the majority channel, only the $\Delta 1$states lie at the Fermi level. Therefore, it is theoretically expected that all the states are completely reflected at $k_{||}$ =0 in anti-parallel configuration, result-

[29] W. H. Butler et al., Phys. Rev. B **63**, 054416 (2001)

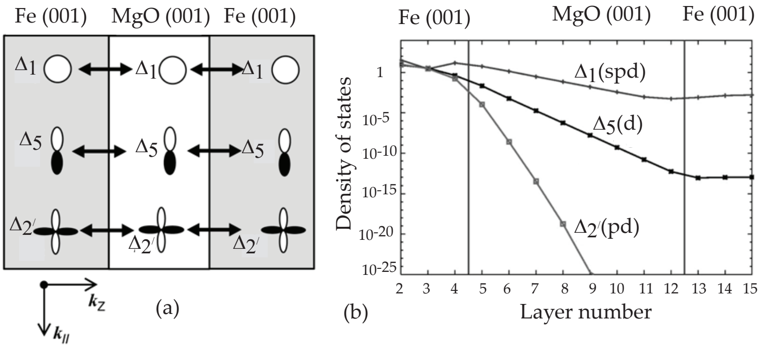

Figure 9: (a) Coupling of wave functions between the Bloch states in Fe and the evanescent states in MgO for the $k_{||}=0$ direction. (b) Layer-resolved tunneling DOS for $k_{||}=0$ in Fe(001) / 8 monolayers MgO / Fe(001) for majority electrons when the magnetization of the Fe layers is oriented in parallel. Each curve is labelled by the symmetry of the incident Bloch state in the left Fe electrode, showing, for example, the slow decay of the states with Δ1 symmetry. [adopted from Ref. 29]

ing in a giant TMR.

2.4 *Elastic and inelastic tunneling*

The electron tunneling process discussed till now is valid only for an ideal barrier which has no defects. This is actually not valid for a real barrier. The barrier contains rather a finite density of defect states, which can significantly affect the tunnel current. Such defective state occur in oxide barriers and mostly arises due to oxygen vacancies. To achieve a more precise description of an electron tunneling through a real junction, the effect of defects (localized states) on the tunneling current will be described. The theories for electronic transport over localized states were developed initially for amorphous silicon and will be applied here for the MgO used as barrier material. As in the previous section, only the one-dimensional case will be examined since it models all relevant processes. Localized state (LS) in the barrier can lead to new current channels such as resonant tunneling or inelastic hopping via chains of localized states. Different tunneling channels are distinguished by the number of localized states an electron tunnels over. Possible elastic and inelastic tunneling channels with an increasing number of localized states are illustrated in Fig. 10. The total conductance of the tunnel junction consists of the sum of the individual channel conductance. In the following a brief overview of the different tunneling channel is presented.

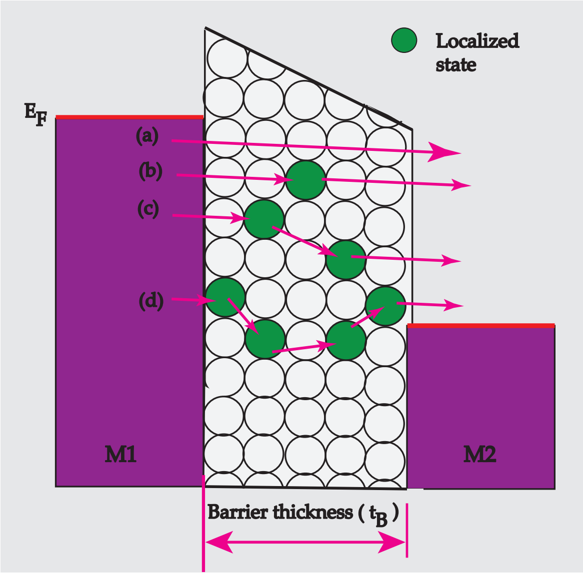

Figure 10: Possible tunneling channels in metal/ insolator/metal tunnel junction: (a) direct tunneling with N=0 localized states; (b) resonant tunneling with N= 1 localized states; (c) (inelastic) tunneling over N>1 localized states; (d) variable range hopping over "many" localized states. The red lines represent the Fermi level. The colored(Lilac) areas represent filled electron states in the metal layers. The Fermi levels of the metals are shifted with respect to each other due to an applied voltage V.

2.4.1 *Direct tunneling (N=0)*

Direct elastic tunneling, where an electron tunnels directly from one electrode to the other is already discussed in previous sections of this chapter. This type of tunneling is portrayed in Fig. 10 (a) and the relation for tunneling current is given by Eq. 1. The conductivity of this channel depends on the barrier thickness in an exponential manner[30]:

$$G_0^{dir} = \widehat{G}_0^{dir} e^{-2\alpha d} \tag{3}$$

with α^{-1} as the localization length. Direct tunneling is the dominant channel in contacts with barriers not much thicker than α^{-1}. The temperature dependence of $\widehat{G}_0^{dir}$ is rather weak as it derives from the thermal broadening of the Fermi function of the electrodes[31]:

$$\widehat{G}_0^{dir} = G_0(0).\frac{CT}{sinCT} \tag{4}$$

Where C=1.384×10$^{-4}\frac{t_B}{\sqrt{\Phi}}$ with barrier thickness (t_B) in Å and the barrier height Φ in eV.

---

[30] Y. Xu et al., Phys. Rev. B **52**, 2843 (1995)

[31] R. Stratton, J. Phys. Chem. Solids **23**, 1177 (1962)

2.4.2 *Resonant tunneling (N=1)*

In resonant tunneling an elastic electron tunnels over one localized state (see Fig. 10b). The tunneling process is accomplished by an electron, first tunneling to the localized state and then continuing to the second electrode. This allows for a much higher barrier thickness. The highest probability for a tunneling process in this case is given for a localized state placed in the middle of the barrier at an energy within an intrinsic width from the Fermi level. Larkin and Matveev[32] alleged the resonant tunnel conductivity as the sum of all resonant tunneling channels over the contact area. From their calculations and from the barrier thickness dependence of the resonant conductivity, one can write resonant conductance as[33]:

$$G^{res} = \frac{2\pi^2 e^2}{h} g S \alpha^{-1} E_o e^{-\alpha d} = \widehat{G}_1^{res} e^{-\alpha d} \tag{5}$$

where g is the conductance at absolute zero, S is an area of junction and E_o is a measure of effective depth of localized state. A direct consequence of this thickness dependence is the domination of the resonant tunneling conductivity over direct tunneling at high barrier thicknesses. Resonant tunneling is independent of temperature in its first approximation. However, electron-phonon interaction leads to a small temperature dependent correction [34]. Theoretically, resonant (elastic) tunneling should be possible over more than one localized state at even higher barrier thicknesses, as discussed in [35]. However, experiments show that inelastic tunneling created by phonon-assisted hopping prevents these channels from being observed.

2.4.3 *Inelastic hopping conductance (N>1)*

If more then one localized state lies in a tunneling barrier, than it is likely that an electron may tunnel over these localized states. This multi-step tunneling (hopping) led to a new inelastic transport channel that depends on temperature T, voltage V, and barrier thickness t_B. Glazman and Matveev[36] proposed a microscopic model for hopping via N>1 localized state. They showed that with increasing temperature or bias voltage, the tunnel current via the inelastic channels increases greatly. This is intuitively ob-

[32] A. Larkin et al., Sov. Phys. JETP **66**, 580 (1987)

[33] Y. Xu et al., Phys. Rev. B **52**, 2843 (1995)

[34] L. Glazman et al., Sov. Phys. JETP **67**, 163 (1988)

[35] A. Larkin et al., Sov. Phys. JETP **66**, 580 (1987)

[36] L. I. Glazman et al., Sov. Phys. JETP **67**, 1276 (1988)

vious, by increasing T or V; both increase the energy corresponding to localized state and tunneling electron. This will increase the probability for the formation of inelastic chains. The resulting conductance due to all possible inelastic conductance channels is given as:

$$G(V,T) = \sum_{N\geq 2}^{\infty} G_N \tag{6}$$

where G_N is either voltage driven or temperaturee driven chain conductance and is given below:

$$G_N(V) = \frac{S\alpha}{t_B}\left(\frac{g t_B e V N^2}{\alpha^2}\right)^N \left[\left(\frac{E_0}{eV}\right)\lambda^{(N-1)/2} exp(-\alpha t_B)\right]^{2/(N+1)} \tag{7}$$

and

$$G_N(T) = \frac{S\alpha}{t_B}\left(\frac{g t_B K_B T N^2}{\alpha^2}\right)^N \left[\left(\frac{E_0}{K_B T}\right)\lambda^{(N-1)/2} exp(-\alpha t_B)\right]^{2/(N+1)} \tag{8}$$

In above equation the factor $\frac{S\alpha}{t_B}$ represent the number of statistically independent conductance channels in the barrier with the total area S and λ is dimensionless electron phonon coupling parameter. The factor $\frac{g t_B K_B T N^2}{\alpha^2}$ or $\frac{g t_B e V N^2}{\alpha^2}$, represent the probability for the formation of such channels. The transport of electrons through incoherent successive tunneling along a conducting chanel with N localized states can be considered as an effective series connection of N-1 resistances with a characteristic conductivity. By solving equation 7 and 8 we have inelastic conductance channels given as:

$$G_N(V) = a_N . V^{N-2/(N+1)} \tag{9}$$

and

$$G_N(T) = \sigma_N . T^{N-2/(N+1)} \tag{10}$$

where a_N and σ_N are constants that depends on the radius of localized states and their density, as well as on the barrier thickness t$_B$.

2.4.4 *Variable range hopping*

The variable range hopping is the predominant conduction mechanism in the limit of thick barriers and high temperatures. As the barrier thickness approaches the bulk limit, characterized by the variable range hopping, one-dimensional tunneling channels are no longer possible. The Mott hopping model[37] describes transport in this case (schematically in Fig. 10d). The variable range hopping conductance (G_{VRH}) is determined by two counteracting conditions. On the one hand, the localized states must be near enough to allow overlap between the electron wave functions. On the other, the distance between states needs to be high enough to allow for finding a localized state with a small energy difference. These conditions together fix a typical hopping length l_{VRH}. This is a function of temperature, as it was found that l_{VRH} varies as $T^{1/4}$. Therefore, the l_{VRH} acquires the form

$$l_{VRH} = \alpha^{-1} exp \left(\frac{-T^{*}}{T} \right)^{1/4} \tag{11}$$

Where T^{*} is given by $k_B T^{*} = 23/g\alpha^{-3}$. The Mott hopping model thus results in the following conductivity law:

$$G_{VRH} \approx exp \left(\frac{-T^{*}}{T} \right)^{1/4} \tag{12}$$

[37] N. Mott et al., *Electronic processes in noncrystalline materials* (Oxford Univ. Press, New York, 1979)

3

Techniques for fabrication and characterization of magnetic tunnel junctions

This chapter contains an overview of the experimental techniques used for the fabrication processes and characterization of magnetic tunnel junctions. The entire process of fabrication begins with the multilayer deposition of magnetic and non magnetic materials, followed by patterning using Laser lithography and ion beam etching. Then the temperature dependent transport *i.e.* elastic and inelastic conductance of tunnel junction and their dielectric breakdown voltage at room temperature have been investigated.

3.1 Sample preparation and corresponding techniques

3.1.1 Thin film deposition

Several methods are used for technical thin film deposition, e.g., thermal evaporation, chemical vapor deposition (CVD), molecular beam epitaxy (MBE), laser ablation, and sputtering etc. From a technical relevance point of view, the sputtering process is most important, and has been used for the preparation of the samples discussed here. The sputtering process involves the physical deposition of a material from a target to a substrate by using a plasma. The plasma is generated from a sputtering gas; usually, an inert gas like Ar. The sputtering processes can be classified by the way the plasma is generated.

The easiest way to generate the plasma is using a glow discharge. The simplest setup for this consists of a vacuum chamber, a constant voltage source, a sputter source, a substrate holder and a pumping system (see Fig. 11). A rare gas, usually Argon, is introduced into the vacuum chamber between the target, the grounded substrate and the chamber walls. By applying ahigher voltage to the target, a plasma is generated, while the positive ions of the sputtering gas are accelerated towards the target. The ions bombarding the target may have enough energy to cause the ejection of surface atoms and emission of secondary electrons, which will cause further ionization of the sputtering gas in the chamber. The principal source of electrons to sustain the plasma is the secondary electron emissions caused by the bombardment of ions into the cathode, so that a self-sustaining condition is established.

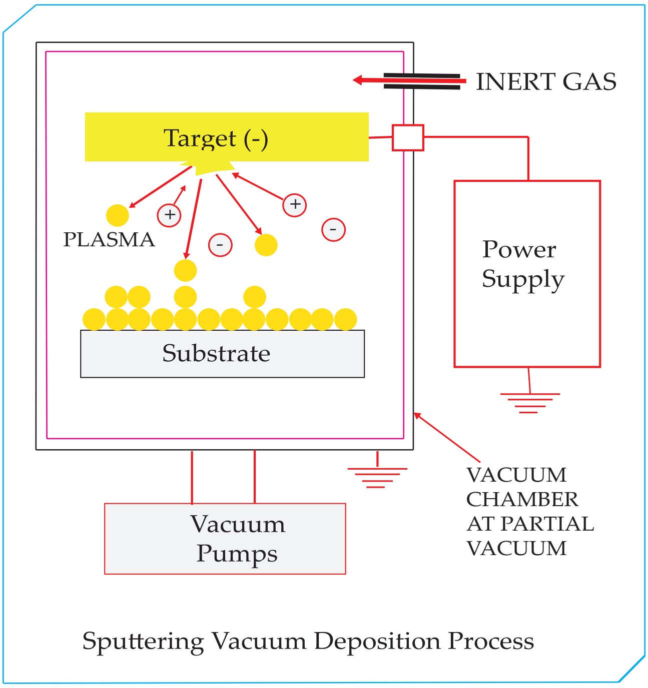

Figure 11: Material deposition of thin films by the DC sputtering. The image is taken from website: www.tcbonding.com /sputtering.html

The target atoms that are struck out by the ions will traverse the chamber and be deposited on the substrate. Since the chamber is large in comparison to the mean free path of the atoms, the atoms are deflected by scattering events. Therefore, a sputtering process results in an almost undirected deposition of the material on the substrate. This type of sputtering is usually referred to DC or diode sputtering and has proven to be a useful technique in the deposition of thin films when the cathode is covered with the source material ("sputtering target"). However, diode sputtering has two major disadvantages. The deposition rate is slow, and the electron bombardment of the substrate is extensive and can cause overheating and structural damage.

The development of magnetron sputtering[38] deals with both of these issues simultaneously. Magnetron sputtering cathodes use powerful magnets to trap the free electrons in a magnetic field directly above the target surface; these electrons are not free to bombard the substrate to the same extent as with diode sputtering. At the same time, the extensive, circuitous path carved by these same electrons when trapped in the magnetic field, enhances their probability of ionizing a neutral gas molecule by several orders of magnitude. This increase in available ions significantly increases the rate at which target material is eroded and subsequently deposited onto the substrate. Therefore, the magnetron sputtering can be operated with lower gas pressures and voltages in comparison to glow discharge plasmas. Sputtering can be done either in DC or RF modes. DC sputtering is very effective for the deposition of conductive materials. However, if the target is a non-conducting material, the positive charge will build up on the material and it will stop sputtering. To overcome this problem, RF sputtering method was developed.

RF sputtering uses a radio frequency sinusoidal voltage to derive the source. The substrate and chamber walls are held at ground potential. Using this approach, the charge that builds up on the dielectric target is dissipated through the second half of the cycle. A detailed description of the sputtering processes discussed above can be found elsewhere[39].

[38] A. Elshabini-Riad et al., *Thin film techanology handbook* (McGraw Hill, 1998)

[39] L. Maissel, *Handbook of Thin Film Technology* (McGraw Hill, 1983)

Deposition of the investigated samples

Magnetic tunnel junctions have been deposited by RF/DC magnetron sputtering using a CLAB 600 system by Leybold Vakuum GmBH. It is a fully automatic system that consists of a sputter chamber with six four inch magnetron sputter cathodes: two RF and four DC magnetron sputtering cathodes, a substrate rotating table and a central handling robot system. Five of the four inch targets are used for DC sputtering (at a power of 115 W). Two have special construction characteristics for ferromagnetic targets. The insulator barrier is sputtered by using a Hÿttinger RF generator (13.56 MHz) and an MgO target. The base pressure of the sputtering system is 1×10^{-7} mbar. The pressure of the sputter gas in the range of 1×10^{-3} mbar is controlled by two parameters inlet Ar flow and the throttle position (the valve controlling the pumping speed by obstruction or constriction).

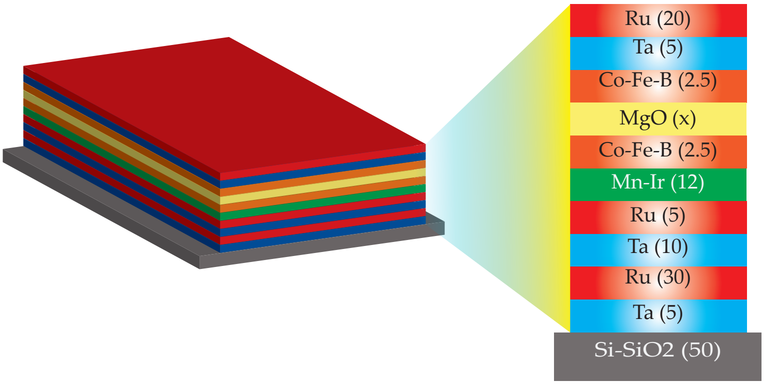

Figure 12: Schematic overview of the MTJ standard stack sputtered using the Leybold CLAB 600. The numbers in parenthesis represent the nominal thickness of each layer in nanometers.

In order to achieve the reproducible stacks it is important to have good control over the Ar flow and throttle position. For the DC sputtering of metallic elements, an Ar flow of 20 sscm and a throttle position of 21% is used, equivalent to an Ar pressure of 1.2×10^{-3} mbar. During the RF sputtering of MgO barrier, the Ar flow stays 20 sscm but the throttle position is 3% (at Ar pressure of 2.4×10^{-2} mbar). A schematic overview of the MTJ standard stack with a layer sequence is shown in Fig. 12

All samples were deposited on thermally oxidized SiO_2 wafers. All metallic layers were deposited by DC magnetron sputtering. The MgO barrier of thickness t_B between 1.8-5 nm was deposited by RF magnetron sputtering. The atomic composition of the sputter target was $Co_{70}Fe_{30}$, $Co_{40}Fe_{40}B_{20}$ and $Mn_{83}Ir_{17}$ for Co-Fe, Co-Fe-B and Mn-Ir target, respectively. The sputter rate of each target was experimentally verified using an X-ray diffraction technique before beginning an entire sputtering process. The thickness of the sputtered layer depends on the growth conditions, *i.e.* sputter rate and time:

$$d = C \times (t + 0.55) sec \tag{13}$$

where d is the thickness of the growing layer in nm, C is the sputter rate in nm/sec and t is the deposition rate in sec. The constant time (0.55 s) corresponds to the opening and closing of the shutter.

The deposition time is calculated from Eq. 13. Further, these data together with other sputter parameter are fed to the computer that controls the thickness of each layer accurately.

3.1.2 *Vacuum annealing*

After deposition, samples were annealed in a vacuum to ensure the exchange bias of the hard electrodes comprised of an Mn-Ir anti-ferromagnetic layer together with a ferromagnetic Co-Fe-B layer. The amorphous Co-Fe-B layer partially crystallized during the post-annealing process, effectively improving the quality of electrode/barrier interface, leading to an increase of the TMR ratio. Samples were annealed in a vacuum furnace with a base pressure of 1×10^{-7} mbar at a temperature occurring between the Curie temperature of the ferromagnet and Neel temperature of the anti-ferromagnet. During the annealing process, a strong magnet of 6.5 kOe is applied from a permanent magnet to define a magnetic ordering of the ferromagnetic layer. Afterwards, the sample is field cooled through the Neel temperature of the antiferromagnetic layer at room temperature.

For the samples, the annealing was done at temperatures varying between 200-500^0 C for one hour in the presence of a magnetic field. All samples were cooled for 30 minutes.

3.1.3 *Lithography*

For transferring patterns onto the multi-layers, different lithography techniques are available. In principal they can be divided into mask based (parallel) and writing (serial) processes. The advantage of parallel processes is the rapid duplication of images of the mask. The disadvantage is the complicated and expensive mask production. In serial processes, direct writing with a focused beams of electrons (e-beam lithography), ions (FIB - focused ion beam lithography) or photons (laser direct writing) is used. In this work, all MTJs were first patterned by laser beam onto the photo resist that was spin coated on the top of the multi-layers. We used the DWL 66 Laser Lithography system from Heidelberg Instruments GmbH. The resolution of the instrumentation is 400 nm. The system can fabricate patterns with a minimum size of 1.2 μm. This direct writing system uses a laser as a radiation source with an output power of 90 mW at a wavelength of 442 nm. The table 1 gives an overview of the photo-resist and processing chemicals along with spin coating parameters used here.

Table 1: Overview of the employed resists and processing chemicals

solution	type	spin coating parameters
ARP5350 from Allresist	positive resist	5000 rpm for 30 s
baking	**30 minutes at 90^{o}C**	
AR-300-35 from Allresist	developer	8-10 sec
removing	**with acetone for 5 minutes in an ultrasonic bath at room temperature**	

3.1.4 *Ion beam milling*

In the lithography step, MTJ elements are patterned with laser beams into a positive photo-resist. An Ion beam milling process transfers structures onto a layer stack. The resist protects the underlying material during the etching process while the unprotected material is simply etched away. In this work, ion beam milling is done on an apparatus built in Bielefeld. The ion beam is produced by an Ar gas fed into the source chamber and ionised by electron bombardment. These Argon ions are accelerated and bombarded into the surface of the sample during the milling process. To ensure homogeneous etching and to avoid short-circuited TMR elements, the sample holder is tilted by 30^0 from normal incidance and rotates slowly. A comprehensive description of the apparatus can be found elsewhere[40].

The removed particles can be neutral or charged. The charged particles pass through an energy filter and are analyzed by a quadrupole mass spectrometer that is attached to the etching chamber. From the analyzed particles, the material that is eroded is known precisely. This feature is very helpful to stopping the process exactly at the desired layer of the stack.

3.1.5 *Junction microfabrication*

The micrometer size samples investigated in chapter 4 have been patterned by a single step laser lithography, and an Ar-ion etching process. However, the samples investigated for TMR temperature dependence and inelastic electron tunneling spectroscopy were prepared by a two step lithography process. For every sample, different arrays of squares with actual dimension of 15, 20 and 25 μm were defined. The lateral distances were chosen to be three times the dimensions of the elements. Fig. 13 shows the step by step procedure used to fabricate the tunnel junctions. The first step is the optical lithography (a) that consists of spin-coating the sample with a resist, exposing it with a laser lithographer, and developing the resist to get the written design (see Fig. 13(b)). Then, the whole sample is etched with Ar ions, down to the Ru layer. Finally, the resist is removed in a bath of solvent under application of ultrasonic agitation (Fig. 13(d)). The breakdown tests were performed on these junctions using a conventional two probe method.

For temperature dependent transport measurement, an additional lithography step was done to form a contact pad for bonding on a chip carrier which fit into a cryostat. For those junctions after developing and etching in first step as shown in Fig. 13(c), TaO_x was deposited using a home built sputter machine by RF

[40] M. Panhorst, PhD thesis, Bielefeld university, 2005

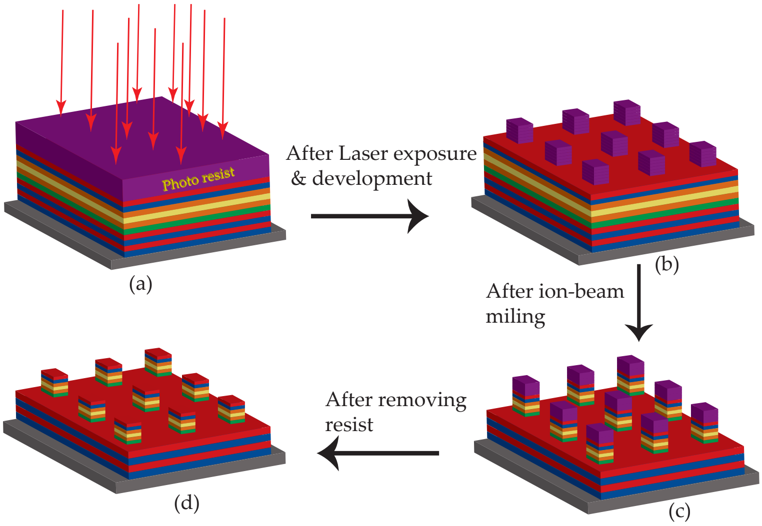

Figure 13: 3D view of the first lithography step and its adjacent process to fabricate junction for time dependent dielectric breakdown study.

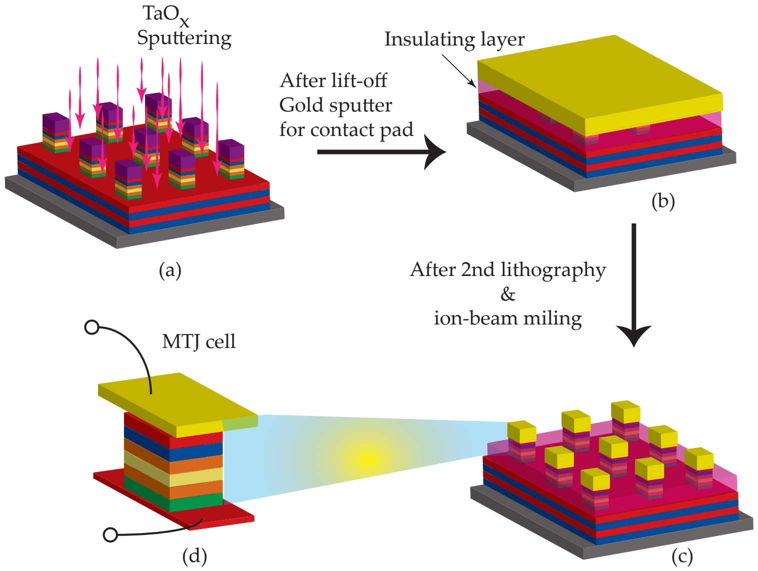

Figure 14: (a-c) 3D view of the second lithography step and its adjacent process and (d) expanded overview of MTJ cell

reactive sputtering at a power of 50W. It is shown in Fig. 14. For this sputtering, the partial oxygen pressure used was 2×10^{-4} mbar and Ar flow was adjusted to reach a pressure of 3.5×10^{-3} mbar. The thickness of the insulator sputtered between the elements was large enough to ensure the electrical isolation of the elements and small enough to facilitate the further lift-off process. A thickness of 50-60 nm of TaO_x proved to be a good electrical insulator. The lift off process time for a photo resist was around 5 to 10 minutes. After finalization of this step, the only part of the wafer that contained the entire TMR stack was in the region where the elements were present. The last process of the second step was the sputtering of Ta and Au layers for the contact pad that would be put on top of the elements in order to contact them for the measurements. The total thickness of this layer was around 60 nm and is shown in Fig. 14(b). The last lithographic step comprise of the pattering of structure for contact pad by laser beam and an ion beam etching procedure, where care must be taken to stop etching process in the TaO_x layer. The next step is the resist removal situated on top of the contact pad. After this final stage the sample is ready to be measured and characterized (see fig.14(c, d)).

3.2 *Characterization and analysis techniques*

The characterization of MTJs used was conducted through transport and structural measurements. Transport properties were observed via current-voltage measurements and their (measured or calculated) derivatives. These measurements could be recorded under the influence of magnetic fields. Structural characteristics were performed by transmission electron microscopy (TEM). This section includes an overview of the measurement methods at room temperature, low temperature and structural characterization techniques.

3.2.1 *Transport measurements*

Room temperature transport measurements were carried out by conventional 2 probe DC technique. During the measurement it was possible to apply a voltage of maximal ±10 V with a desired step size through a computer that controlled and monitored all the hardware. The current was measured by an electrometer with different amplification ranges. The output of the electrometer was measured by a Keithley Model 2000 digital multi-meter. A homogeneous magnetic field was produced by two coils with a ferrite rod supplied with a 36V-12A power supply and with an error of ± 5mV. The maximum field produced by the coils was in the range of 3500 Oe and was measured using a Bell 6010 Gauss/Tesla meter. A comprehensive description of the apparatus can be found in the thesis by Andy Thomas[41]. The electric properties of the TMR samples were determined by two point measurements perpendicular to the plane. Most of the MTJs were contacted carefully with a thin gold needle from the top. The contact to the lower conduction line was obtained by pressing a thicker gold needle hard on the sample outside the MTJ, and scratching it to destroy the barrier. To determine the resistance in dependence of the external magnetic field, a constant bias voltage was applied while the external magnetic field varied. Unless otherwise stated, a bias voltage of 10 mV was used.

Low temperature measurements were carried out in an Oxford Instruments closed cycle helium cryostat, which provides temperatures down to about 13 K. Other types of measurements carried out in these experimental settings were current voltage measurements, dielectric breakdown (chapter 4) with various constant magnetic fields, and inelastic electron tunneling spectroscopy as described in chapter 6.

3.2.2 *Transmission electron microscopy*

Transmission Electron Microscopy (TEM) has become a mainstay among characterization techniques for materials scientists. This technique uses a beam of electrons that is transmitted through an ultra thin specimen, interacting with the specimen as it passes through it. A series of magnetic lenses, at and below the sample position, are responsible for delivering both, the undeflected and deflected electrons signals that penetrate the sample thickness to a detector, usually a CCD camera. Accompanying this signal trans-

---

[41] A. Thomas, PhD thesis, Bielefeld univetsity, 2003

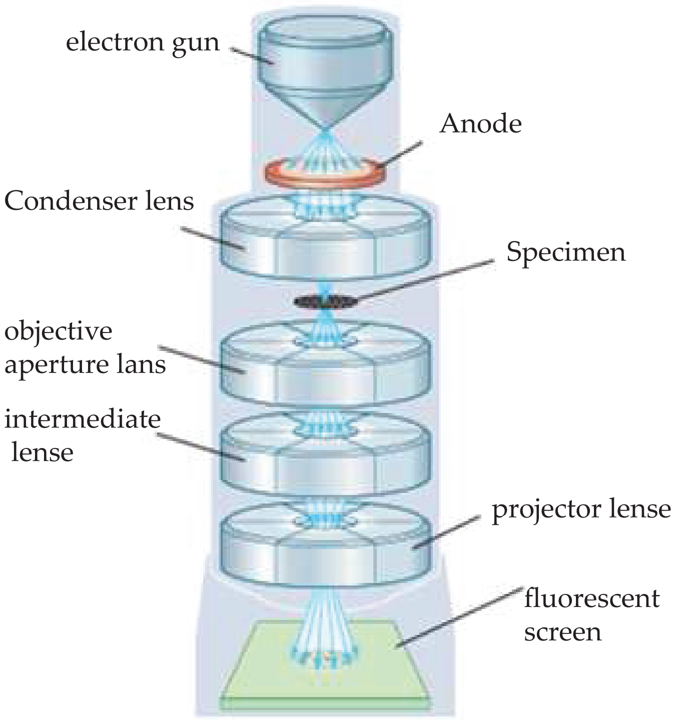

Figure 15: Schematic view of Transmission Electron Microscope. [Image is taken from web site: http://media-2.web.britannica.com/eb-media/90/113690-004-CB552E7F.gif]

mission is a magnification of the spatial information in the signal by as little as 50 times to as much as a factor of 10^6. This remarkable magnification range is facilitated by the small wavelength of the incident electrons, and is the key to the unique capabilities associated with TEM analysis. A schematic of a TEM instrument showing the location of a thin sample and the principal lenses within a TEM column, is illustrated in Figure 15.

The transmission electron microscope uses a high energy electron beam transmitted through a very thin sample to image and analyze the microstructure of materials with atomic scale resolution. The electrons are accelerated at several hundred kV, giving wavelengths much smaller than that of light: 200kV electrons have a wavelength of 0.025Å .

Because even for very thin samples one does not usually see individual atoms. Rather the high resolution imaging mode of the

TEM, images the crystal lattice of a material as an interference pattern between the transmitted and diffracted beams. This allows one to observe planar and line defects, grain boundaries, interfaces, etc. with atomic scale resolution. The brightfield/darkfield imaging modes of the microscope, which operate at intermediate magnification, combined with electron diffraction, are also invaluable for giving information about the morphology, crystal phases, and defects in a material. For the structural investigation of full magnetic tunnel junctions, high resolution transmission electron microscopy (HR-TEM) has been used.

3.2.3 *Inelastic electron tunnel spectroscopy*

When a voltage is applied to a metal/isolator/metal tunnel junction, electrons can tunnel from occupied electronic states in one electrode to free states in the other electrode[42] [Fig. 16(a)]. When the electrons do not loose energy during this process, it is called elastic tunneling. When the electrons loose energy, e.g., due to the creation of phonons (vibrational excitations, frequency ω_{exc}), this effect is called inelastic tunneling. Therefore, for each type of inelastic tunneling process there is a minimum energy below which this process cannot be found. When this energy is reached, the conductance is increased [Fig. 16(b)]. The change of the gradient of the current versus voltage graph due to the onset of this inelastic tunneling process results in a step in the dI/dV versus voltage curve [Fig. 16(c)].The usual way of plotting inelastic electron tunnel spectroscopy (IETS) measurements is a d^2I/dV^2 versus voltage graph [Fig. 16(d)]. In this kind of graph the step in the dI/dV versus voltage curve resulting from the onset of the inelastic tunneling process is represented by a peak.

To obtain a dI/dV versus voltage curve, a two-probe measurement was carried out where a dc bias voltage with overlaid ac voltage was applied by an electronic measurement setup. The resulting current was detected and amplified by the measurement box. The measured current was used as an input for a Stanford SR830DSP lock-in amplifier. The lock-in amplifier was used as a source of overlaid ac voltage. Ac voltages in the range of 2mV were used. The output of the lock-in amplifier was proportional

[42] S. K. Khanna et al., Science **220**, 1345 (1983)

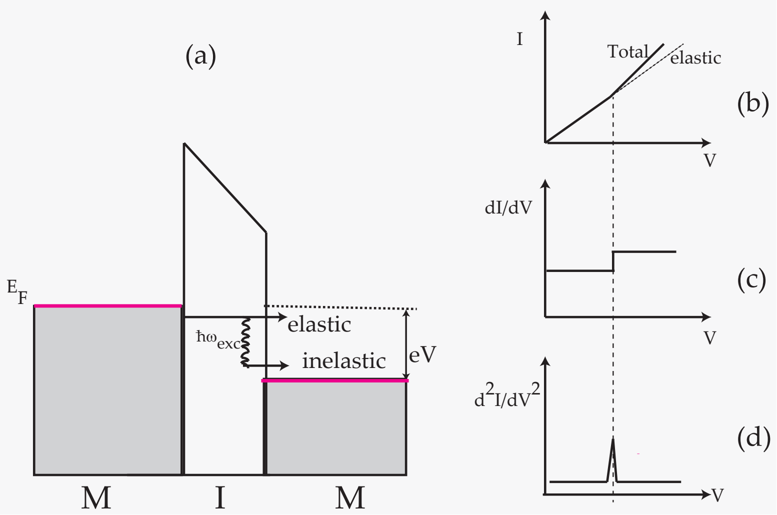

Figure 16: (a) Schematic of Metal- Insulator -Metal junction (energy versus thickness). (b) Current versus voltage graph for a tunnel junction with only elastic tunneling up to a certain voltage indicated by a small vertical line and an onset of inelastic tunneling at this voltage. (c) dI/dV versus voltage measurement resulting from (b), (d) d^2I/dV^2 versus voltage measurement resulting from (b). These graphs are based on a figure in Ref. [42].

to the variation of the current due to the ac voltage. Therefore, this signal was proportional to dI/dV. The IETS signal proportional to d^2I/dV^2 was obtained by differentiating this signal numerically.

To measure IETS spectra of magnetic tunnel junctions, a low temperature was necessary because the thermal energy at room temperature corresponded to about 25 mV. This thermal smearing would camouflage many of the peaks observed at MTJs. Therefore, measurements were carried out in an Oxford Cryo-drive 1.5 closed cycle He cryostat at about 13 K.

4

Dielectric breakdown of magnetic tunnel junction

4.1 Introduction

The dielectric breakdown of magnetic tunnel junction is a serious reliability concern in spintronic devices because of the continuous trek towards smaller and smaller devices with thinner oxide layer. It has recently been found that the MTJs can be switched by spin transfer and MTJs using MgO barriers show large TMR by spin polarized tunneling effect[43],[44]. In spin transfer switching, one of the key technologies is to make excellent tunneling barriers thin enough to allow a high current for switching. Oxide barrier layer in MTJs become more vulnerable to the applied voltage as they get thinner. For this reason, standardized procedures for the characterization of dielectric breakdown are mandatory for the evaluation of the lifetime of spintronic devices. When an electric field is applied across the MTJ, the continued degradation of the barrier will lead to the formation of a conductive path in the oxide and a shortening of the top and bottom electrode. This kind of degradation mechanism is called time dependent dielectric breakdown (TDDB).

In order to assess the applicability of MTJ for devices operating at a voltage much lower than the breakdown voltage, we will present our novel findings regarding time dependent dielectric breakdown in Co-Fe-B/MgO/Co-Fe-B junctions with thickness ranging from about 1.8 nm to 5.0 nm. As a first step to-

[43] W. H. Butler et al., Phys. Rev. B **63**, 054416 (2001)

[44] J. C. Slonczewski, J. Magn. and Magn. Mater. **159**, L1 (1996)

wards the understanding of microscopic breakdown mechanisms, the results have been analyzed in terms of various expressions of voltage dependent breakdown probabilities.

We will first describe the measurement method of the breakdown of our samples (section 4.2), followed by an overview of the experimental results of breakdown measurements (section 4.3). In section 4.4 a general statistical model for breakdown is presented, and apply two models to our junctions for data analysis. A conclusion is given in section 4.5.

4.2 *Measurement method*

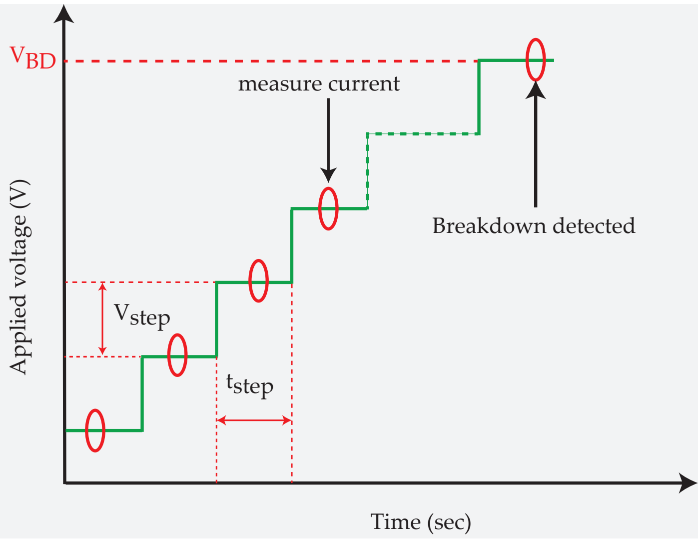

Figure 17: Schematic stress bias of the staircase ramp. The current is measured at the end of each step.

Several types of testing methods have been used to characterize the TDDB of dielectric thin films. Commonly used methods include the ramp voltage stress method (RVS), the constant voltage stress method (CVS), and the constant current stress method(CCS). Excellent reviews of the dielectric breakdown in thin oxide, including testing methods were given by Martin [45] and Ghibaudo[46]. Most directly, the time to breakdown can be measured by either the CVS or the CCS method. These methods have the disadvantage of priori unknown time to breakdown, which can exceed sev-

[45] A. Martin et al., Microelectron. Reliab. **38**, 37 (1998)

[46] G. Ghibaudoa et al., Microelectron. Reliab. **39**, 597 (1999)

eral days or even months when measuring at a low stress voltage, making these methods less convenient. Therefore, breakdown is most often studied using the voltage ramp method. It is a fast measurement method that can provide the intrinsic and extrinsic breakdown strengths of the dielectric with good resolution. Currently, a staircase ramp, similar to a linear ramp, (shown in Fig. 17) is commonly used to perform breakdown tests. It has the advantage of being easy implemented and having good hardware and software control. The most vital parameter in RVS is the ramp speed, as defined by V_{step} and t_{step} as: $\frac{dV}{dt} = \frac{V_{step}}{t_{step}}$. The height of the voltage step determines the resolution of the measured breakdown field. If the V_{step} chosen is to too large, then a small drift in the intrinsic breakdown fields will not be resolved. Therefore, V_{step} of 1mV is taken for better resolution and t_{step} varied to get a ramp speed between 5-20 mV/sec.

4.3 *Experimental results*

For MTJs fabricated with the process discussed in chapter 3, we measured their time-dependent dielectric breakdown using the technique discussed above, and focused on its dependence on the barrier thickness, junction area, polarity of applied voltage, ramp speed, annealing temperature, MTJ state (parallel or anti-parallel), and layer stack. More than 700 breakdown measurements were conducted to assess the reliability of junction during this study. Before starting the breakdown test, the TMR and resistance area product (RA) was measured in each case by biasing the MTJ at 10 mV using constant voltage source. The average values and statistical errors of the TMR amplitudes and RA product acquired at room temperature are listed in table 2.

t_B[nm]	RA_P	RA_{AP}	TMR
1.8	106±10 k$\Omega\mu m^2$	281±10.5k$\Omega\mu m^2$	173±5 %
2.1	323±18 k$\Omega\mu m^2$	821±10.9k$\Omega\mu m^2$	167±4 %
3.0	43.4±3.2 M $\Omega\mu m^2$	77.13±1.8 M$\Omega\mu m^2$	73.2±4 %
4.0	6.09±1.04 G $\Omega\mu m^2$	8.75±0.85 G$\Omega\mu m^2$	22.5±2.3 %

Table 2: Typical RA_P and RA_{AP} products in parallel and anti-parallel magnetization state and corresponding TMR measured with a bias voltage of 10 mV at RT

The resistance of a sample with a 5.0nm barrier thickness was too high to perform reliable TMR measurements. Instead, we estimated its RA product to be about 2T$\Omega\mu m^2$. The RA product both in parallel and anti-parallel state increased exponentially with a barrier thickness, while the average value of TMR at RT decreased with an increase in barrier thickness. The reasons for this decrease are further explain in chapter 5. As similar trends were observed for all barrier thicknesses, i.e. area dependency, polarity of applied voltage, and ramp speed, for the readers ease, we present the results of the junctions with barrier thickness of 1.8 and 2.1 nm first.

RA value extracted by fitting an IV curve (±100 mV) by a linear function.

The intrinsic failure due to voltage stress induced degradation of an insulator is characterized by an abrupt decrease in resistance at the breakdown voltage[47] e.g., as can be seen in Fig. 18.

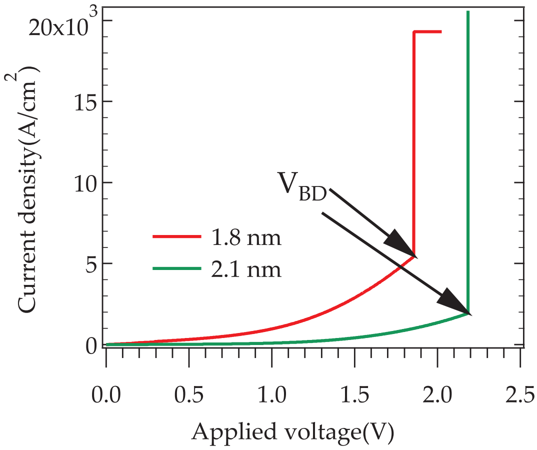

Figure 18: Typical Breakdown I-V characteristics curve for optimally annealed 400 μm^2 junctions in anti-parallel magnetization state (AP) that break at 1.85 V (1.8 nmm) and 2.18 V (2.1 nnm), respectively. The ramp speed is 15mV/s

During the breakdown, a highly conductive path is irreversibly formed that shunts the current. Afterward, no TMR effect was observed and, e.g., the resistance of MTJs with a junction size of 225μm^2 was found to be typically in the range of 75-10 Ω, corresponding to RA products of 17-2.3 k$\Omega\mu m^2$.

The mean current density and voltage of MTJs at the breaking point are shown in Fig.19 (the error bars represent the standard deviation for an ensemble of typically five nominally identi-

[47] B. Oliver et al., J. Appl. Phys. **91**, 4348 (2002)

cal MTJs).

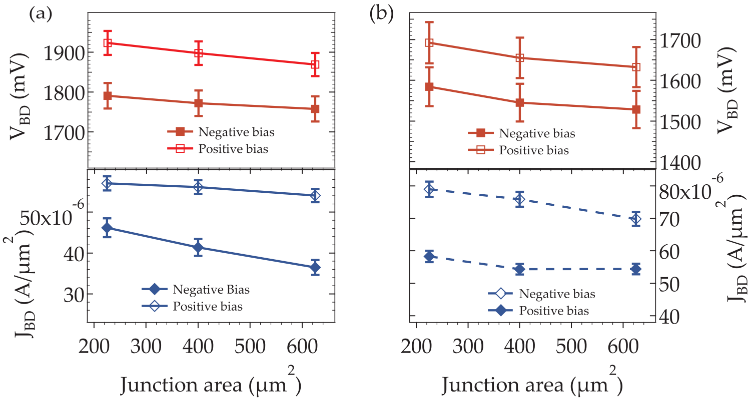

Figure 19: The current density (dotted line) and breakdown voltage (solid line) dependence on polarity of applied voltage for a barrier thickness of 1.8 nm: (a) anti-parallel magnetization and (b) parallel magnetization state. The ramp speed is 15 mV/s.

It was found that the current density and breakdown voltage of MTJs strongly depends on the polarity of the applied voltage. For positively biased top electrodes, the current density and breakdown voltage is about 20 and 10% larger than for negatively biased top electrodes. TDDB dependence on bias polarity indicates that upper and lower MgO/Co-Fe-B interfaces are not equally strong against stress. We speculate that the change of the junction reliability of MTJs under negative and positive bias is caused by properties of the barrier, namely, an asymmetric defect density distribution at the interface regions between the insulator and magnetic layer, e.g., asymmetric structural defects such as the dislocations at the interfaces and lattice distortions. The current density at which the breakdown occurs is, in general, larger for the parallel than for the anti-parallel state. Therefore, the breakdown voltage might not only be dominated by the voltage stress, but can be influenced by the current stress. However, it should be noted that the current density at the breakdown is about a factor of 3 smaller for 2.1 nm thick barriers than for 1.8 nm thick barriers, which favors that current density, though is not as important as the bias voltage.

Figure 20 shows the area and thickness dependence of the breakdown voltage. As can be seen, the breakdown voltage depends strongly on the thickness, and weakly on the junction area in both

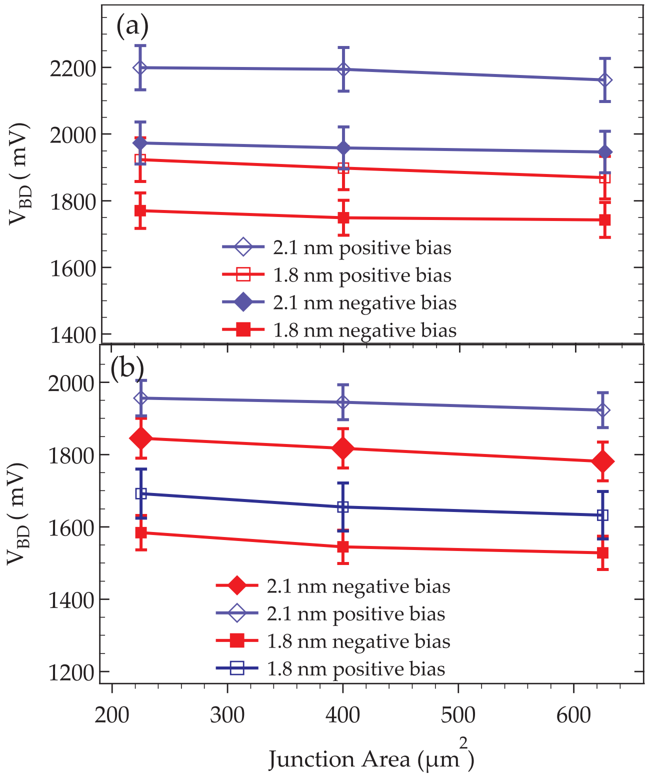

Figure 20: Breakdown voltage dependence on the area and barrier thickness for optimally annealed MTJs: (a) anti-parallel magnetization and (b) parallel magnetization state. The ramp speed is 15 mV/s.

parallel(P) and anti-parallel(AP) magnetization state. By increasing the barrier thickness by 0.3 nm, from 1.8 nm to 2.1 nm, the breakdown voltage considerably increases by an average value of about 9.0%. The breakdown voltage decreases by an average value by about 1.6% when the junction area increases from 225 to 625 μm^2 for a 1.8 nm thick junction under negative bias in AP state. Generally, the breakdown voltage is lower for large area junctions. Obviously, the probability of finding the weaker links is larger when the junction area increases. Moreover, if we compare the breakdown voltage of 64 μm^2 junction (not shown) with 625 μm^2 for a 1.8 nm thick junction, the breakdown voltage of a later junction decreases by about 3.2 %. Hence the breakdown voltage is usually higher for a small area junction. This is true for all barrier thicknesses. This means that for MRAM devices, the junction area

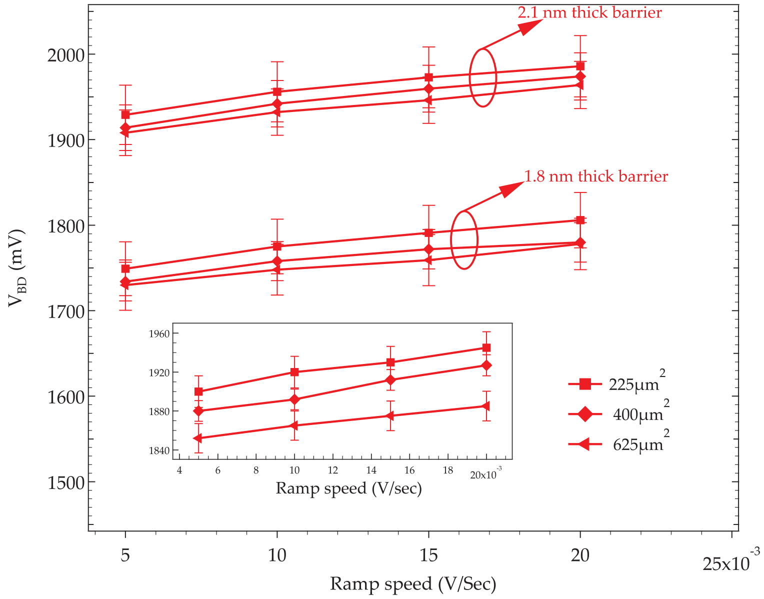

Figure 21: Breakdown voltage dependence on voltage ramp speed in an AP state for optimally annealed MTJs with 1.8 and 2.1 nm thick barriers. The inset of the figure shows the breakdown dependence on voltage ramp speeds for 1.8 nm when the upper electrode is positively biased

is usually much smaller than for actual test junctions. The relationship between breakdown voltage and area is well established by models in the literature as discussed in the next section.

The ramp speed dependence of the breakdown voltage is shown in Fig. 21. It is well know that the breakdown voltage of RVS strongly depends on ramp speed. This was first reported for a SiO_2 based MOS capacitor by Osburn *et al.*[48].

MOS
metal oxide semiconductors

In case of MTJs, the ramp speed dependence on breakdown voltage was first demonstrated and modelled by Oepts[49]. The breakdown measurements were performed upon ramping the applied voltage from V=0V with constant dV/dt for a series of junctions with three different areas under positively and negatively biased top electrodes. From the Fig. 21 it can be seen that the breakdown voltage increases when ramp speed is increased, in agreement with the observation that at lower bias, lifetime increases.

[48] C. M. Osburn et al., J. Electrochem. Soc. **119**, 591 (1972)

[49] W. Oepts et al., Appl. Phys. Lett. **73**, 2363 (1998)

4.3.1 *Barrier thickness dependence of dielectric breakdown*

TDDB measurements were performed for MTJs with barrier thicknesses in the range between 1.8-5 nm. All MTJs show similar V_{BD} trends with respect to the area of the junctions (not shown here). Barrier thickness dependence of breakdown voltage is shown in Fig. 22.

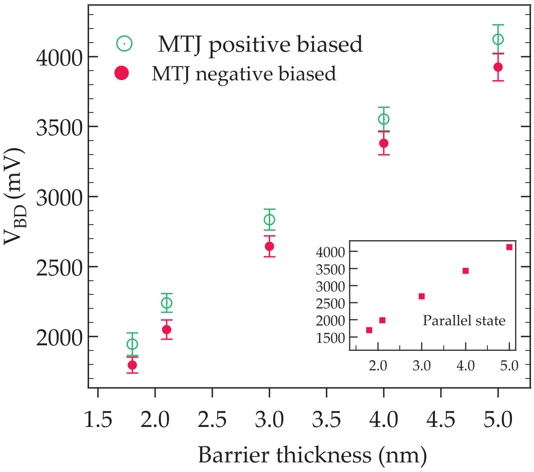

Figure 22: The breakdown voltage dependence on the barrier thickness, and the polarity of applied voltage in anti-parallel magnetization state. The inset shows V_{BD} measured at RT in a parallel magnetization state for positively biased voltage. The junction area is 225 μm^2. Each point is an average of five individual measurements, and the error bars represent the standard deviation. The ramp speed was 15 mV/sec.

A linear increase of breakdown voltage with barrier thickness was observed in all cases. This linear behavior of V_{BD} is in accordance with our micro-structural investigation, which does not provide any hints of the reduction of barrier quality with the increase in MgO thickness. Rather, the TEM micrographs of our MTJs (in chapter 5) clearly reveal that the tunnel barriers are homogeneous and that the electrode-barrier interfaces are of almost the same quality.

4.3.2 *Breakdown voltage dependence on annealing temperature*

The thermal and dielectric stability of MTJS are important requirements for memory devices and their integration in the semiconductor process technology. The MTJs were annealed in a vacuum of up to 500^oC and their dielectric stability and TMR were

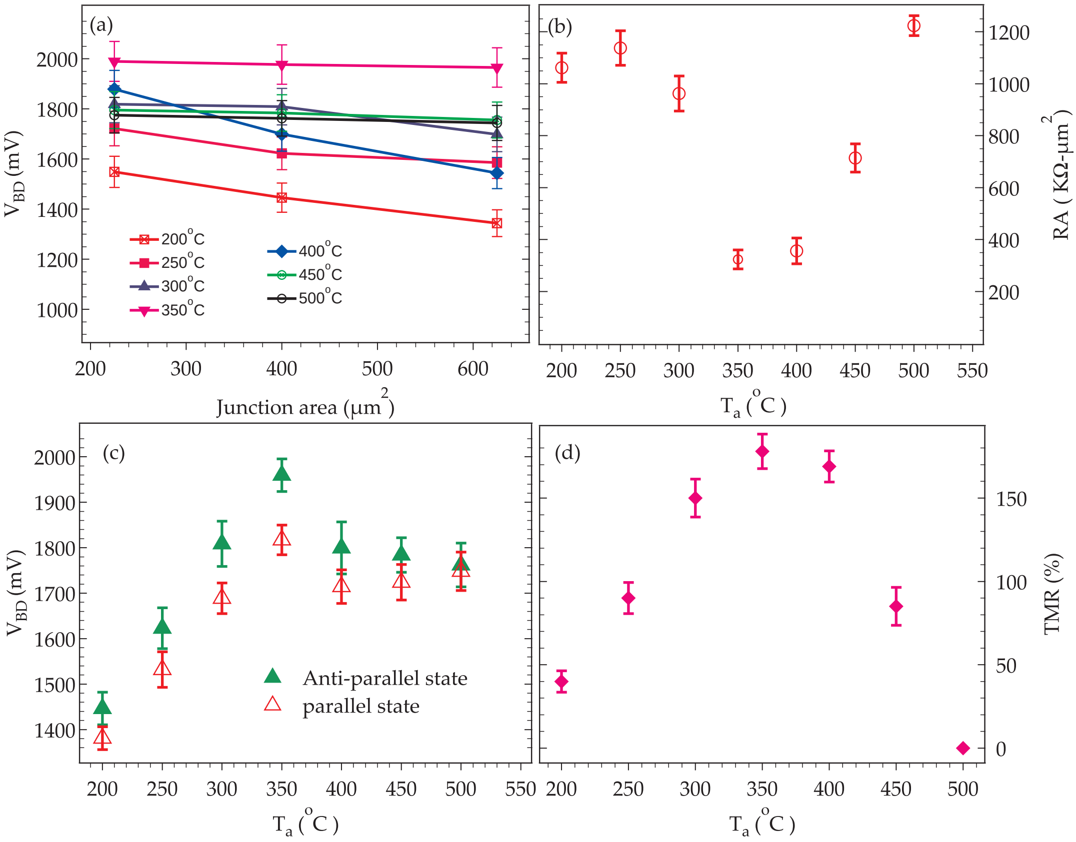

Figure 23: (a) Breakdown voltage dependence on annealing temperature and junction size in AP state. (b) The average RA product in parallel magnetization state as a function of annealing temperature. (c) V_{BD} as a function of annealing temperature for 400μm^2 junction and (d) TMR as a function of annealing temperature. The barrier thickness is 2.1 nm, and the ramp speed is 15 mV/s.

measured at room temperature. Figure 23 exhibits the annealing temperature (T_a) dependence of breakdown voltage, junction area, RA product (for the P electrode allignment) and TMR for the MTJs with 2.1 nm barrier thickness. First, we focus on the dependence of the breakdown voltage on the junction area for different annealing temperatures[Fig. 23(a)].

It was observed that the breakdown voltage depends strongly on the area for annealing of 400 and 200^{o}C. For the optimum annealing temperature of 350^{o}C, the area dependence was smallest. A MTJ with a 2.1 nm thick barrier and 225μm^2 area at 400^{o}C annealing temperature typically breaks at an average value of 1.87

V. By increasing the junction area to 625 μm^2 the breakdown voltage decreased by 18 % to an average value of 1.54 V. For annealing temperatures of 450 and 500^{o}C, the area dependence became smallest.

In Fig. 23(c-d) the annealing temperature dependence on the breakdown voltage and TMR is shown. An increasing V_{BD} and the TMR with increasing annealing temperature of up to 350^{o}C, most likely due to an improvement of the crystallinity of the Co-Fe-B/tunnel barrier interface, was found in all cases. The largest value of V_{BD} coincides with the largest TMR, again pointing to the barrier quality. A rapid decrease of V_{BD} above the optimum annealing temperature (400^{o}C) was observed in both parallel and anti-parallel states. This was found also in an Al-O based junction[50] grown on Si wafer caped with SiO_2 layer. In this case, a strong inhomogeneous temperature-induced crystallite growth was observed, resulting in high mechanical stress acting on the barrier and, accordingly, a reduced V_{BD}. In our MgO-based MTJs investigated here, we might also expect that the reduction of V_{BD} above 350 ^{o}C was connected to additional mechanical stress as a result of recrystallization. It was found that a recrystallization of the Co-Fe-B electrode at the MgO barrier took place[51] resulting in "quasiepitaxial" electrode-barrier interfaces, a prerequisite for coherent tunneling. The corresponding products of the area resistance are given in Fig. 23(b) for different annealing temperatures. A decreasing RA product with increasing annealing temperature up to 350^{o}C might be due to an improvement of the crystallinity of magnetic electrodes. Additional annealing led to an increase in RA product. The temperature stability of TMR and V_{BD} is also closely related to the interdiffusion process upon annealing. Fig. 24 shows the TMR major loop measured at different annealing temperatures. We observed a maximum TMR of 176% for the sample annealed at 350^{o}C. Further, annealing led to lower the TMR ratios with the effect completely vanished at 500^{o}C annealing.

All MTJs in this study have a bottom electrode pinned by an Mn-Ir anti-ferromagnet. Mn diffusion from the anti-ferromagnet to the electrode barrier interface is expected at high annealing temperatures and might be responsible for the drop of TMR ra-

[50] J. Schmalhorst et al., J. Appl. Phys. **91**, 6617 (2002)

[51] J. Schmalhorst et al., J. Appl. Phys. **102**, 053907 (2007); and Y. S. Choi et al., J. Appl. Phys. **101**, 013907 (2007)

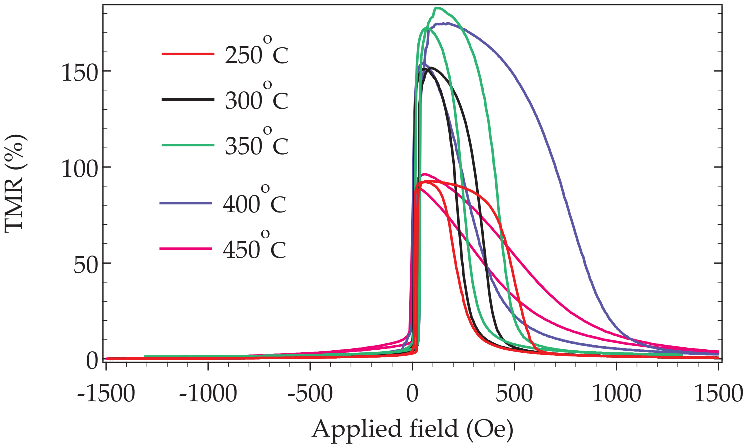

Figure 24: TMR major loop acquired at 10 mV with different annealing temperature. The junction area is $400\mu m^2$ and barrier thickness is 2.1 nm.

tio when T_a exceeds 400 ^{o}C. Evidence of Mn diffusion in Co-Fe-B/MgO/Co-Fe-B junction has been given by Hayakawa *et al.*[52] Using an energy despersive X-ray analysis, they observed a clear Mn peak in the MgO barrier at 375 ^{o}C. The peak intensity was found to be much enhanced after annealing at 450 ^{o}C. In our junctions, the decrease of TMR and the breakdown voltage, and, on the other hand, an increase in RA product above 350 ^{o}C, may be attributed to the Mn diffusion towards lower electrode/barrier interfaces. At 500 ^{o}C, a high level of Mn diffusion to the barrier and bottom electrode barrier interface, due to its affinity for oxygen was expected, leading eventually to the complete deterioration of the spin dependent transport of the devices.

4.3.3 *Influence of the MTJ architecture on the breakdown voltage*

The TDDB results of MTJs with a magnetically hard bottom electrode pinned by an adjacent anti-ferromagnetic Mn-Ir layer were previously presented. Generally, MTJs with such architecture are known as bottom pinned, hereafter, we refer to them as BAF-MTJ. These results were compared with another set of MTJs whose bottom electrode was the free layer and top electrode was an artificial ferromagnet, Co-Fe-B/Ru/Co-Fe, pinned by an antiferromagnetic Mn-Ir layer (see in Fig. 25). This system will be called TAF-MTJ.

[52] J. Hayakawa et al., Appl. Phys. Lett. **89**, 232510 (2006)

Figure 25: Multi-layer layout for bottom pinned (left) and top pinned (right) magnetic tunnel junction

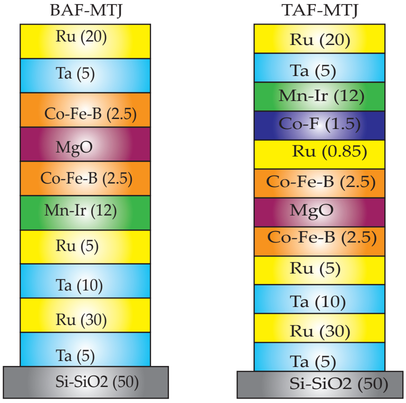

Figure 26: The breakdown voltage dependence on the junction area and voltage polarity for TAF-MTJ with 1.8 nm thick barrier. Each point is an average of five individual measurements, and the error bars represent the standard deviation. The ramp speed was 15 mV/sec.

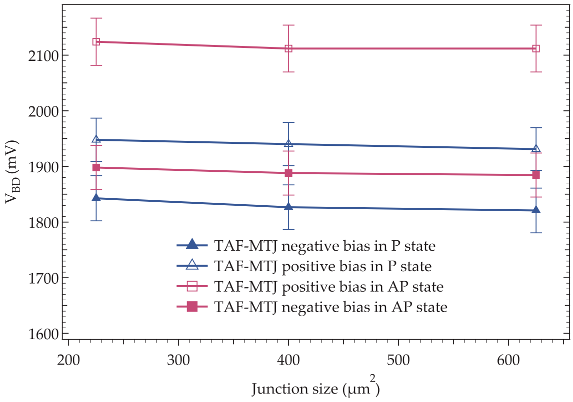

In the present section we will compare the results for both junctions with respect to their dielectric breakdown voltage. Furthermore, inelastic electron tunneling spectroscopy (IETS) was also applied to investigate the spin dependent tunneling process for both top and bottom pinned tunnel junctions as discussed in chapter 6. For TAF-MTJ with a 1.8 nm thick barrier, breakdown voltage as a function of junction area and polarity of applied voltage is shown in Fig. 26.

A comparison of breakdown voltage of TAF-MTJ with BAF-MTJ previously shown in Fig. 19 reveals that for the anti-parallel (AP), as well as the parallel (P) magnetization states, TAF-MTJs had higher breakdown voltages than BAF-MTJs. For example, a BAF-MTJ in anti-parallel magnetization state with a junction area of 225 μm^2 under negative bias typically broke at V$_{BD}$= -1.72 V compared to V$_{BD}$=-1.89 V for a TAF-MTJ having the same junction area. Furthermore, all MTJs showed a higher breakdown voltage for positive than for negative biases; this trend holds for parallel as well as for anti-parallel magnetization alignments. The difference in breakdown voltage of BAF-MTJ and TAF-MTJ in parallel and anti-parallel magnetization states is summarized in table 3.

polarity	parallel state	anti-parallel state
negative bias	260-292 mV	123-143mV
positive bias	270-299 mV	168-189mV

Table 3: The difference $\left[V_{BD}^{TAF-MTJ} - V_{BD}^{BAF-MTJ}\right]$ in AP and P state with voltage bias polarities for 1.8 nm thick barrier.

The difference in the breakdown voltage in the parallel state is generally higher than in anti-parallel states. These general trends were found for MTJs with 1.8 nm thick barrier, and are also valid for TAF-MTJs and BAF-MTJs with a barrier thickness of 2.1 nm. A comparison of breakdown voltage in AP states with 2.1 nm thick barrier is shown in Fig. 27

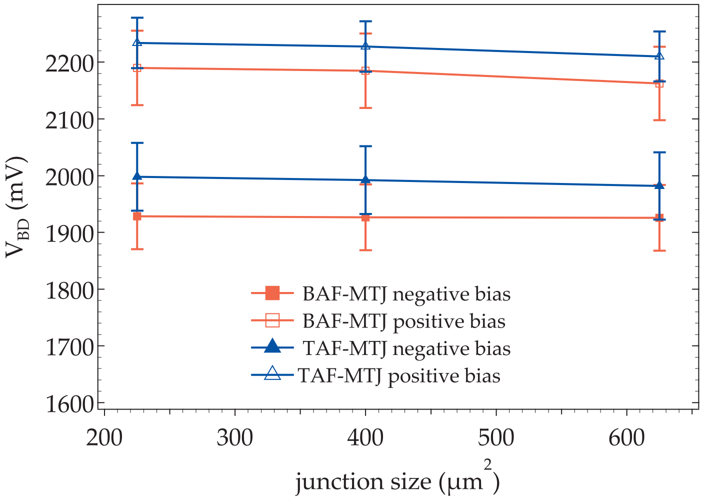

Figure 27: A comparison of the breakdown voltage dependence on the junction area and voltage polarity for TAF-MTJ and BAF-MTJ with 2.1 nm thick barrier. Each point is an average of five individual measurements, and the error bars represent the standard deviation. The data were taken in the anti-parallel magnetization state.

As discussed above, all MTJs showed a higher breakdown voltage for positive bias than for negative bias voltage, i.e., the polarity dependence of the breakdown voltage does not change by changing the layer stack. This indicates that the lower electrode/barrier interface is not equally strong against stress compared to the top interface. This may cause an asymmetry in the bias voltage dependence of electronic transport properties. Therefore, for both sets of junctions, the bias voltage dependence of the electronic transport was probed via a lock-in technique. Precisely, the tunneling current in parallel and anti-parallel states was measured with very high accuracy by inelastic electron tunneling spectroscopy. The differential resistance (dV/dI)-V spectra (discussed in chapter 6) for these junctions revealed an asymmetry for the top pinned system which was reversed in comparison to the bottom pinned system. This indicates that the asymmetries of the transport properties and of the breakdown voltage with respect to the bias voltage polarity have different origins.

We can speculate that the polarity dependence of the V_{BD} voltage is caused by different oxygen concentrations at the lower and upper interfaces between the oxide barrier and the Co-Fe-B electrode. Such an asymmetry can be expected, because it can easily be induced by the deposition process itself: the MgO barrier is directly deposited on top of the Co-Fe-B electrode by RF sputtering from an MgO target. Therefore, the surface of the ferromagnetic electrode can be oxidized by oxygen originating from the target[53,54]. In contrast the interfacial Co-Fe-B at the upper barrier - electrode interface cannot be oxidized in this way. Accordingly, different oxygen concentrations are expected for both interfaces. As mentioned above, the dielectric breakdown is believed to be initialized by a field-induced break of an atomic bond in the oxide. As discussed in detail by McPherson et al.[55], for thin SiO_2 films oxygen vacancies are thought to dominate the breakdown process as precursors for the initial bond breakage. Because it is not possible to determine the atomic arrangement of cobalt, iron, boron, magnesium and oxygen atoms at an atomic level in our junctions, it is difficult to identify the precursors for the breakdown. However, taking the discussion on SiO_2 into account, the influence of a small oxygen distribution asymmetry in the barrier region on the breakdown process is very reasonable.Because this oxygen distribution asymmetry have to be expected for both set

[53] J. Schmalhorst et al., J. Appl. Phys. **102**, 053907 (2007)

[54] J. C. Read et al., Appl. Phys. Lett. **90**, 132503 (2007)

[55] J. W. McPherson et al., J. Appl. Phys. **84**, 1513 (1998)

of junctions, it is reasonable that the, in general, observed higher breakdown voltages for positive bias compared to negative bias result from the expected oxygen distribution asymmetry.

4.3.4 *Dielectric and annealing stability of pseudo spin valve*

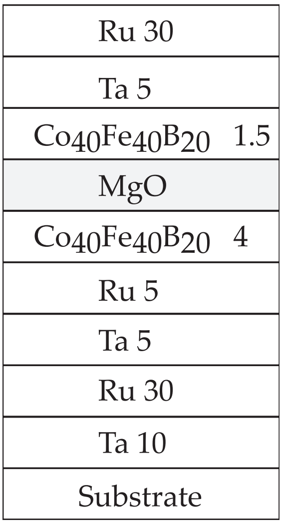

Figure 28: Layer stack of investigated pseudo spin valve MTJs

The dielectric breakdown and annealing temperature stability of a pseudo spin valve (PSV) is investigated here. The layer stack of the investigated sample is shown in Fig. 28. In this study, we fabricated [Co-Fe-B (4 nm)/MgO (2.1 nm) / Co-Fe-B (1.5 nm)] PSV MTJ junctions with a relatively thin top electrode for different coercive fields of the magnetic layers, and studied the evolution of the MR loops and dielectric breakdown over high annealing temperatures up to 500 ^{o} C.

The main advantage of a PSV over exchange biased MTJ is the stacking structure without anti-ferromagnetic pinning layer such as Mn-Ir, which makes it suitable for a very high annealing temperature. This is needed to achieve a good crystallization of the Co-Fe-B electrodes, the MgO barrier and especially of the interface between them. The resulting room temperature MR loops for the subsequently annealed PSV junction are shown in Fig. 29. A good magnetic separation in the anti-parallel state of the two electrodes was found at an annealing temperature of 350^{o}C. This particular sample exhibits the highest TMR ratio after annealing at 400^{o}C. Higher temperatures led to a decrease of the TMR. The strong decrease in these junctions might be related to Ta diffusion towards the upper barrier interface. Surprisingly, at 500 ^{o}C, the behavior of an MR loop completely changed, and nearly hysteresis free MR loops were observed. This behavior is attributed to a transition of the Co-Fe-B upper layer, from the original ferromagnetic state to a superparamagnetic state. Based on micro-structural investigations by transmission electron microscopy (see Fig. 30), we believe that the thin Co-Fe-B layer breaks into magnetic clusters, which behave superparamagnetically, at high annealing temperature.

In Figure 30 (a), the crystalline barrier, grains of crystalline Co-Fe (crystallized Co-Fe-B), and very smooth interfaces are seen. The tantalum shows no structure compared to Fig. 30(b) where the tantalum is diffused completely into a magnetic layer, making

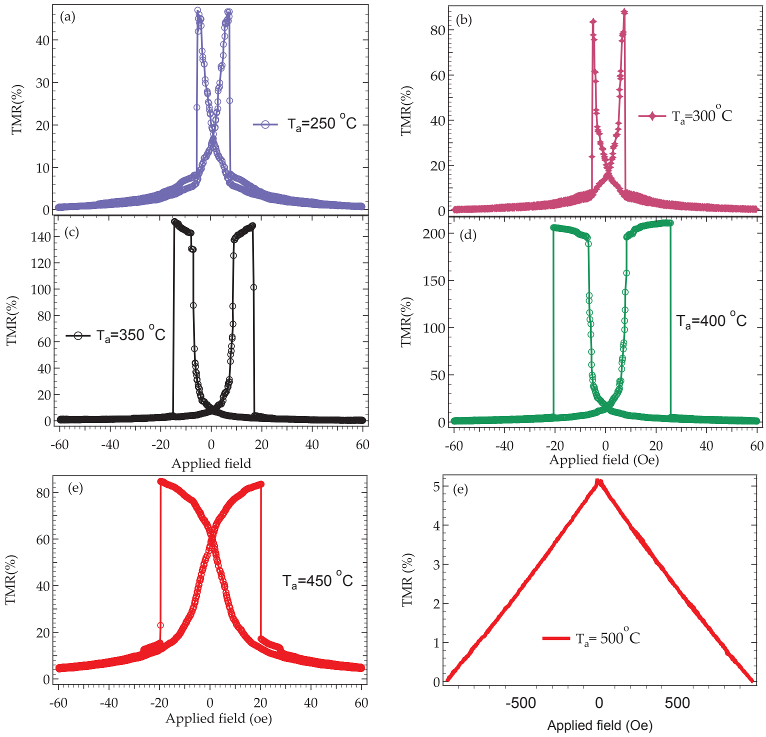

Figure 29: (a-d) Room temperature TMR Loop of pseudo spin valve junctions that were annealed at temperatures between 250 - 450 ^{o}C. (e) A nearly hysteresis free MR loop of PSV MTJ was acquired at 500 ^{o}C.

them amorphous[56]. We performed a time dependent dielectric breakdown measurement to investigate the dielectric reliability of PSV junction as a function of annealing temperatures. An increasing breakdown voltage in a parallel magnetic state with increasing annealing temperature, most likely due to improvement in the crystallinity of the Co-Fe-B electrode/ tunnel barrier interface, was found for all junction areas. A typical behavior of V$_{BD}$ of 400 μm^2 is shown in Fig. 31. The corresponding area-resistance product of these junctions initially decreases with increasing annealing temperature of up to 350^{o}C , and might be due to an improvement in the crystalinity of electrodes. After 350^{o}C, a strong increase in area-resistance gave a sign of strong Ta diffusion, in accordance with our micro-structural investigation.

In contrast to the samples discussed previously that include

[56] S. Ikeda et al., Appl. Phys. Lett. **93**, 082508 (2008)

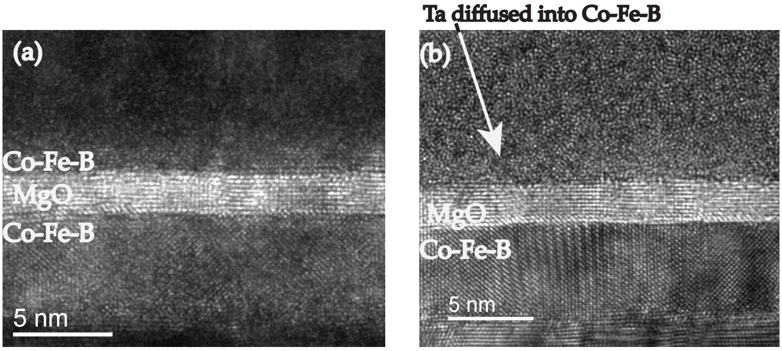

Figure 30: High resolution transmission electron micrographs on 5 nm length scale of pseudo spin valve junctions that were annealed at (a) 400^o C and (b)500^o C.

an Mn-Ir anti-ferromagnetic layer that pinned the hard electrode, an improved dielectric reliability was shown (see Fig.31c), even for the lowest annealing temperatures. This might be due to an improved barrier interface. Moreover, the missing Mn-Ir layer in PSV MTJ might also be the reason for this increase of V_{BD} with increasing annealing temperature. Furthermore, the current density at the breaking point in PSV junction is much higher than ex-bias MTJs of the same thickness, which favor our assumption that the breakdown phenomenon is field dependent.

4.4 Analysis of the experimental data by theoretical models

This section gives a brief overview of the physical background of general mathematical methods used to describe dielectric breakdown. Various mechanisms of dielectric breakdown across silicon oxide in MOS capacitor have been proposed, which are all able to portray data in some areas of the parameter space. In the history of MTJs, the dielectric breakdown was first investigated in 1998 by Wouter Oepts *et al.* [57]. They analyzed their data of aluminum oxide junction with different models proposed earlier for SiO_2. Here, we will analyze our breakdown data of MgO barrier in terms of two specific forms of breakdown probability density, i.e. using the E-model[58] and the 1/E model[59]. Breakdown can be described as a statistical process. Full understanding requires the investigation of large ensembles of nominally identical junc-

[57] W. Oepts et al., Appl. Phys. Lett. **73**, 2363 (1998)

[58] J. W. McPherson et al., J. Appl. Phys. **84**, 1513 (1998)

[59] I. C. Chen et al., IEEE Trans. Electron. Devices **32**, 413 (1985)

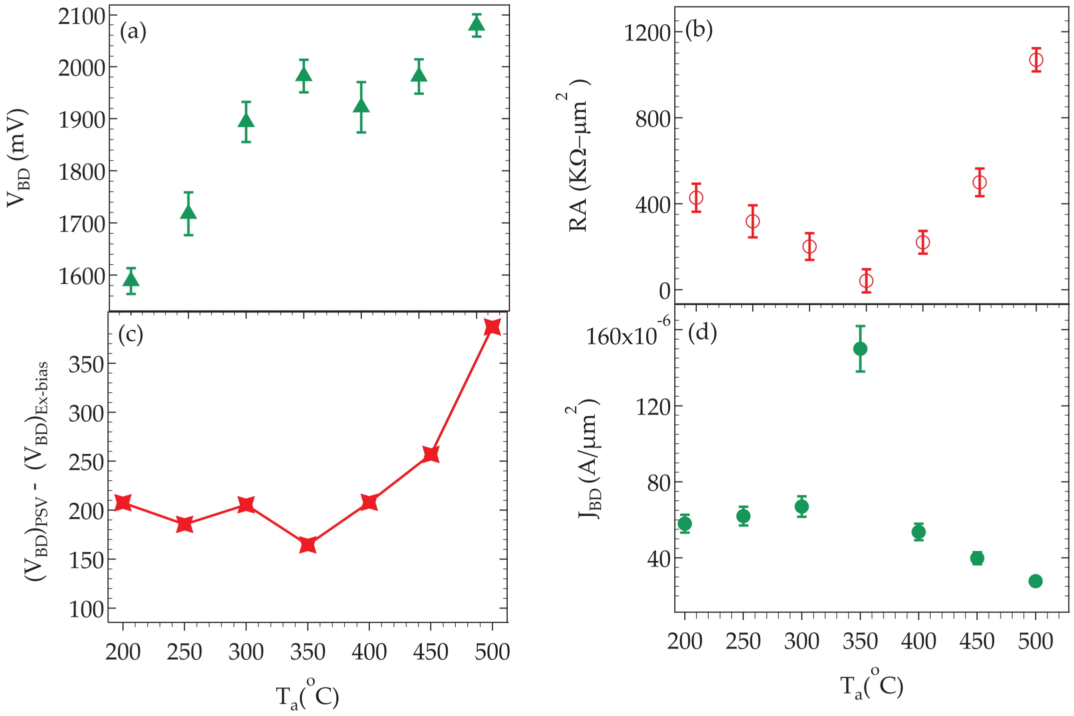

Figure 31: (a) Breakdown voltage as a function of the annealing temperature of the pseudo spin valve junction in parallel magnetic state. (b) The average RA product in parallel magnetic states as a function of T_a. (c) V_{BD} difference of the PSV and exchange coupled bottom pinned antiferromagnetic Mn-Ir junctions in a parallel state. (d) Average current density of PSV junctions at breakdown point for different annealing temperatures.

tions. The breakdown results can be characterized in terms of the fraction F(t) of the ensemble that has shown breakdown at definite time t and is related to breakdown rate f(t)=dF(t)/dt. The breakdown probability density (also known as the failure rate), is defined as the number of junctions that break between t and t+Δt, per increment Δt, as a fraction of those that survived to time t and are mathematically written as[60]

$$p(t) = \frac{F(t+\Delta t) - F(t)}{\Delta t(1 - F(t))} = \frac{f(t)}{1 - F(t)} \qquad (14)$$

By employing F(t) and its derivative, it is easy to show that p(t)= $-\frac{d}{dt}(1 - F(t))$ where, (1-F(t)) represents a fraction of non-failed junctions. In the case of the time independent breakdown probability density, p(t)=p, once obtains (1-F)= exp(-pt), i.e., the non-

[60] M. Ohring, *Reliability and Failure of Electronic Materials and Devices* (Academic Press, 1998)

failed junctions decay exponentially with time. The mean lifetime of the junctions of an ensemble when p(t)=p is:

$$\tau_{1/2} = ln(2)\frac{1}{p} \tag{15}$$

In the literature, the microscopic mechanisms leading to breakdown are divided into two catagories: processes which lead to a gradual change of atomic and electronic structure of the oxide, finally followed by breakdown, and processes which occur as single sudden events. In the first case, breakdown probability density at a certain time depends on voltage time history. In latter cases, it only depends on voltage. When the breakdown voltage is measured by the RVS method then breakdown probability density implicitly depends on a time dependent voltage i.e. p(t)=P(V(T)), and monotonically increases with increasing voltage. We than expect that there is a certain voltage, V_{max}, at which the breakdown rate is at a maximum as a function of time.

The electric field dependent breakdown probability density according to the E model is given as

$$p(t) = Aexp\left(\frac{E(t)}{B}\right) \tag{16}$$

and according to the 1/E model as

$$p(t) = Cexp\left(-\frac{D}{E(t)}\right) \tag{17}$$

The prefactors A and C in eq 16 and 17 are proportional with the junction area if the breakdown probability is independent of the location on the junction area. The expression for V_{max} at which the breakdown rate is at the maximum for the E and 1/E models is given accordingly as

$$V_{max} = Bln\left(\frac{dV}{dt}.\frac{1}{AB}\right) \tag{18}$$

and

$$V_{max} = D\left[ln\left(V_{max}^2\frac{C}{D}\right) - ln\left(\frac{dV}{dt}\right)\right]^{-1} \tag{19}$$

The details of equation 18 and 19 can be found in the Appendix A, and the physical background of the models leading to equations 16 and 17 will be explained later in this chapter.

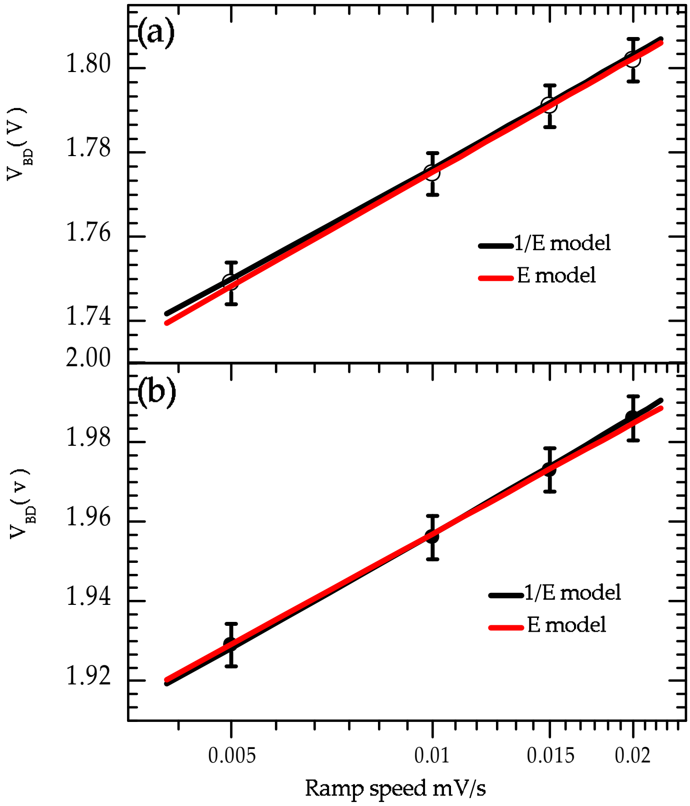

Figure 32: Fits of breakdown voltage according to breakdown probabilities of the E and 1/E models. The barrier thickness was (a) 1.8 nm and (b) 2.1 nm in anti-parallel states with negative biased top electrodes. The junction area was 225 μm^2.

For the 1/E model V_{max} cannot be expressed in closed analytical form and is obvious from Eq.19. We have generally observed a very small scattering of the breakdown voltage for our ensemble of nominally identical MTJs. Therefore, the mean breakdown voltage shown in all figures is assumed to be identical to V_{max}.

In fig 32 we have plotted the ramp speed dependence on the breakdown voltage data for 225 μm^2 junctions. The parameters defined in Eq. 16 and 17 can be extracted by fitting the models according to Eq. 18 and 19 to the data. The results of the fits are summarized in the table 4

A certain area dependence is also expected from eq 18 and 19. As shown as a dotted line in Fig. 33, these area dependencies are consistent with experimental data.

Although both models describe the experimental data very well,

	E model		**1/E model**	
t_B [nm]	A [sec^{-1}]	B [V]	C [sec^{-1}]	D [V]
1.8	2.61×10^{-28}	0.028	1×10^{11}	78.8
2.1	7.32×10^{-29}	0.03	4×10^{11}	87.55

Table 4: Fitting parameters from breakdown probability density of E and 1/E model

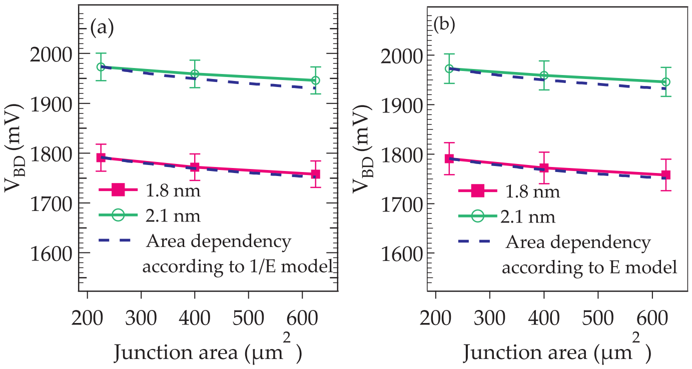

Figure 33: Breakdown voltage dependence on the junction area in AP states for optimally annealed MTJ with 1.8 and 2.1 nm thick barrier. The dotted lines represent the size dependence according to (a)E model and (b) 1/E model

a large difference in extrapolated lifetime is found at lower bias voltages between both models. Fig. 34 shows the extrapolated lifetime curves for both models. At a typical operating voltage of 300 mV, the lifetime for MTJs with 1.8 and 2.1 nm thick barriers for E model (1/E model) can be estimated to 1.8×10^{9} (5.64×10^{42})and 1.4×10^{12} (6.64×10^{42}) years, respectively. These extrapolated values suggest that the applicability of these junctions at low bias voltage is not hindered by a short lifetime.

4.4.1 *Microscopic models*

In this section, the physical background of the theoretical models leading to Eq. 16 and 17 will be elucidated. The microscopic origin of TDDB will be discussed and possible relevance to the breakdown across MgO (MTJs barrier layer) is given. Generally, breakdown models were proposed originally for SiO_2 layer in MOS capacitors where measurements were conducted over a thickness range of 15-40 nm. The voltage applied in the breakdown study was very high compared to the observed breakdown voltage in our MgO based MTJs. Therefore, it is important to

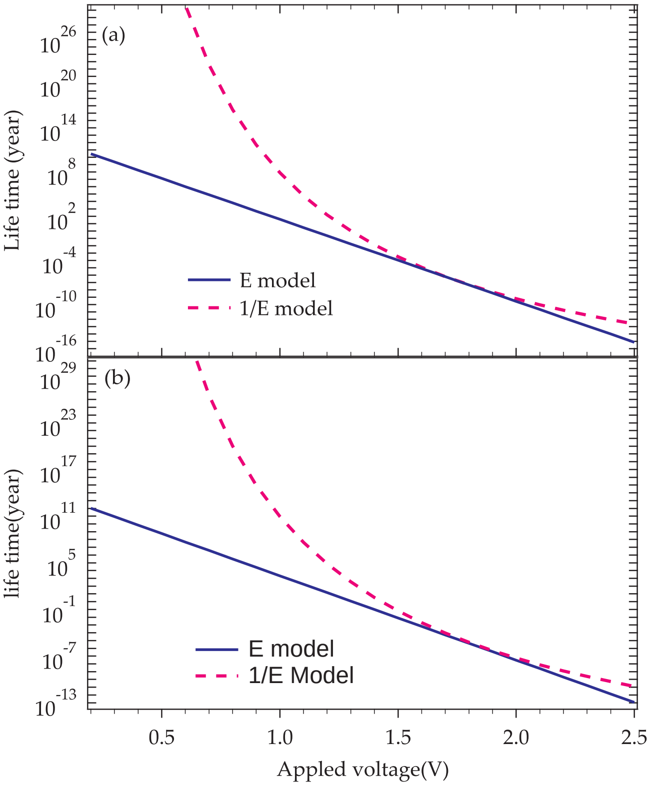

Figure 34: Extracted life time as a function of applied voltage, for both E and 1/E models of (a) 1.8 nm and (b) 2.1 nm thick junction. A large difference in extrapolated lifetime is found at low bias voltage.

evaluate the applicability of these models in the thickness range of our junctions. With respect to the history of the oxide breakdown mechanism, an empirical TDDB model[61] was introduced in the late 1970, which indicated that the logarithm of time to failure is directly proportional to the electric field in the oxide.

$$ln(TF)\alpha\frac{\Delta H_o}{k_B T} - \gamma E \tag{20}$$

Where ΔH_o is the enthalpy of activation of the oxide breakdown, and γ is the field acceleration parameter. This equation was first introduced as an empirical relation but was later a thermochemical foundation and is commonly referred as the E-model[62]. Others have suggested that the breakdown process is current driven and ln(TF) should show a 1/E dependence. This is commonly referred

[61] E. Anolick et al., IEEE IRPS Proc. **17th Annual**, 8 (1979); D. Crook, IRPS Proc. **17th Annual**, 1 (1979); and A. Berman, IEEE IRPS Proc. **19th Annual**, 204 (1981)

[62] J. W. McPherson et al., J. Appl. Phys. **84**, 1513 (1998)

to as a 1/E model[63]. These two models have been used to describe the physics of dielectric breakdown and to predict lifetime. Following, the physics of these models is discussed.

4.4.2 *The 1/E model*

The 1/E model relates the dielectric breakdown to the current induced hole generation when an electron finally reaches at the anode. Early explanations for the current -induced damage of oxides were based on the assumption that a fraction of the tunneling electrons reaching the anode were used to excite the deep valance band electron to a state above the Fermi-level (impact ionization), thereby creating a hot hole which tunnel back into the oxide. This simple explanation had to be modified latter, when operating voltage for the MOSFET device was reduced to below 5V. The motivation behind this modification occurred first, to address the question of how an impact ionization can arise in the SiO_2 when the band gap of SiO_2 is 8.9 eV and second, to extend the 1/E model to lower voltages. It was hypothesized that the accelerated electrons do not actually undergo impaction ionization in the SiO_2, but when they reach the silicon anode the thermalization of these energetic electrons at the anode is believed to produce hot holes which can then tunnel back into oxide, where they can be trapped and create defects in SiO_2[64]. This mechanism of creating defects is usually referred as the anode hole injection. This model is therefore known as an anode hole injection model.

It is strongly believed that most of the holes are likely to pass through the dielectric and are collected at the cathode. However, if there is a weak bond (well above the valence bond), a hole can be captured by the weak bond. The hole fluence is generally smaller than the current density, and the probability of hole generation is directly proportional to the applied voltage[65]. When hole tunneling from the anode is in the Fowler-Nordheim regime, the tunnel hole current is proportional to $E^2 exp(-\frac{D}{E})$, with parameter D (hole generation coefficient) independent of the electric field E. As the density of the holes at the anode is proportional to the current density, the breakdown probability density is give by

[63] I. C. Chen et al., IEEE Trans. Electron. Devices **32**, 413 (1985); J.lee et al., IEEE Trans. Electron. Devices **35**, 2268 (1988); and K. Schuegraf et al., Semiconductor Sci. and Tech. **9**, 989 (1994)

[64] K. F. Schuegraph et al., IEEE IRPS Proc. **31st Annual**, p. 7. (1993)

[65] R. Degraeve et al., IEEE Trans. Electron. Devices **45**, 472 (1998)

$$p(E) = CJ(E)E^2 exp(-\frac{D}{E}) \tag{21}$$

where C is a constant. It is strongly believed in the reliability community that the breakdown probability density p does not depend explicitly on time t for the case of an ultra-thin oxide. Ultra-thin oxide creation of only one trap is sufficent for triggering a breakdown, and evidence of this has been reported by Degrave *et al.*[66] The model claims that the rate of oxide damage is proportional to the hole generation rate and breakdown occurs when a critical amount of damage has been reached. Therefore, the field dependence of the prefactor of the exponential factor is often neglected. Under this approximation Eq. 21 reduces to Eq. 16. Our experimental data of the breakdown dependence on the ramp speed fit nicely using Eq. 16, although the tunneling current density is not explicitly taken into account. However, if the tunnel current is taken into account, the oxide damage rate is proportional to $J(E)\kappa(E)$, where J is the oxide tunneling current and κ is the number of holes created by each tunneling electron. Taking κ to be equal to $\kappa_o exp(-\frac{D}{E})$ [67] and J to be $Aexp(-\frac{B}{E})$ (the E^2 the term in the Fowler-Nordheim model is ignored for simplicity), we can obtain a simple expression for time to the breakdown (t_{BD}) as follows:

$$t_{BD} = \tau_o exp(\frac{G}{E}) = \tau_o exp(\frac{Gd}{V}) \tag{22}$$

Where G= B+D, the sum of the exponential factors in the F-N tunnel current and the impact ionization coefficient and τ_o is a constant depending on material properties. When V_{BD} is measured by the RVS method with a constant ramp speed dV/dt, then the estimation of the voltage at which breakdown occurs is given by[68]

$$V_{BD} \cong \sqrt{\frac{dV}{dt} G\tau_o d \exp(\frac{Gd}{V_{BD}})} \tag{23}$$

As shown in Fig.35, there is a good agreement between experimental results and theoretical projection given in Eq. 23 using the parameter values listed in table 5

Since the ramp breakdown voltage can be projected to t_{BD} for a given voltage by using Eq. 22 no significant difference was found

[66] R. Degraeve et al., Microelectron. Reliab. **36**, 1639 (1996)

[67] M. Knoll et al., J. Appl. Phys. **53**, 6946 (1982); and I. C. Chen et al., IEEE Device Letter **3**, 164 (1986)

[68] E. Rosenbaum et al., IEEE Trans. Electron Devices **43**, 70 (1996)

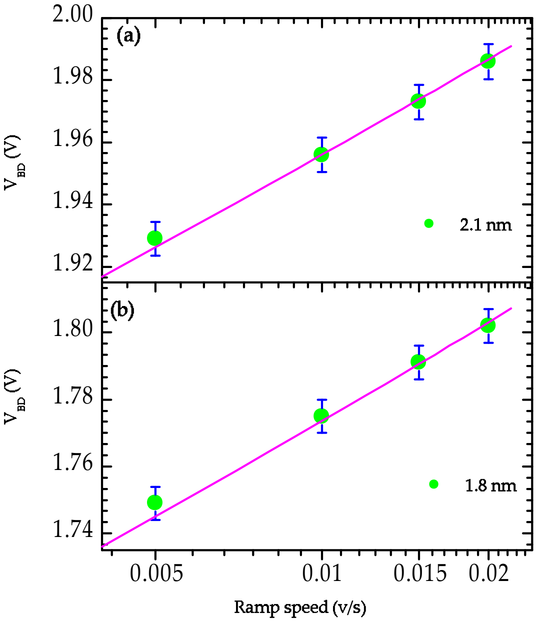

Figure 35: The breakdown voltage dependence on ramp speed for MTJs with barrier thickness of (a)2.1 nm and (b) 1.8 nm. The solid line represents the theoretical projection of Eq. 23 that includes F-N tunnel current and hole fluence due to thermalization of hot electron at anode.

t_B [nm]	τ_0 [sec]	G [MV/cm]
1.8	1.19×10^{-17}	398.55
2.1	1.15×10^{-18}	398.9

Table 5: Fitting parameters when F-N current is included in the breakdown probability density of 1/E model

in the expected lifetime of MTJs was observed when compared with the lifetime projection in the range $0 - 2.5$ V using equ. 4.7 from the Oept's analysis. Both approaches yield nearly the same lifetime at a higher field region (see inset of Fig. 36).

In spite of the good fit as obtained using both approaches, we could not get strong physical arguments in favor of the 1/E model or E-model when applied to our junctions. The facts that confront the legitimacy of the 1/E model as applicable to our junctions are: First, for the case of the ultrathin barrier, the hole tunneling back into the oxide is not expected to be in the Fowler-Nordheim regime, as the range of the applied voltage is less than the height of the barrier. This invalidates the exponential factor in Eq. 16 and 21. Second, the energy of the holes created, which is almost equal to the energy of the tunneling electron, is much less than the height of barrier so that a direct tunneling of hole is expected

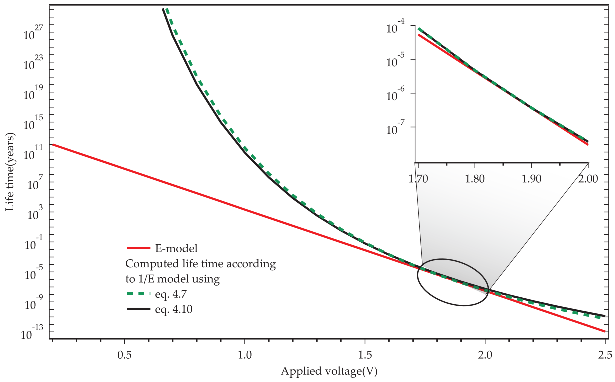

Figure 36: Comparison of the extracted lifetime of a 2.1 nm thick junction according to the 1/E model by using equation 22 and 4.7. Inset shows the extracted lifetime at higher voltages where accelerated tests were performed.

and becomes extremely unlikely. In an ultra thin oxide regime, the mechanism of hole creation is not clear, but for the same reason Dimaria *et al.* have reported that for a SiO_2 based system, the hole tunneling does not occur for applied voltage over a barrier below a certain threshold value, $V_{TH} \approx 5V$[69]. However, for ultra thin films it has been found that the defect generation occurs below this threshold voltage. The rate at which defects are generated are statistical in nature and the rate drops several orders of magnitude as applied voltage decreases[70]. Third, we follow the assumption that the thermalization of the hot electron at the anode produces hot holes which tunnel back into the oxide, where they can be captured and create defects. Then, in case of the PSV, the higher current would produce more holes compared to exchange biased junctions showing a higher area-resistance product and would results in a lower breakdown voltage. However, it was found that the current density at the breakdown point has not a strong impact on the breakdown process. The PSV junctions show higher current densities together with higher breakdown voltage compared to exchange biased junctions. In light of these facts, we are persuaded that the 1/E model is not relevant to the breakdown process of our junctions.

[69] D. J. DiMaria et al., J. Appl. Phys. **80**, 304 (1996)

[70] D. A. Buchanan et al., Appl. Phys. Lett. **65**, 1820 (1994)

4.4.3 The E model

The E-model relates breakdown to the field-induced displacement of atomic bonds in the oxide barrier. Using the concept of thermodynamic free energy consideration, McPherson[71] and Kimura[72] developed a thermodynamical model for dielectric breakdown. Accordingly, when the dielectric is subjected to an electric field, there is a net dipole moment induced which causes a bond distortion. The field-induced strained bond is expected to introduce strong anharmonic coupling with the lattice. The anharmonic coupling allows the strained bond to interact with thermal phonons, increasing the probability of breakdown. The intrinsic failure is thus associated with the physical properties of the oxide and its variation of structures and compositions. Oxides like Al_2O_3 or MgO are ionic in nature. The bonds in these oxides are very polar, e.g. in SiO_2, 60 -70 % of the binding electronic charge is shifted from the silicon to the oxygen atom resulting in a large dipole moment. Significant bond distortion occurs when an electric field is applied because the permanent dipole parallel to the field must grow (by localized lattice distortion) at the cost of the dipole oriented in the opposite direction to the field. If the distortion leads to a bond angle above or below a critical value, the oxygen atom will be displaced and this defect is believed to be the precursor of a breakdown, which will occur when a certain critical density of broken bonds is reached. It is known that for the local electric field, that a molecular bond will experience an electric field equal to the externally applied field plus the dipolar field due to polarization and can be expressed as: $E_{loc}=(1+L\chi)E$, in which L is a Lorentz factor and χ is the electric susceptibility. A molecular model representation of what happens inside the dielectric when an electric field is applied is shown in Fig. 37 [73].

It is evident from the Fig. 37 that in the absence of electric fields all dipoles are in same degenerate state E_o. When the field is applied, the degeneracy is partially removed, with the dipoles oriented parallel to the field at much lower energy levels E_1 relative to those being oriented anti-parallel to the field at energy level E_2. In an effort to lower the dipolar energy and minimize the free energy of the system, dipole flipping to energy state E_1

[71] J. W. McPherson et al., J. Appl. Phys. **84**, 1513 (1998)

[72] M. Kimura et al., J. Appl. Phys. **85**, 7671 (1999)

[73] J. W. McPherson et al., J. Appl. Phys. **88**, 5351 (2000)

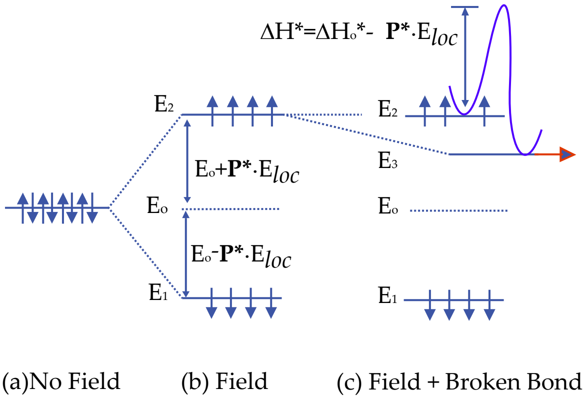

Figure 37: E-model showing how the dipolar degeneracy is partially removed by the electric field: (a) Prior to switching of the field (b) once the field is applied, dipoles oriented parallel to the field have significantly lower energy than those oriented in an anti-parallel state; and (c) some of the dipoles will flip to an orthogonal orientation relative to the field and this is only possible after bond breakage. An activation energy ΔH^{*}=ΔH_{o}^{*} -aE must be supplied thermally for bond breakage.

is expected. The dipolar energy reduces the activation energy for bond breakage. This would results the dipole flipping in order to minimized the free energy of system and is shown in Fig . 37(c). This type of flipping from E_2 to E_3 state is possible only by bond breakage. Thus, from the presence of an electric field parallel and anti-parallel to the two dipole moments, the contribution from the two dipoles to the total energy is decreased and increased, respectively, by an energy $p^{*}.E_{loc}$ where p^{*} is the dipole moment . This energy helps to lower the activation energy for a collapse of anti-parallel dipoles, resulting in the creation of localized electronic defects which give rise to the failure of an oxide. The average time to breakdown due to this process is given by:

$$TF(E) = A_o exp\left[\frac{\Delta H_o^{*} - p^{*}.E_{loc}}{k_B T}\right] = A_o exp\left(\frac{\Delta H_o}{k_B T}\right) exp\left(-\gamma E\right) \tag{24}$$

The details of equation 24 can be found in Appendix B. By assuming that the breakdown probability is independent of time, one can obtain an expression for the breakdown probability density that was used by Oepts in their analysis of breakdown measurements *i.e.* equation 16. The parameter A in Eq. 16 is generally known as attempted frequency (further details in Appendex B) and is proportional to the junctional area. The parameter B is the activation voltage and is related to the field acceleration parameter γ by the relation $\gamma = \frac{d}{B}$, where d is oxide thickness. An extensive study on silicon oxide has been carried out to check the validity of this model by Kimura and it was found that this model provides a good fit to experimental data. The E versus 1/E controversy has continued for many years due to the fact that either model can fit TDDB rather well over limited field ranges. However, there have been several long term low-field TDDB studies published for SiO_2 based capacitor showing that the E model provides a superior fit to the TDDB data, specially at lower fields [74]. The breakdown processes based on the E-model are simple and it is basecally impossible for any ionic material to avoid the effect of stress by the local electric field. Magnesium Oxide (MgO) is more ionic than SiO_2, which leads to a higher dipole moment in the MgO structure and to a higher value of the field acceleration parameter γ. From the fit to our experimental data of a 1.8 nm thick junction, we found B=0.028 V corresponding to field acceleration parameter γ= 6.43× 10^{-8} m/V. This value is approximately a factor of 2 higher than the value for SiO_2 obtained from the Kimura data[75]. An important additional consideration in favor of the applicability of the E model is the fact that there is no threshold value, so that it can be applied at the lower voltages at which we observed breakdown.

4.5 *Conclusion*

We have investigated the dielectric breakdown in MgO-based magnetic tunnel junctions with Co-Fe-B electrodes. Breakdown measurements under positive and negative bias were carried out for MTJs with barrier thicknesses of up to 5.0 nm. When comparing the results for the two bias directions, we found a striking difference: for a positively biased top electrode a larger breakdown voltage was generally observed. This points to an inhomogeneous defect distribution in the barrier. With respect to the annealing temperature, both the TMR as well as the breakdown voltage show a distinct maximum at 350 ^{o}C . Possible reasons for the decrease of breakdown voltage with further increasing annealing temperature were discussed. Finally, we have analyzed our data with the models proposed for a SiO_2 breakdown in SiO_2. For a certain barrier thickness, good fits are possible within both the

[74] J. McPherson et al., IEEE IEDM. **98**, 171 (1998); J. Suehle et al., IEEE Trans. Electron Devices **44**, 801 (1997); and A. Yassine et al., IEEE Electron Device Lett. **20**, 390 (1999)

[75] M. Kimura et al., J. Appl. Phys. **85**, 7671 (1999)

E and 1/E model for the breakdown probability density. The resulting fitting parameters of both models for dielectric breakdown were consistent with the ramp speed as well as the junction area dependence of the breakdown voltage. Extrapolation of lifetime curves of our junctions to lower voltages as obtained from the fits to the experimental data, suggest that the breakdown will not be a limiting factor upon applying these junctions in the next generation of memory devices.

The contents of this chapter has been published in the Journal of Applied Physics[76] in 2008 and 2009.

[76] A. A. Khan et al., J. Appl. Phys. **103**, 123705 (2008); and A. A. Khan et al., J. Appl. Phys. **105**, 083723 (2009)

5

Temperature Dependence of the Tunnel Magnetoresistance

5.1 Introduction

Much interest has been focused on the study of magnetic tunnel junction in view of their potential technological applications since the successful experimental realization of significant magnetoresistance at room temperature[77]. The tunnel magnetoresistive effect (TMR) is such a spin-polarized electronic transport effect, the MTJ devices change their resistance depending on the orientation of the magnetic moment of ferromagnetic electrodes. However, the TMR ratio in MTJs decreases with increasing applied voltage and temperature. With respect to the TMR temperature dependence, it was first noticed by Shang *et al.*[78] that the temperature dependence of the TMR for MTJs greatly exceeded that for non-magnetic junctions with nominally identical barriers. Shang *et al.* explained these results within a simple phenomenological model, in which it was assumed that the tunneling spin polarization P decreases with increasing temperature due to spin wave excitation as does the surface magnitazation. They assumed that both the tunneling spin polarization and the interface magnetization followed the same temperature dependence, the well known Bloch $T^{3/2}$ law, *i.e.*, $M(T)=M(0)(1-\alpha\ T^{3/2})$. In the same year MacDonald *et al.*[79] provided a theoretical justification for these ideas, especially emulating the proportionality between M(T) and P(T), though the microscopic origin was slightly different than that con-

[77] J. S. Moodera et al., Phys. Rev. Lett. **74**, 3273 (1995)

[78] C. H. Shang et al., Phys. Rev. B **58**, R2917 (1998)

[79] A. H. MacDonald et al., Phys. Rev. Lett. **81**, 705 (1998)

sider by Shang *et al.*

Many theoretical explanations of the TMR effect of MTJs are based on model calculations performed for zero temperature and in the limit of a zero bias voltage. Under these conditions, only those processes are included in which the spin of the conduction electron obey laws of conservation of energy and momentum. The net conductance can than be calculated by the summation of individual conductance contributions of all incident electrons. In an elastic tunneling process, each incoming electron has a single corresponding transmitted electron state. Also only the electrons with energy at the Fermi level will contribute to the tunnel current, since only those empty electron states are available in the counter electrode for tunneling. This limits the electron conductance contribution because the number of available states for each incident electron to tunnel into the counter electrode is restricted.

At elevated temperatures or at non-zero bias voltages, however, these assumptions may not be completely valid. The occupation probability of electron states changes with the rise of temperature around Fermi-level, which can be determined by Fermi statistics. The obvious effect of non-zero bias voltage is the change of the form of the barrier (due to change in the position of the Fermi level) and a change of the kinetic energy of transmitted electron compared to that of the incident electron.

In addition to this, at finite temperatures inelastic processes become possible, for which the difference of initial and final energy of the tunneling electron is released as excitation of phonons and magnons, or gained by their absorption. These scattering events lead to new conductance channels. With respect to the TMR amplitude it is of special importance whether new current channels are spin conserving or not. As phonon excitation conserves spin and the resulting conductance channel will have a large influence on TMR. Magnon excitation or absorption leads to a spin flip and thus reduces the TMR[80]. As a result of the additional degree of freedom offered by excess energy, the number of final state available for electron tunneling increases. These inelastic conductance contributions can be visualized by spectroscopic techniques called inelastic tunneling spectroscopy (IETS), as will be discussed in chapter 6. The model presented by Zhang *at el.* is based on a

[80] S. Zhang et al., Phys. Rev. Lett. **79**, 3744 (1997)

two dimensional spin wave excited by tunneling electrons at the insulator ferromagnet interface. They performed a transfer Hamiltonian calculation of the inelastic tunneling conductance resulting from the absorption or emission of spin waves during the tunneling process at elevated temperatures. Han *at el.*[81] further extended this model to explain the TMR temperature dependence of AlO based MTJs by introducing a lower energy cutoff E_c to get a finite number of excited magnons at a non-zero temperature.

Finally, the localized states in the barrier led to new current channels such as resonant tunneling or inelastic hopping via a chain of localized states[82,83]. Depending on the barrier thickness, on the distribution of the electronic states localized in space and energy, and on the temperature and bias voltage, the relative contribution of these additional channels to the total conductance of an MTJ may range from negligible to dominant. The inelastic hopping conductance via chains of localized states might not be spin conserving and thus reduces the TMR with the increase of temperature and/or bias voltage. No theoretical descriptions of the strong temperature dependence of MgO based MTJs including the unpolarized hopping conductance via chain of localized state have been done so far.

In this chapter, we present a systematic study of the area resistance (RA) product and the TMR in Co-Fe-B/MgO/Co-Fe-B MTJs showing a maximal TMR of about 300% as a function of temperature and bias voltage. We will first describe the experimental results of our MTJ (section 5.1) followed by a microstructural investigation of our samples (section 5.2). In section 5.3 we will compare our experimental data with theoretical models. We show that in addition to direct spin-polarized and magnon-assisted tunneling dominating the transport for a barrier thickness of 1.8 nm, the relative contribution of inelastic, unpolarized hopping becomes much more important with increasing barrier thickness. In the last section conclusion is given.

5.2 *Experimental results*

The resistance area product in the parallel (anti-parallel) magnetic state $RA_p(RA_{Ap})$ and the TMR of typical MTJs acquired at 15K

[81] X.-F. Han et al., Phys. Rev. B **63**, 224404 (2001)

[82] Y. Xu et al., Phys. Rev. B **52**, 2843 (1995)

[83] Y. Lu et al., Phys. Rev. Lett. **102**, 176801 (2009)

and 300 K with a bias voltage of 5 mV are listed in Table 6.

Table 6: Typical resistance area product in the parallel and anti-parallel magnetization state and the corresponding TMR measured with a bias voltage of 5 mV at 15 K and 300 K, respectively.

@ 15K			
t_B [nm]	RA$_P$	RA$_{AP}$	TMR
1.8	$110\ \text{K}\Omega - \mu\text{m}^2$	$421\ \text{K}\Omega - \mu\text{m}^2$	283 %
2.1	$346\ \text{K}\Omega - \mu\text{m}^2$	$1.34\ \text{M}\Omega - \mu\text{m}^2$	287 %
3.0	$77.2\ \text{M}\Omega - \mu\text{m}^2$	$311\ \text{M}\Omega - \mu\text{m}^2$	303 %
4.0	$27.5\ \text{G}\Omega - \mu\text{m}^2$	$108\ \text{G}\Omega - \mu\text{m}^2$	293 %
@ 300K			
1.8	$105\ \text{K}\Omega - \mu\text{m}^2$	$291\text{K}\Omega - \mu\text{m}^2$	177 %
2.1	$312\ \text{K}\Omega - \mu\text{m}^2$	$843\text{K}\Omega - \mu\text{m}^2$	170 %
3.0	$44.5\ \text{M}\Omega - \mu\text{m}^2$	$76.7\text{M}\Omega - \mu\text{m}^2$	72.4 %
4.0	$7.13\ \text{G}\Omega - \mu\text{m}^2$	$8.69\text{G}\Omega - \mu\text{m}^2$	21.9 %

These MTJs will be analyzed in detail with respect to their temperature and bias voltage dependence below. Exemplary TMR loops for t_B=1.8 and 4.0 nm measured at 15 and 300 K are shown in Fig. 38

The low temperature TMR is very similar for all barrier thicknesses, but the TMR temperature dependence becomes stronger with increasing t_B. The TMR for a sample with t_B=1.8 nm drops from 282% at 15K to 178% at RT, a decrease from 295% down to 22% is observed for sample with t_B=4.0 nm. A sample with t_B=2.1

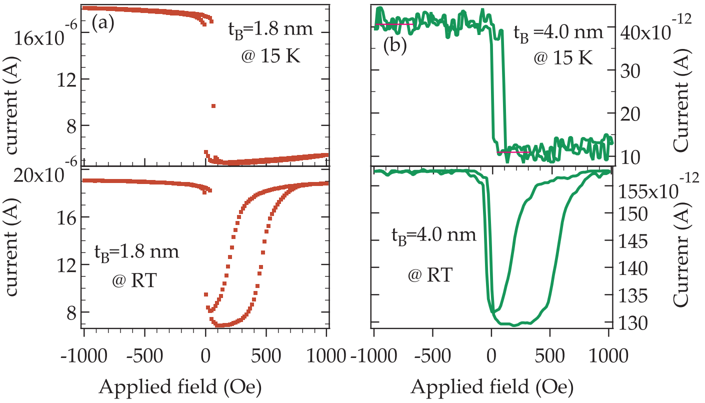

Figure 38: Typical dependence of the current on the applied magnetic field acquired with 5 mV bias voltage measured at 15 and 300 K for t_B=1.8 and 4.0 nm.

nm behaves very similar to a sample with t_B=1.8 nm, a sample with t_B=3.0 nm displays an intermediate behavior (303% at 15K to 72.4% at RT). This strong TMR temperature dependence is evident from Fig. 39(b).

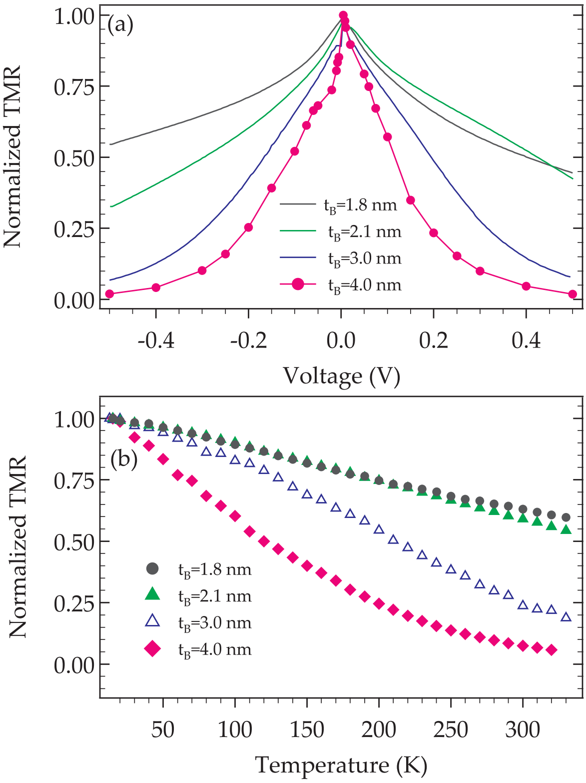

Figure 39: (a) Typical normalized bias voltage dependence of the TMR for t_B=1.8-4.0 nm measured at 15K and (b) typical normalized TMR temperature dependence measured with 5mV bias voltage.

With respect to the TMR temperature dependence, it is worth noting that the generally found reduction of RA products for elevated temperature is always larger for anti-parallel than for parallel magnetic state (see Fig. 40).

Whereas R^p is reduced by a factor of 1.05 only for t_B=1.8 nm between 15K and RT, it goes down by a factor of about 15 for t_B=5nm. Please note that the latter sample showed such a high resistance that it was required to apply a bias voltage of more than 300 mV at low temperature to measure currents above the noise

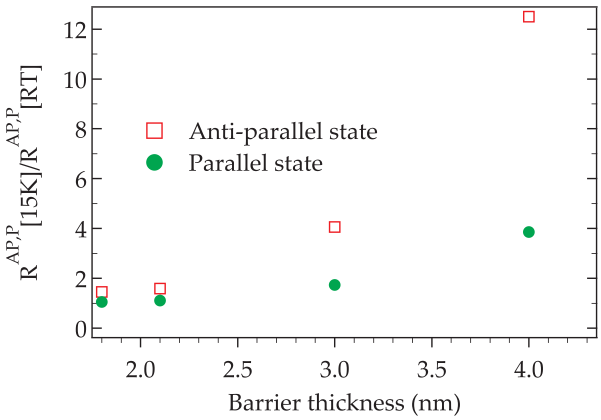

Figure 40: Typical ratio of the junction resistance at low temperature and at RT for anti-parallel and parallel magnetic state as a function of barrier thickness. The low temperature resistance value for t_B=4 nm was estimated as described in the text, the corresponding RT values was extracted by fitting an IV curve (±100 mV) by a linear function.

level of our experimental setup (about 8pA peak-to-peak). Therefore we could not measure the R^{AP} of this sample directly. Instead, we have estimated its RA product to be about 30$T\Omega\mu m^2$ by measuring a low temperature IV curve (bias voltage range: ±500 mV) for sample with t_B=5nm and scaling it by a factor of 10^3 to fit the IV curve of a sample with t_B=4.0nm in the parallel magnetic state. The corresponding resistance of the sample with t_B= 5.0 nm at RT was still too high to be measured directly with 5mV bias voltage, but a value of 2$T\Omega\mu m^2$ could be extracted by fitting an IV curve (± 100 mV) by a linear function. As expected for quantum mechanical tunneling, the low temperature RA product depends exponentially on the barrier thickness: by fitting the logarithm of RA with a linear function ($\ln[RA_P(t_B)] = \gamma + \alpha t_B$) an exponential prefactor of α= 6.1 ± 0.2 nm^{-1} was found which matches quite well with the data of Yuasa et. al.[84] (α= 6.41nm^{-1}) who deposited their MgO barriers by electron beam evaporation instead of RF sputtering. The low temperature bias voltage dependence of TMR (see Fig. 39(a)) shows the same trend as the TMR temperature dependence, it becomes much stronger with increasing barrier thickness. Particularly, the TMR of sample with t_B=4.0 nm nearly vanishes for bias voltage $|V| \geq 500$ mV. We could not measure any TMR for a sample with t_B=5.0 nm, but this is reasonable: taking the result for the thinner MgO barriers into account, it can be assumed that the

[84] S. Yuasa et al., Nat. Mater 3, 863 (2004)

TMR bias voltage and temperature dependence for t_B=5nm is at least as large as for t_B=4nm. Therefore the minimum bias voltage and/or temperature required to get a fair current is so large, that the TMR must be expected to vanish at these minimum values. Another possibility to decrease the absolute resistance of an MTJ to prepare much larger junctions. However, it was not possible to increase the junction size sufficiently (by a factor of about 1000), since all of these extremely large MTJs samples with t_B=5.0 nm showed extrinsic shorts. However, the TDDB study of junctions as discussed in previous chapter, substantiate the dielectric stability of the oxide which conserved at least up to t_B=5.0 nm.

5.3 Microstructural investigation

To understand the origin for the different bias voltage and temperature dependences for different MgO thickness, microstructural investigations have been performed for t_B=2.1 and 4.0 nm. The transmission electron micrographs of Figs. 41(a) and 41(c) show a good morphology of the MTJ structures with quite smooth interfaces in the overviews.

The enlarged HRTEM images in Figs. 41(b) and 41(d) indicate partial crystallization of Co-Fe-B during the postannealing at 350^0 C.[85] The MgO tunnel barrier grown on the Co-Fe-B layer showed a good crystalline structure. Moire fringes are observed that point to growth in 5-20 nm sized epitaxial columns with small tilting angles out of plane of the MgO (001)-oriented crystallites.[86] The crystal lattice of the MgO can be clearly identified from the lower interface up to the upper interface for both samples. Therefore, the tunnel barrier and the electrode-barrier interfaces of both junctions seem to be of almost the same quality, in accordance with the similar low-temperature/low bias voltage TMR amplitudes of both samples and with the linear barrier thickness dependence of the dielectric breakdown voltage.

However, the HRTEM investigations do not give any information on the density of the localized electronic defect states in the barrier. As RF sputter deposition from an MgO target is used where the deposition condition are constant throughout the full layer and as the barrier seems to be homogeneous in the HRTEM

[85] G. Eilers et al., J. Appl. Phys. **105**, 073701 (2009)

[86] G. X. Miao et al., Appl. Phys. Lett. **93**, 142511 (2008)

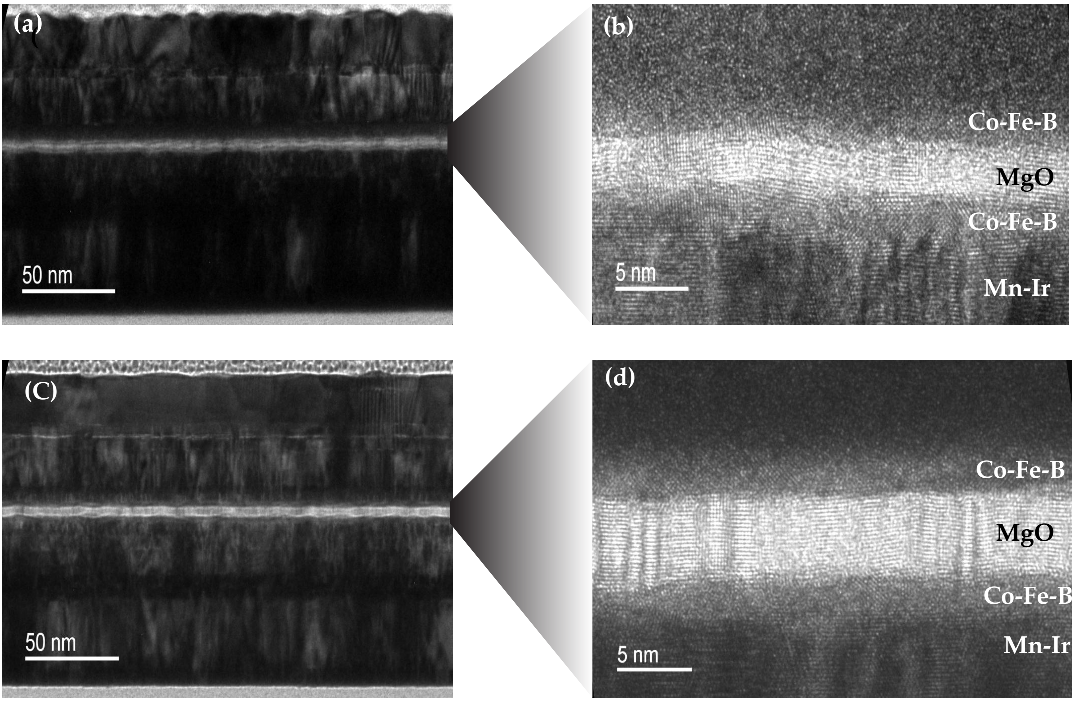

Figure 41: Transmission electron micrographs of magnetic tunnel junctions. (a) and (c) Low magnification image for t_B=2.1 and 4.0 nm. (b) and (d) High resolution images for t_B=2.1 and 4.0 nm.

images, it can be assumed that the number of defects per unit volume is constant in first order. The influence of defect states on the transport properties will be discussed in the next section.

5.4 Theoretical models

In this section, three conspicuously different model proposed in the literature for the mechanism of this TMR temperature dependence are discussed. The present discussion is based on the experimental results for the prepared MgO based MTJs. For these the temperature dependent behavior is different compared to Al-O based junctions. This gives reason to compare different models, which leads to the selection of a physically reasonable model.

5.4.1 Shang model

For a typical AlO based junction, the temperature dependence was first analyzed using a model proposed by Moodera *et al.*[87] and in more detail by Shang *et al.*[88] This model, based on Jullière's model[89], has a direct temperature dependent spin polarization of the ferromagnetic electrodes. The conductance G of the tunnel junction is assumed to consist of two independent conduction channels: a contribution G_d due to direct tunneling and a contribution G_{UP} due to un polarized tunneling via defect states in the oxide barrier. The latter contribution was assumed to be phonon assisted and therefore absent at zero K. It was assumed that the only direct tunneling contribution depends on the angle θ between the magnetic moment of the two electrodes. Thus the conductance is written as:

$$G(\theta) = G_d(\theta) + G_{UP} \tag{25}$$

with

$$G_d = G_T \times (1 + P_1 P_2 cos\theta) \tag{26}$$

where P_1 and P_2 is the effective tunneling electron spin polarization. and prefactor G_T is the average direct elastic conductance for parallel and anti-parallel alignment of the electrode magnetization. The elastic direct tunnel conductance varies slightly with T due to a broadening of the Fermi distributions in the electrodes. The relative increase of the direct elastic conductance with increasing temperature has been calculated and is given by[90]

$$\frac{G_T(T)}{G_o} = \frac{CT}{sin(CT)} \tag{27}$$

where G_o is the conductance at zero temperature and C is give by C=1.387 × 10^{-4} $d/\sqrt{\phi}$, with the barrier width d in and an average barrier height ϕ in eV. They assumed that P decreases with increasing temperature due to spin-wave excitation (Bloch's law),

$$P(T) = P_o(1 - \alpha T^{3/2}) \tag{28}$$

where α is material-dependent constant, and P_o is the full effective spin polarization at T=0 K. If only direct tunneling is taken into

---

[87] J. S. Moodera et al., Phys. Rev. Lett. **80**, 2941 (1998)

[88] C. H. Shang et al., Phys. Rev. B **58**, R2917 (1998)

[89] M. Julliere, Phys. Lett. **54A**, 225 (1975)

[90] R. Stratton, J. Phys. Chem. Solids **23**, 1177 (1962)

account, then the conductance in parallel and anti-parallel states for our MTJs ($P_1 = P_2$) can be given as:

$$G_P = G_T(1+P^2) = G_T(1+P_o^2(1-\alpha T^{3/2})^2) \tag{29}$$

$$G_{AP} = G_T(1-P^2) = G_T(1-P_o^2(1-\alpha T^{3/2})^2) \tag{30}$$

Here G_T is the coefficient for direct tunneling and is considered to be constant. It is easily seen from equation 30 that the anti-parallel conductivity increases with rising temperature. In the parallel case, the conductivity is falling with temperature. But impressively a small increase of the conductivity in a parallel state with rising temperature is found in magnetic tunnel junctions[91] with Al-O barrier. To explain these results, an additional unpolarized term G_{UP} is introduced to the model (see Eq. 25). This additional conductance must have a temperature dependence which shows a strong increase in conductivity to compensate for the basic $dG_P/dT < 0$ behavior. Shang et al. proposed that this additional contribution could be from electrons hopping through localized states. This would also fit with the observed power law dependence on the temperature.

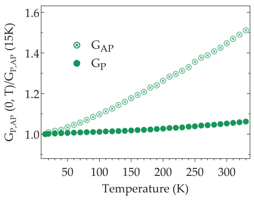

Figure 42: Typical temperature dependence of conductance for t_B= 1.8 after normalization by conductance at 15K

However, this model cannot hold for MgO based junctions because of the very small overall change of conductance in the parallel state as shown in Fig. 42. If different junctions with high TMR ratios are investigated, the model gives a larger temperature dependence of the conductivity in both magnetic states. Therefore, the spin-independent term in this model must also be larger to compensate for the stronger basic $dG_p/dT < 0$ tendency. One would assume that a larger TMR ratio is linked to a junction of better quality with regard to barrier structure and magnetism. A spin independent term has the tendency of lowering the TMR and is a sign of an inferior quality barrier. Then it would be very unlikely that a spin independent term could be higher in a magnetic tunnel junction with higher TMR, especially in the case of a thinner barrier. Therefore, this model is not able to give a complete physical explanation of the temperature dependence of TMR for the MgO based MTJs.

[91] J. Schmalhorst et al., Phys. Rev. B **68**, 224437 (2003)

5.4.2 Magnon assisted tunneling model

A second model on the dependence of TMR on the temperature was developed by Zhang *et al.*[92] This theory is based on two dimensional spin waves excited by tunneling electrons at the interface between the insulating barrier and the ferromagnet electrode. This model was extended later by introducing a lower energy cut-off E_c to get a finite number of excited magnons at a non-zero temperature.[93] It also provide an explanation for the dependence of TMR on the applied bias voltage. A surface magnon can be emitted or absorbed by a tunneling electron, opening additional conductance channels. Because of angular momentum conversation, the spin of this electron has to be flipped and it contributes to another spin-channel. Therefore the overall conductance is always a mixed state of both magnetic alignments of the ferromagnetic electrodes if magnons are excited which leads to reduce the TMR.

Drewello *et al.*[94] extended this model by introducing thermal smearing and applied it successfully to MgO-based MTJs although coherent tunneling is not explicitly taken into account in this model. The motivation for the extension was the very general experimental result, that the temperature dependence of the resistance in the parallel state in MgO-based junction was so small, that the additional increase in conductance due to a broadening of the Fermi level when the temperature of the junction increases, could not be neglected. However, this effect could be neglected for AlO based junction with strong temperature dependence caused by other effects. The total conductance for a given temperature T and bias voltage V is described as a sum of the contributions from direct elastic tunneling and from magnon-assisted tunneling, the conductance can be written as :

$$G^{\gamma}(V,T) = G^{\gamma}_{dir}(V,T) + G^{\gamma}_{mag}(V,T) \tag{31}$$

Where γ =(AP,P) describes the magnetic state of the MTJ, G_{dir}(V,T) is the direct elastic tunneling conductance and G_{mag}(V,T) is the magnon-assisted inelastic conductance. The TMR amplitude is defined as TMR(V,T)=(G_P(V,T)-G_{AP}(V,T))/ G_{AP}(V,T). Taking thermal smearing into account the temperature dependence of the to-

[92] S. Zhang et al., Phys. Rev. Lett. **79**, 3744 (1997)

[93] X.-F. Han et al., Phys. Rev. B **63**, 224404 (2001)

[94] V. Drewello et al., Phys. Rev. B **77**, 014440 (2008)

tal conductance in the limit of zero bias is then given as:

$$G^{\gamma}(0,T) = G^{\gamma}(0,0)\frac{CT}{sinCT}\left[1 + Q\beta^{\gamma} ln\left(\frac{k_B T}{E_c}\right)\right] \qquad (32)$$

In Eq. 32 C characterize the strength of thermal smearing. E_c is the lower magnon cut-off energy and parameter β^{γ} is defined as β^P=2Sk_BTξ/E_m and β^{AP}=2Sk_BT/ξE_m for the parallel and antiparallel magnetic configuration respectively, with S being the spin parameter and E_m is related to Curie-temperature T_C of the ferromagnetic electrode. ξ is the ratio of conductance in both states ξ =G_{AP}(0,0)/G_P(0,0)=R_P(0,0)/R_{AP}(0,0). The parameter Q describes the probability that magnons are involved in the tunneling process, it directly depends on the ratio of the squares of the transfer matrix elements for direct (T^d) and magnon-assisted transfer(T^J): Q=$[(\left|T^d\right|^2/\left|T^J\right|^2)+2S^2]^{-1}$. The bias voltage dependence of the TMR in the limit of zero temperature is given accordingly as

$$TMR(V,0) = TMR(0,0) - Q\frac{SeV}{E_m}\frac{R_{AP}(0,0)}{R_P(0,0)}\left(\frac{1}{\xi} - \xi\right) \qquad (33)$$

As mentioned above the temperature and bias voltage dependence becomes much stronger with increasing barrier thickness. Further, it was not possible to fit the data for T_B=2.1, 3.0, and 4.0 nm self-consistently by Eqs. 32 and 33 only we will come back to this point below. Therefore, we propose to take an additional unpolarized conductance G_{UP}(V,T) into account, which will lead to very reasonable results. For this, Eq. 31 is amended by an additional term,

$$G^{\gamma}(V,T) = G^{\gamma}_{dir}(V,T) + G^{\gamma}_{mag}(V,T) + G_{UP} \qquad (34)$$

In contrast to the TMR, it is obvious that the difference ΔG(V,T) between the total conductance in the parallel and in the antiparallel state is not changed by this additional unpolarized term. In the limit of zero bias it is given by

$$\begin{aligned} \Delta G(0,T) \quad = \quad & \frac{CT}{sinCT}\left\{[G^P(0,0) - G^{AP}(0,0)] + \frac{2QSk_B}{E_m}T\right. \\ & \left.\left[\xi G^P(0,0) - \frac{G^{AP}(0,0)}{\xi}\right] ln\left(\frac{k_B T}{E_c}\right)\right\} \qquad (35) \end{aligned}$$

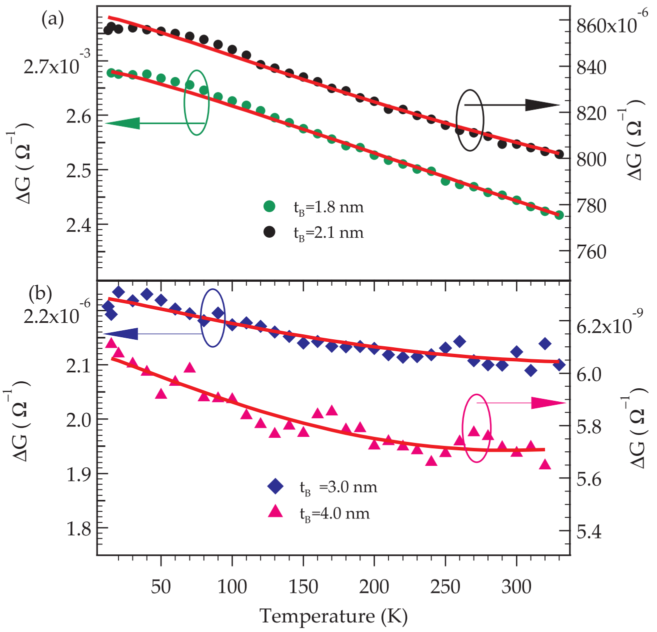

Figure 43: Typical temperature dependence of ΔG for all four samples with t_B= 1.8, 2.1 nm (a) and 3.0, 4.0 nm (b). The red solid lines are the fits according to Eq. 35.

The self-consistent fitting procedure of our data will now be described. Eq. 35 was used to fit ΔG(0,T) for all four samples *simultaneously* (see Fig. 43) under the constraint that the measured bias voltage dependence of the TMR (average of data for positive and negative bias voltage) for t_B=1.8 nm is reproduced best by Eq. 33 for this barrier thickness it is known that the magnon-assisted tunneling model can nicely explain the temperature and the bias voltage dependence of the TMR,[95].

Table 7: Parameters for fitting $\Delta G(0,T)$ of all four sample by Eq.35 under the constraint that the bias voltage dependence of the TMR of sample with t_B=1.8 nm, described by Eq.33, is reproduced best. Technically this was achieved by fixing C' to different values, fitting $\Delta G(0,T)$ for all four samples *simultaneously* and finally checking if the corresponding QS/E_m value for sample with t_B=1.8 nm can reproduce the measured bias voltage dependence of the TMR at low temperature. The best fit of the bias voltage dependence of sample with t_B=1.8 nm and $\Delta G(0,T)$ for all samples was achieved for $C' = 6.85 \times 10^5 K^{-1} m^{-1}$. The corresponding value for the low energy cut off energy was $E_c = 0.16 \pm 0.15 meV$.

MgO thickness	QS/E_m $[eV^{-1}]$
1.8 nm	0.035± 0.006
2.1 nm	0.029 ± 0.005
3.0 nm	0.034 ± 0.006
4.0 nm	0.050 ± 0.009

Because of the very similar MgO-barrier interface quality in all junctions (see Sec. III B) the low-energy cut-off energy E_c is ex-

[95] V. Drewello et al., Phys. Rev. B 77, 014440 (2008)

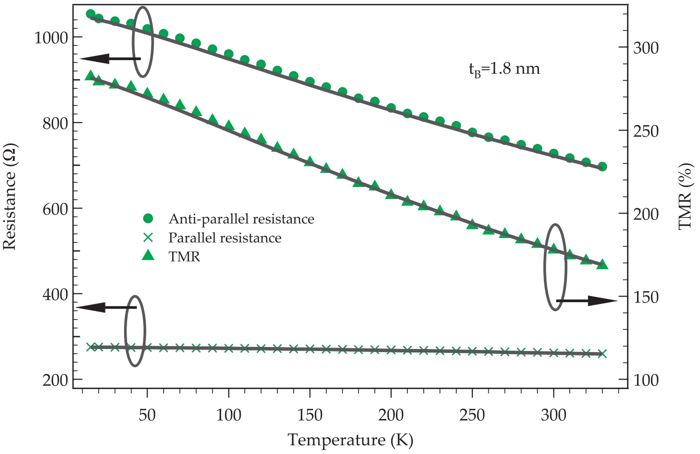

Figure 44: Fit of the resistance in the parallel and anti-parallel state of the MgO based MTJs. The resulting fit of the TMR is also shown on the right. The magnon model including thermal smearing (Eq.32 and Eq.33) is used.

pected to be identical for all samples. Furthermore, C is expected to show the mentioned linear dependence on the barrier thickness t$_B$ and can therefore be rewritten as $C = C' \times t_B$ with C' being identical for all samples. Furthermore, we use individual values of QS/ E$_m$ for all samples to account for a possible thickness dependence of this parameter describing the magnon-assisted processes. The results of the self-consistent fits are summarized in table 7

It is important to mentioned here, that the extracted C' value corresponds to a mean barrier height of 4.1 eV which is close to the half of the MgO band gap of 7.8 eV.[96] This gives additional support for the self-consistency of our model.

For t$_B$=1.8 nm the fitting parameters given in Table 7 can be inserted in Eq. 32 to reproduce the total conductance G^{P,AP}(0,T) in the parallel and the anti-parallel state very well [see gray lines in Fig. 43]. This shows that direct spinpolarized and magnon-assisted tunneling dominates the transport for a barrier thickness of 1.8 nm.

For t$_B$≥ 2.1 nm the experimental data for G^{P,AP}(V= 0,T) cannot be reproduced in this way, an additional temperature dependent current contribution needs to be taken into account. Because the magnon-assisted tunneling model can self-consistently reproduce

[96] R. C. Whited et al., Sol. St. Communications **13**, 1903 (1973)

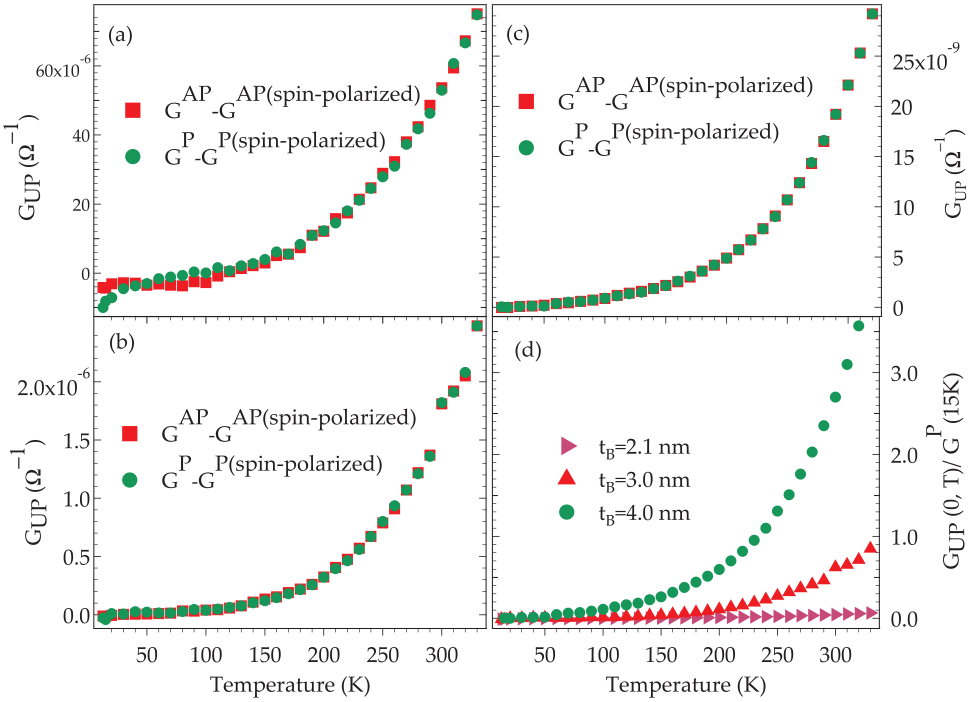

Figure 45: Typical temperature dependence of G_{UP}(0,T) for (a) t_B=2.1 nm, (b) 3.0 nm, and (c) 4.0 nm. The green circles (red squares) correspond to the calculation starting with conductance in the parallel (anti-parallel) state. In (d) the data resulting from G^P(0,T) are shown after normalization by GP(15 K).

ΔG for all samples, this additional current contribution should be unpolarized. It can be calculated by subtracting $G^{P,AP}$(V=0,T) according to Eq. 34 from the experimental data. As expected, these differences are nearly identical for parallel and anti-parallel alignment (see Fig. 45). In other words this is the justification for the extra term $G_{UP}(V,T)$ in Eq. 34.

The relative contribution of inelastic unpolarized hopping becomes much more important with increasing barrier thickness, which becomes obvious from Fig. 45 (d) showing the typical temperature dependence of $G_{UP}(0,T)$ for t_B= 2.1, 3.0 and 4.0 nm normalized by $G^P(0,0)$. This is therefore the reason for the strong decrease of the TMR in these MTJs. The dependence of unpolarized conductance on temperature and barrier thickness was analyzed and found to be in remarkably good agreement with the theory of Glazman and Matveev[97]. Details of the procedure can be found in Appendix C. After including the additional unpolar-

[97] L. I. Glazman et al., Sov. Phys. JETP **67**, 1276 (1988)

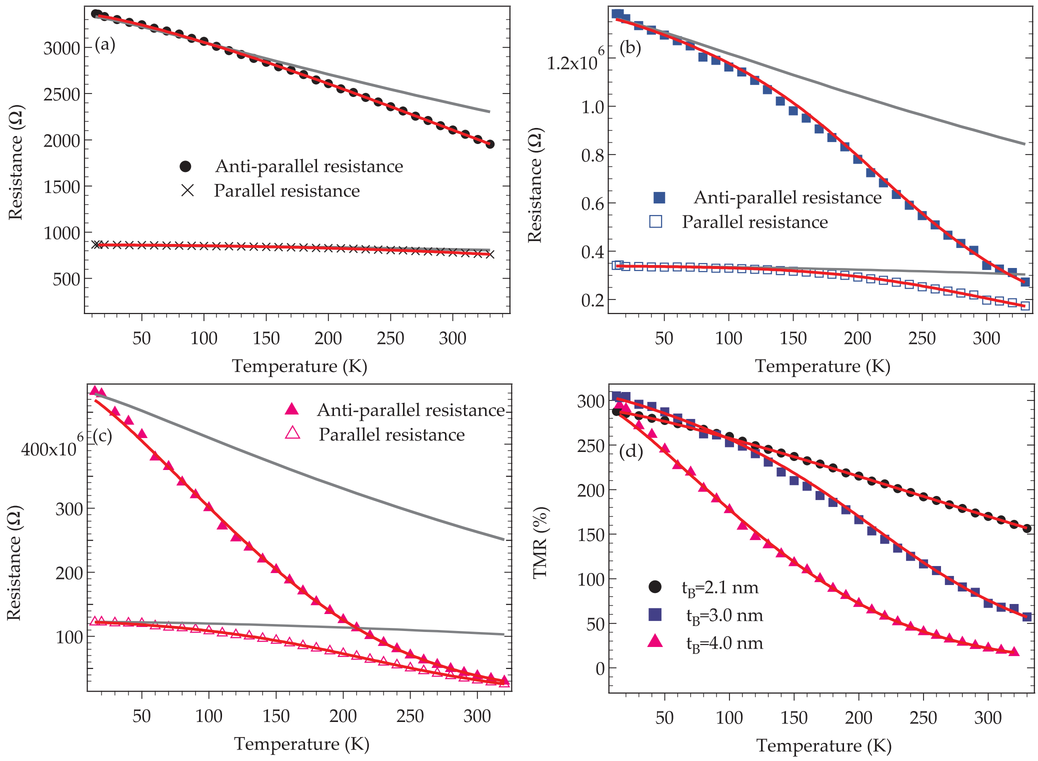

Figure 46: Typical temperature dependence of the TMR, and the resistance for t_B=2.1, 3.0 and 4.0 nm. The junction area is 225 μm^2. The red solid lines are the fits of $R_{P,AP}$ according to Eq. 34. The gray solid lines are the resulting simulations according to Eq. 32, e.g., if only direct and magnon-assisted tunneling would be taken into account.

ized tunnel conductance, the resulting fits can well reproduce the observed temperature dependence of the TMR and the area resistance products (see red solid lines in Figs. 46).

5.4.3 *Spin-polarized hopping model*

As an another attempt to explain the TMR temperature dependece in MTJs with a high degree of spin polarization, Lu *et al.*[98] proposed an extension of the Glazman-Matveev theory to the case of ferromagnetic reservoirs to account for spin-polarized inelastic tunneling through nonmagnetic localized states embedded in an insulating barrier. Lu *et al.* demonstrated that in MTJs with high TMR such as Co-Fe-B/MgO/Co-Fe-B MTJ, temperature driven

[98] Y. Lu et al., Phys. Rev. Lett. **102**, 176801 (2009)

spin-conserving inelastic processes through chains of localized states may exist and would lead to reducing the magnetoresistance effects. The extension of Glazman-Matveev theory adapted to spin-polarized reservoirs could be used to fit both conductance and TMR vs T. Their main motivation for the assumption of spin-polarized hopping conductance was the experimental observation that ΔG(T) increased with increasing temperature for MTJs with 4-nm-thick MgO barrier which in in contradiction to our result (see fig.49). We have also applied this model to our data. The first step was to fit the conductance in the anti-parallel state by a function of the form

$$G^{AP}(0,T) = \sigma_o + \sum_{N\geq 2}^{N_{max}} \sigma_N T^{N-2/(N+1)} \tag{36}$$

The parameters σ_N describing the contribution of hopping via N localized states to G^{AP}(0,T) are used as free parameters. From the fit by Eq. 36 to experimental data it is possible to extract the different N-LS conduction chains from their specific thermal fingerprint.

For a sample with t_B=1.8 and 2.1 nm, the data can be fitted by taking chains up to N=2 and N=3, respectively. For the sample with t_B=3.0 and 4.0 nm higher order hopping chains were required: for this we have adopted the fitting procedure as described by Xu. *et al.* [99], i.e. we have first restricted the fit to a temperature range that can be best fitted by taking chains up to $N = 2$ only into account. Then the temperature range has been increased so far that it can be best fitted by a function with one additional term and so on. By so doing, the data for a sample with t_B=3.0 and 4.0 nm in the entire temperature range up to 330K could be fitted with a function containing terms of up to N=6 and N=7, respectively. The results for all four samples are shown in Fig.47 (a, c, e, g), the corresponding fitting parameters for all samples are summarized in Table. 9 [see on page 97]. The corresponding relative contribution W_N of different N-LS chains to the anti-parallel conductance for sample with t_B=3.0 and 4.0 nm are shown in Fig. 47 (b, d, f, h). Please note that resonant tunneling ($N = 1$) is expected to be T-independent and can therefore not be distinguished from direct tunneling ($N = 0$). In this sense the

[99] Y. Xu et al., Phys. Rev. B **52**, 2843 (1995)

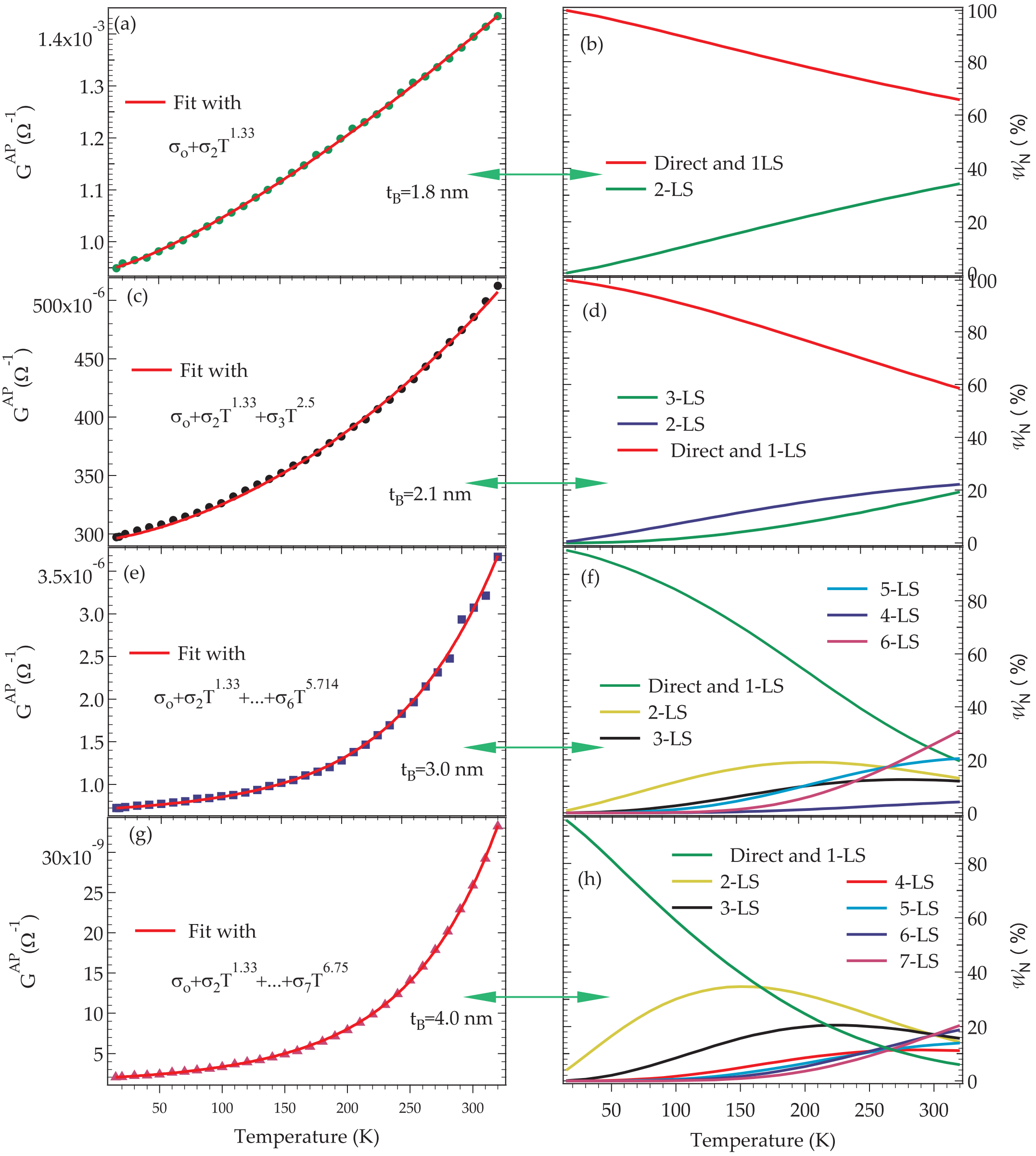

Figure 47: Temperature dependence of the tunnel conductance in an anti-parallel state and the relative contribution $W(N)$ of the different N-LS chains to the anti-parallel conductance for all four samples.

parameter σ_0 must be interpreted as an average value for direct and resonant tunneling.

MgO thickness	P_0	α $(K^{3/2})$
1.8 nm	0.7658 ± 0.0004	$5.71 \times 10^{-6} \pm 1.9 \times 10^{-7}$
2.1 nm	0.7681 ± 0.0004	$4.54 \times 10^{-6} \pm 1.8 \times 10^{-7}$
3.0 nm	0.7799 ± 0.0004	$6.85 \times 10^{-6} \pm 1.7 \times 10^{-7}$
4.0 nm	0.7796 ± 0.0004	$1.86 \times 10^{-5} \pm 2.0 \times 10^{-7}$

Table 8: Parameters for fitting $\Delta G(0,T)$ of a sample with t_B=1.8 to 4.0 nm simultaneously by using Eq. 37 and 38. The best simultaneous fits for all four samples were achieved for $C' = 4.0 \times 10^5 K^{-1} m^{-1}$.

The expression for ΔG(0,T) due to the activation of spin conserving inelastic hopping through chains of N localized state at zero bias is given by

$$\Delta G(0,T) = \sigma_0 \frac{CT}{sinCT} \times TMR_0 + \sum_{N \geq 1}^{N_{max}} \sigma_N^{N-2/(N+1)} T \times TMR(N,T) \tag{37}$$

and the TMR(N,T) assigned to a different variety of chains is given as:

$$TMR(N,T) = \frac{(1+P)^{2\beta_N} + (1-P)^{2\beta_N}}{2(1-P^{2\beta_N})} - 1 \tag{38}$$

with $\beta_N = 1/N + 1$ and an T-dependent effective spin polarization P=P$_0 \times (1 - \alpha T^{3/2})$ (α is the spin wave parameter related to the interfacial Curie temperature and P_0 is the effective spin polarization at $T = 0$K). The total temperature dependent TMR(T) is then given as the sum of TMR(N,T) weighted by their fractional contributation W_N:

$$TMR(T) = \sum_N W_N(T) \times TMR(N,T) \tag{39}$$

We have then fit the data of all four samples simultaneously by using Eq. 37 and 38, whereas the spin wave parameters α and the polarizations P$_0$ have been considered as free parameters, and the thermal smearing has been taken into account by $C = C' \times t_B$, keeping C' identical for all samples. The resulting parameters for t_B=1.8-4.0 nm are given in Tab. 8 and the resulting fits are shown in Fig. 48.

Although the fitting parameters in Table 8 can reproduce the temperature-dependent TMR data for all four samples quite well, the fit quality for ΔG(0,T) was not in all cases as satisfying as by fitting the data by the extended magnon-assisted tunneling model (see Sec. Fig. 43). Particularly, for t_B=4.0 nm the fit showed a rising trend of ΔG(0,T) for $T > 240$ K.

Second, the the extracted spin-wave parameters α were differ-

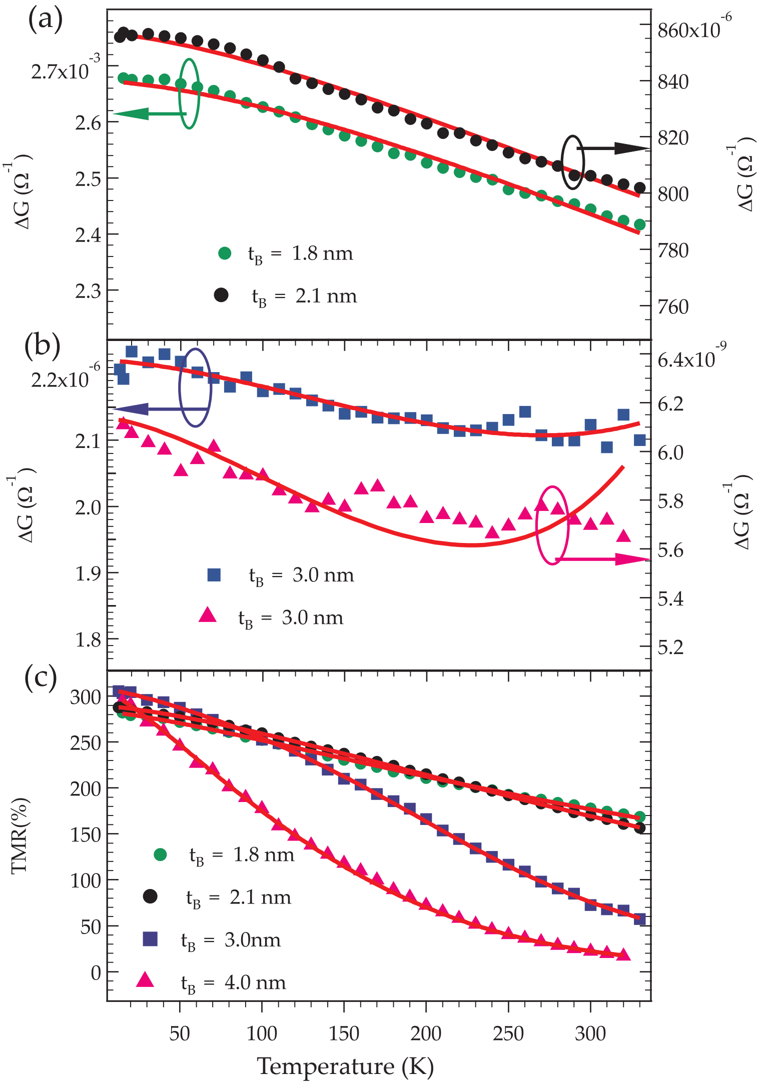

Figure 48: Typical temperature dependence of ΔG(0,T)[a, b] and TMR (c) for a sample with t_B =1.8 - 4.0 nm . The red lines represent fits using Eqs. 37 and 38.

ent for all samples. The latter would be in contradiction to our micro-structural investigations which showed the same quality of the electrode barrier interface for the different samples and, therefore, one would expect the same magnetic interface properties for the different samples. Therefore our data cannot be described conclusively by the model by Lu *et al.*, Accordingly, the existence of such a polarized conductance channel is not supported by our experiments. They have suggested a spin-polarized extension of the inelastic hopping conductance to explain the temperature dependence of the TMR in Co-Fe-B/ MgO / Co-Fe-B MTJs very similar to the MTJs investigated in this work despite the difference, that the TMR at low temperature and low bias voltage is 2 to 3 times larger (depending on the barrier thickness) for our junctions. The main motivation for the invention of spin-polarized hopping conductance was the experimental observation that ΔG(T) increased with increasing temperature for MTJs with 4nm (sample D in Lu *et al.*) thick MgO barrier (see Fig. 49).

This can not be explained by magnon-assisted tunneling in general, which always reduces ΔG (0, T) with increasing temperature. The difference between the samples is not clear at the moment. In particular, differences in the interface quality may be present because the maximal TMR amplitudes at low temperature are different in the two studies. To decide whether spin-polarized inelastic hopping is of general importance for MgO-based MTJs or not, further comparative studies by other groups are required.

5.5 Conclusion

We have investigated structural and transport properties of Co-Fe-B / MgO / Co-Fe-B junctions with a barrier thickness of up to 5nm. The HRTEM investigation on junction with barrier thickness t_B = 2.1nm and 4nm showed a good crystalline quality of the MgO barrier, and the electrode-barrier interface for both junctions in accordance with the similar low temperature TMR amplitudes, with the linear dependence of the dielectric breakdown voltage on the barrier thickness and the expected exponential increase of the RA product on the barrier thickness. We have demonstrated that direct spin-polarized and magnon-assisted tunneling can explain

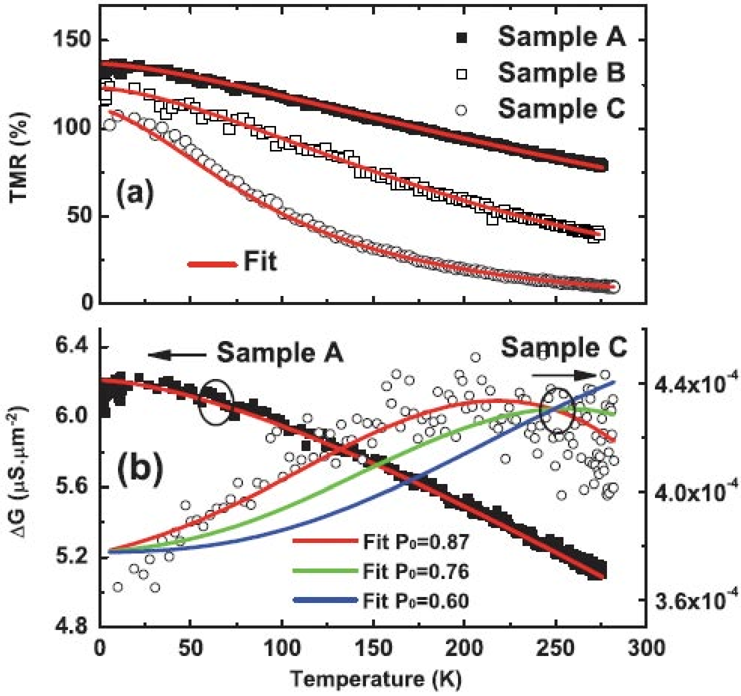

Figure 49: Typical temperature dependence of Δ G(0,T) and TMR(T)for a sample with t_B =1.8 and 4.0 nm (The terms sample A, B and C corresponding to barrier thickness of 2.5, 3 and 4nm in Lu *et al.*). In contrast to the work by Lu*et al.* all of our samples show a decreasing Δ G(V, T) with increasing temperature.

the bias voltage and temperature dependent transport properties for a barrier thickness of 1.8nm. For increasing barrier thicknesses this model has been successfully extended by an unpolarized current contribution.

This additional unpolarized conductance can well describe the very strong temperature dependence of the TMR for MTJs with 4nm thick MgO barrier, and we have not found any hints to spin-polarized inelastic tunneling as suggest by Lu et al.[100].

The contents of this chapter has been published in Physical Review B in 2010[101].

[100] Y. Lu et al., Phys. Rev. Lett. **102**, 176801 (2009)

[101] A. A. Khan et al., Phys. Rev. B **82**, 064416 (2010)

Table 9: Fitting parameters for samples with t_B=1.8-4.0 nm

parameter	sample with t_B=1.8 nm	sample with t_B=2.1 nm	sample with t_B=3.0 nm	sample with t_B=4.0 nm
σ_0	$9.426 \times 10^{-4} \pm 8 \times 10^{-7}$	$2.947 \times 10^{-4} \pm 4 \times 10^{-7}$	$7.15 \times 10^{-7} \pm 2 \times 10^{-9}$	$1.98 \times 10^{-9} \pm 3 \times 10^{-11}$
σ_2	$2.200 \times 10^{-7} \pm 7 \times 10^{-10}$	$5.7 \times 10^{-8} \pm 1 \times 10^{-9}$	$2.486 \times 10^{-10} \pm 6 \times 10^{-14}$	$2.210 \times 10^{-12} \pm 2 \times 10^{-15}$
σ_3	$\times \times \times$	$4.3 \times 10^{-11} \pm 2 \times 10^{-12}$	$1.23 \times 10^{-13} \pm 1 \times 10^{-17}$	$2.832 \times 10^{-15} \pm 5 \times 10^{-19}$
σ_4	$\times \times \times$	$\times \times \times$	$3.14 \times 10^{-16} \pm 6 \times 10^{-21}$	$3.538 \times 10^{-18} \pm 6 \times 10^{-22}$
σ_5	$\times \times \times$	$\times \times \times$	$2.899 \times 10^{-18} \pm 7 \times 10^{-24}$	$9.804 \times 10^{-21} \pm 3 \times 10^{-25}$
σ_6	$\times \times \times$	$\times \times \times$	$7.547 \times 10^{-22} \pm 2 \times 10^{-27}$	$3.034 \times 10^{-23} \pm 5 \times 10^{-28}$
σ_7	$\times \times \times$	$\times \times \times$	$\times \times \times$	$8.368 \times 10^{-26} \pm 6 \times 10^{-31}$

6

Characterization of Magnetic Tunnel Junction by IETS

6.1 Introduction

Inelastic electron tunneling spectroscopy[102] (IETS) has been used extensively in the past to probe vibrational modes in tunneling barrier materials, and more recently, to probe magnetic excitation in magnetic tunnel junctions. In ferromagnetic tunneling junctions, IETS allows the observation of spin-dependent excitations at the barrier-electrode interface. The relative magnetization of the electrodes alone will cause a change in the IET spectrum and provide the possibility of identifying specific contributions to the current which influences the TMR effect. Unfortunately, in bias voltage dependent electronic transport, the number of electrons tunneling inelastically is usually orders of magnitude smaller than the number utilizing elastic channels. Thus, it is difficult to detect the energy at which an inelastic channel opens from simple I-V or conductance-V curves because the contribution from these channels is too small against the much larger elastic background.

However, IETS involves measuring the derivatives of the tunneling current-voltage characteristics (dI/dV and dI^2/dV^2) in order to probe more sensitively the change of the conductance properties when excitation or absorption occurs as a part of the tunneling process. Specifically, this technique has a resolution that is limited only by the intrinsic temperature driven energy broadening of the spectra[103]. Additionally, the bias voltage range of the

[102] R. C. Jaklevic et al., Phys. Rev. Lett. **17**, 1139 (1966)

[103] S. K. Khanna et al., Science **220**, 1345 (1983)

spectra is only limited by the breakdown voltage of the junctions (typically in the range of a few volts as discussed in chapter 4).

IETS can in principle reveal all inelastic processes in which electrons take part in the tunneling process. In these junctions, it is especially possible to excite and identify phonons [104] of the barrier and the electrodes[105] as well as magnons in feromagnetic materials.[106] Another prominent feature in IETS spectra is the zero bias anomaly. In the dI/dV-V spectrum, a sharp dip at zero bias is usually found which results in large peaks in the IETS spectrum. In a nonmagnetic junction, this effect was first discovered by Wyatt[107] and has been correlated to single magnetic impurities[108].

A qualitative study of scattering at such impurities, however, has proven to be difficult[109]. In MTJs the zero-bias anomaly has always been found since IETS was first applied to MTJs by Moodera et al.[110] In addition, structures at bias voltages higher than 200 mV have recently been discussed.[111] They are of interest because they are presumably connected to the coherent tunneling process which is the base of the high TMR ratios in system with crystalline MgO barriers.

This chapter aims to identify intrinsic inelastic excitation in MgO based MTJs by means of the bias voltage dependence of the electronic transport. In the following we will discribe the experimental setup used to measure IETS spectra of Co-Fe-B/MgO/Co-Fe-B junctions (section). In section we will present the experimental results of IETS spectra of our samples with three different architectures (bottom pinned BAF-MTJ, top pinned TAF-MTJ and pesudo-spin-valve PSV) and compare the bias voltage dependence of the electronic transport properties of BAF-MTJ and TAF-MTJ . Finally, the IETS spectra of both sets of junctions are compared and correlated with their dielectric breakdown and possible origins for this correlation will be discussed. In the last section we provide conclusions.

6.2 *Experimental set-up*

Magnetic tunnel junctions with three different layer stacks are investigated. The samples are prepared using the same sputter system described earlier. Different the layer stacks are prepared, an

[104] J. Adler, Solid State Commun. **7**, 1635 (1969)

[105] T. T. Chen et al., Solid State Comm. **8**, 1965 (1970)

[106] D. C. Tsui et al., Phys. Rev. Lett. **27**, 1729 (1971)

[107] A. F. G. Wyatt, Phys. Rev. Lett. **13**, 401 (1964)

[108] J. A. Appelbaum et al., Phys. Rev. B **5**, 544 (1972)

[109] R. H. Wallis et al., J. Phys. C **7**, 1293 (1974); and S. Bermon et al., Phys. Rev. B **17**, 2110 (1978)

[110] J. S. Moodera et al., Phys. Rev. Lett. **80**, 2941 (1998)

[111] G.-X. Miao et al., J. Appl. Phys. **99**, 08T305 (2006); and M. Mizuguchi et al., J. Appl. Phys. **99**, 08T309 (2006)

overview of layer stack is given in table 10.

sample	Lower stack	t_B[nm]	Upper stack	T$_a$
BAF	Ta 5/Ru 30/Ta 10/Ru 5/ Mn-Ir 12/Co-Fe-B 2.5	1.8	Co-Fe-B 2.5/ Ta 5/Ru 20/	350^{o}C
TAF	Ta 5/Ru 30/Ta 10/ Ru 5/Co-Fe-B 2.5	1.8	Co-Fe-B 2.5/Ru 0.85/ CoFe 1.5/MnIr 12/Ru 20/	350^{o}C
PSV	Ta 5/Ru 30/Ta 10/ Ru 5/CoFeB 4	2.1	CoFeB 1.5/ Ta 5/Ru 30/	400^{o}C

Table 10: The different layer stacks and the corresponding annealing temperatures T$_a$. Numbers represent the layer thickness in nm.

The different annealing temperatures and barrier thicknesses were chosen to get highest TMR ratios at room temperature and good magnetic separation in the anti-parallel state of the two electrodes at low temperatures. IET spectra for the different samples are taken and evaluated. All measurements are done by a conventional two probe technique in a closed cycle helium cryostat (Oxford Cryo-drive 1.5) at 15 K. The bias voltage is always defined with respect to the lower electrode. Thus, negative bias results in electrons tunneling into the upper electrode. The differential conductance dI/dV of the MTJs was measured directly using a standard lock-in technique (STANDFORD SR830 DSP digital two channel Lock-In) with a modulation frequency of 6.85 kHz for parallel and anti-parallel alignments of the Co-Fe-B electrodes. From these data, the differential resistance dV/dI as well as the inelastic electron tunneling (dI^2/dV^2-V) spectra were calculated numerically. Before proceeding to the IETS spectra, a brief introduction to lock-in amplifier is given.

6.2.1 Lock-in amplifier

In its most basic form, a lockin amplifier is an instrument with dual capability[112]. It can recover signals in the presence of an overwhelming noise background or, alternatively, it can provide high-resolution measurements of clean signals over several orders of magnitude and frequency. A lock-in provides a DC output proportional to the AC signal at the input. The special rectifier, called phase sensitive detector (PSD), which performs this AC to DC conversion forms the heart of the instrument. It is significant in that it rectifies only the signal of interest while suppressing the ef-

[112] Stanford Research Systems, *DSP Lock-In Amplifier model SR830 Manual*

fects of noise in contrast to a traditional rectifier, which is typically found in a normal AC voltmeter making no distinction between signal and noise. To understand how a lock-in amplifier works, consider a signal V_{sig}sin (ω_{ref} t + ϕ_{sig}), modulated at a reference frequency ω_{ref}. The lock-in amplifier produces a signal V_L sin(ω_L t + ϕ_L) and a phase sensitive detector outputs the product of the two signals,

$$V_{out} = V_{sig} sin(\omega_{ref} t + \phi_{sig}) \times V_L sin(\omega_L t + \phi_L) \tag{40}$$

$$\begin{aligned} V_{out} &= \frac{V_{sig}V_L}{2} cos\left[(\omega_{ref} - \omega_L)t + (\phi_{sig} - \phi_{ref})\right] - \\ &\quad \frac{V_{sig}V_L}{2} cos\left[(\omega_{ref} + \omega_L)t + (\phi_{sig} + \phi_{ref})\right] \end{aligned} \tag{41}$$

Setting the lock in frequency equal to that of the reference frequency [ω_{ref}=ω_L=ω] and Prior to low pass filter the voltage V_{out} is:

$$V_{out} = \frac{V_{sig}V_L}{2}\Big(cos(\phi_{sig} - \phi_{ref}) - cos(2\omega t + \phi_{sig} + \phi_{ref})\Big) \tag{42}$$

After passing the V_{out} through a low pass filter the AC components are removed. In this case the filtered output voltage will be

$$V_{out} = \frac{V_{sig}V_L}{2} cos(\phi_{sig} - \phi_{ref}) \tag{43}$$

V_{out} is a DC voltage proportional to the signal. In the case of tunneling spectroscopy, the lock-in is used by adding a modulation voltage at a frequency f_m to the bias voltage,

$$V_T = V + V_m sin(\omega_m t) \tag{44}$$

where $\omega_m = \frac{f_m}{2\pi}$ and V_T is the total tunnel bias voltage. The current through the junction can be written as a Taylor expension[113],

$$\begin{aligned} I(V_T) &= I(V) + (\frac{dI}{dV})V_m sin(\omega_m t) + \\ &\quad (\frac{d^2I}{dV^2})V_m^2 sin^2(\omega_m t) + \cdots \end{aligned} \tag{45}$$

---

[113] M. L. Meade, *Lock-In Amplifiers: Principles and Applications* (IEEE electrical measurement series, 1983)

Therefore, the amplitude of the first harmonic is proportional to first derivative term, and second harmonic is proportional to second derivative term, which can be extracted using a phase sensitive detection technique.

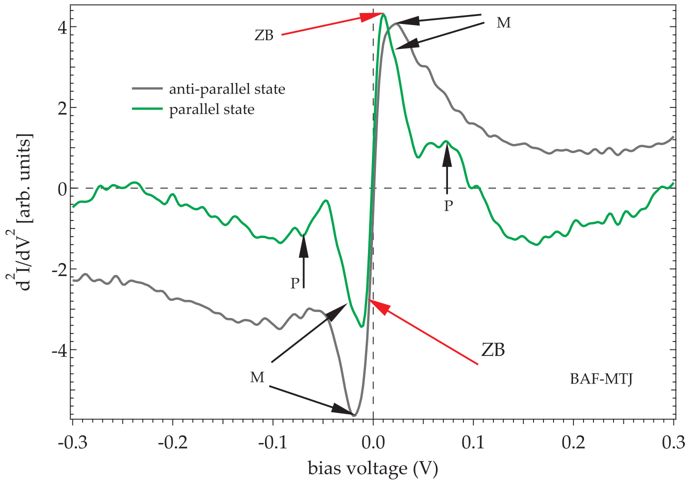

Figure 50: IETS spectra of BAF-MTJ in anti-parallel and parallel magnetic state.

We used an SRS-Model SR830 DSP lock-in amplifier for all of our measurements. The advantage of this DSP lock-in amplifier over a conventional amplifier is its ability to detect signals at a harmonic of the reference frequency. A constant voltage source provides the bias voltage V to which a modulation of 6.85 kHz and an amplitude of 2.83 mV (2mV effective voltage) is added. The SR830 multiplies this input signal with digital sine waves at the multiple of the reference. Only signals at the required harmonic (first harmonic in our case) will be detected. For a single channel lock-in, problems can arise if the phase of the input signal and the reference signal are off by $\frac{\pi}{2}$. However, the SR830 uses a dual-channel mode to get both the in-phase $sin(\omega_{ref}t)$ and out-of-phase $\cos(\omega_{ref}t)$ components of the input signal. These two components are added in quadrature to get the final dI/dV signal.

6.3 *Results*

IETS of bottom pinned (BAF-MTJ) junction

BAF-MTJ is a standard MTJ design with a pinned lower electrode. The sample displays a TMR ratio of over 246% at 15K. The spectra for the parallel and the anti-parallel magnetic state are shown in Figure 50. At low bias, around V = 0V the largest peaks are visible in both states (peaks are marked ZB in the Figure).

The peaks (M) at +24 mV and -22mV can be attributed to magnon excitation at the barrier-electrode interface, and their energy positions can be interpreted as energy with a maximum probability for magnon excitation[114]. In the parallel state, the broader peaks P are observed at 78 mV and -70 mV. The energy positions of these peaks can be recognized as the excitation of MgO phonons at the barrier/electrode interface[115]. In the anti-parallel state, the phonon peaks (P) are not clearly visible.

[114] X.-F. Han et al., Phys. Rev. B **63**, 224404 (2001)

[115] P. A. Thiry et al., Phys. Rev. B **29**, 4824 (1984)

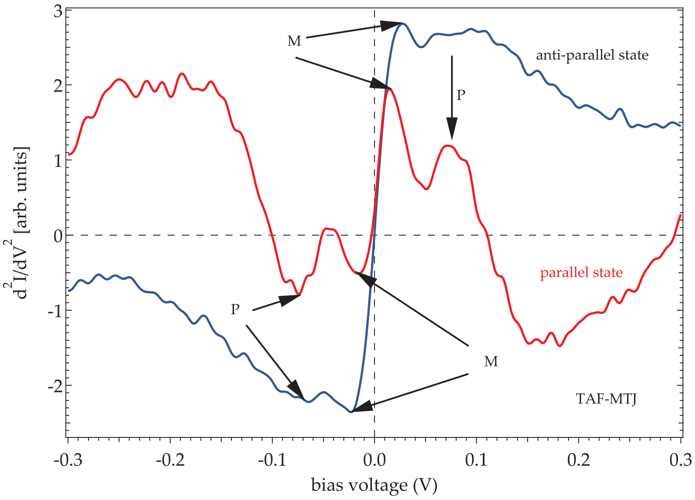

Figure 51: IETS spectra of TAF-MTJ in anti-parallel and parallel magnetic state

IETS of Top pinned (TAF-MTJ) junction

The TAF-MTJs display a TMR ratio of up to 216% at 15K. In these junctions a pinned artificial ferrimagnet forms the top electrode, while the lower electrode is free. IETS spectra in both magnetic states are shown in figure 51

The spectra look different from the spectra of BAF-MTJ. First of all, the general peak-height is much smaller in the parallel state compared to the anti-parallel state. Compared to BAF-MTJ, the asymmetry of the phonon peaks (P) is smaller and they can also be seen in the anti-parallel state.

IETS of Pseudo spin valve

A pseudo-spin valve junction with layer stack shown in Fig. 28 is investigated now. The IETS spectra in parallel and anti-parallel state are shown in Fig.52.

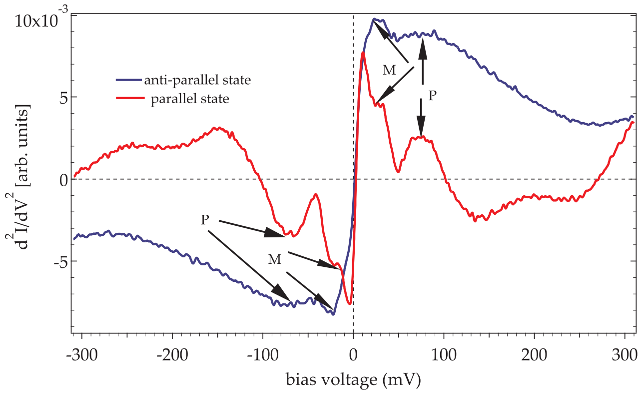

Figure 52: IETS spectra of the pseudo-spin valve junction in anti-parallel and parallel magnetic state. The figure was taken from our related publication, reported by Drewello(PRB, 79,174417 (2009))

It is evident from the figure 52 that in both states, the intensity of the peaks in the spectra lies between the intensities of BAF-MTJ and TAF-MTJ (if compared to the height of the rest of the respective spectra). The shoulders (M) at the first peaks are very pronounced in this sample. The rest of the spectrum, i.e. the phonon peaks (±71 mV) are very alike to those of TAF-MTJ. In the anti-parallel state, at higher biases, no further structures are found. More information on the the different features observed in IETS spectra of MgO based MTJs can be found in our related publication, reported by Drewello[116].

[116] V. Drewello et al., Phys. Rev. B **79**, 174417 (2009)

Asymmetry in electronic transport proporties:
A comparison between BAF-MTJ and TAF-MTJ

Both sets of samples showed very similar area resistance products and TMR amplitudes at RT. However, a distinctive asymmetric electronic contributions was found in both systems. Figure 53(a-b) shows the typical (dV/dI)-V spectra for BAF-MTJ and TAF-MTJ, respectively. Obviously, the asymmetry in the spectra marked by arrows is reversed when both systems are compared.

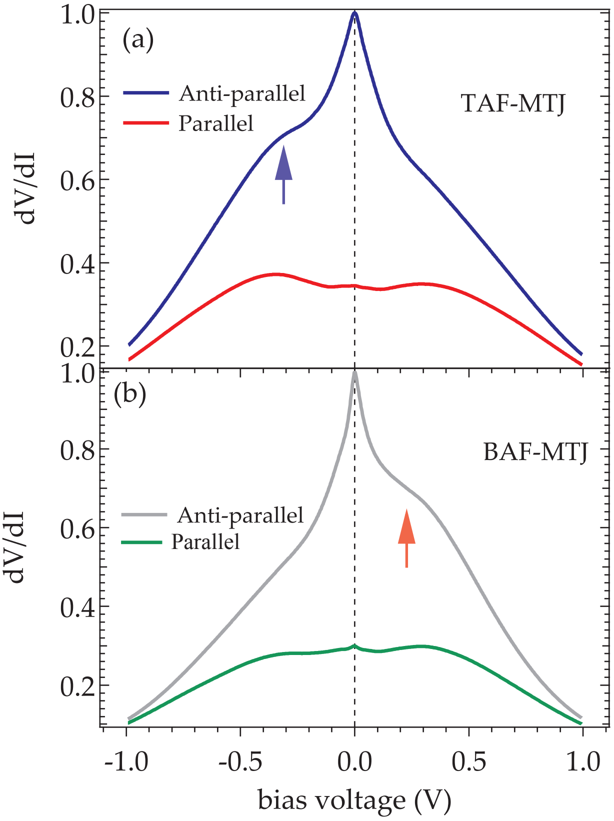

Figure 53: Differential resistance (dV/dI)-V spectra for parallel and anti-parallel magnetization states measured at 15K for (a) BAF-MTJ and (b) TAF-MTJ.

As discussed in chapter 4, BAF-MTJs and TAF-MTJs as well show in general larger breakdown voltages for positive than for negative bias voltage, i.e., the polarity dependence of the breakdown voltage does not change by changing the layer stack. This indicates that the asymmetries of the transport properties and of the breakdown voltage with respect to the bias voltage polarity have different origins. In the later case the observed higher breakdown voltage for positive bias result from the expected Oxygen distribution asymmetry induced during the deposition process (section 4.3). For the former case, the structural properties of the samples might be needed to explain the results. In the following, the differences between TAF-MTJ and BAF-MTJ shall be discussed with respect to the experimental results of the transport properties.

The first aspect concerns the different stacking of BAF-MTJs and TAF-MTJs, specifically, the location of the Mn-Ir layer in the samples. For BAF-MTJ (TAF-MTJ), the Mn is below the bottom electrode (above the top electrode). It is worth to mention that the diffusion of Mn from the anti-ferromagnetic layer to the electrode-barrier interface which is often observed in annealed MTJs (such a diffusion was, e.g., reported for Co-Fe-B/MgO/Co-Fe-B MTJs by Hayakawa et al[117].) might be needed to explain the asymmetry of the transport properties because of the obvious correlation of the asymmetry and the location of the Mn-Ir layer. Such an influence is reasonable because Mn oxides have different gap energies compared to MgO and, therefore, the formation of an asymmetric potential barrier leading to asymmetric transport characteristics can be expected.

As a second aspect regarding the structural properties of our MTJs, we like to refer to the work by Yuasa et al.[118] They also observed an asymmetry in the TMR bias voltage dependence measured at RT for epitaxial Fe/MgO/Fe junctions, and suggested that this results from asymmetric structural defects such as dislocations at the interface and lattice distortions in the Fe and MgO layers, identified by cross-sectional transmission electron microscopy (see Fig. 1 in Yuasa et al.). It can be expected that these types of structural defects are also present in our polycrystalline junctions. If these defects are responsible for the asymmetric transport properties, the change of the layer stack will need to change the asymmetry of the structural defects accordingly to explain the reversion of the asymmetry of the transport properties. This could be related to mechanical stress induced by the anti-

[117] J. Hayakawa et al., Appl. Phys. Lett. **89**, 232510 (2006)

[118] S. Yuasa et al., Nat. Mater **3**, 863 (2004)

ferromagnetic Mn-Ir layer below (BAF-MTJ) and above (TAF-MTJ) the barrier, respectively. However, thorough experimental investigations of the structural properties of the MTJs are required before a deeper understanding rather than a phenomenological description of the electrical measurements is possible.

Dielectric breakdown and IETS

Figure 54 shows the IETS spectra for BAF-MTJ and TAF-MTJ in parallel and anti-parallel state. The peaks (M) can be attributed to magnon excitation at the barrier - electrode interface. Usually the intensity of these peaks in the anti-parallel state is larger than in parallel state. This holds for BAF-MTJ as well as for TAF-MTJs indicating stronger magnon excitation in the anti-parallel state. However, there is a striking difference between the IETS

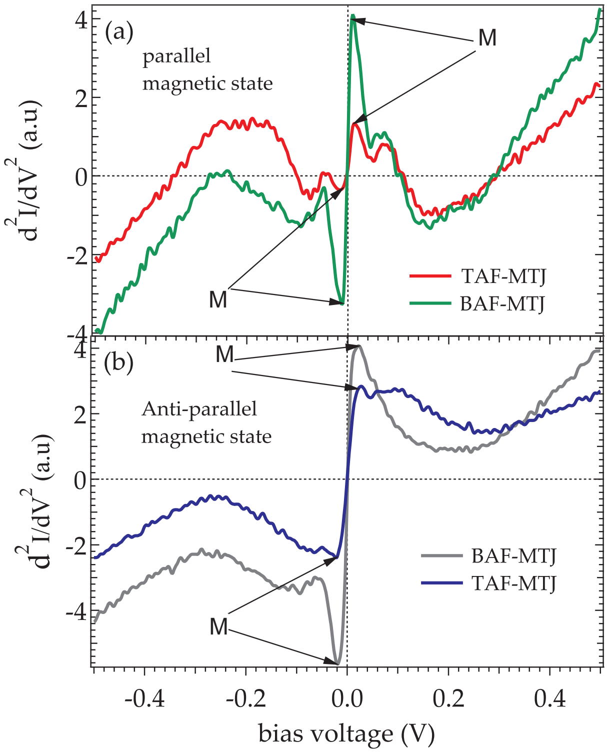

Figure 54: Comparison of IETS spectra of both systems in (a) in a parallel state (b) and in an anti-parallel state.

spectra of both systems: both in parallel and anti-parallel configuration the intensities of the magnon peaks are much weaker for TAF-MTJ than for BAF-MTJ, indicating that the magnon excitation is stronger in BAF-MTJ. This is further supported by the weaker temperature dependence of the TMR for TAF-MTJ as shown in Fig. 55.

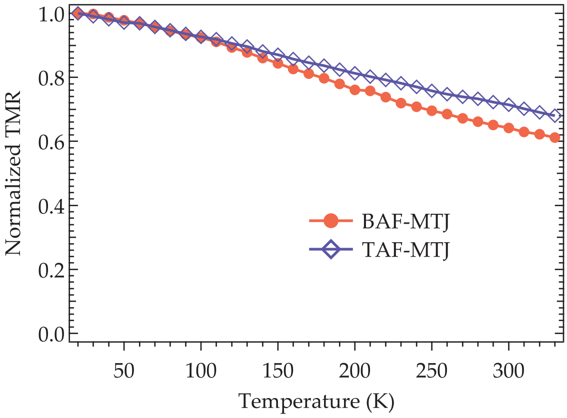

Figure 55: Typical normalized temperature dependence TMR for BAF-MTJ and TAF-MTJ measured with 10 mV bias voltage. The data are normalized to the TMR ratio at 15K.

The origin of the different strength of magnon excitation in the two systems is not known, but it is interesting that the this difference is correlated to the observation that the breakdown voltage is in general larger for TAF-MTJ compared to BAF-MTJ as discussed above. Therefore, it might be possible that the scattering events leading to breakdown are correlated with those exciting magnons which is certainly not included in the E-model or that both effects result from the same structural differences between BAF-MTJ and TAF-MTJ.

6.4 *Conclusion*

In conclusion, magnetic tunnel junctions were investigated by inelastic electron tunneling spectroscopy. For one set of samples, BAF-MTJ, the bottom electrode was magnetically hard (Mn-Ir/Co-Fe-B); in the other case, TAF-MTJ, the hard Co-Fe-B/Ru/Co-Fe/Mn-Ir electrode was on top of the barrier. In the third case , a pseudo-spin valve junction, a relatively thin ferromagnetic layer was deposited on top of barrier to ensure hard/soft switching of the magnetic electrodes. Several excitations were observed in both magnetic states of MTJs. The zero bias anomaly could be caused by magnetic impurities. A second contribution was found, which strongly differs for the parallel and the anti-parallel magnetic state. This is attributed to the excitation of magnons. The asymmetry of the differential resistance for BAF-MTJ was reversed compared to the results for TAF-MTJ suggesting that these properties have a different origin than the polarity dependence of the breakdown voltage. They might be correlated with the diffusion of Mn from the antiferromagnetic Mn-Ir layer to the barrier during vacuum annealing.

7

Summary and outlook

This thesis is devoted to the fundamental understanding of the dielectric reliability and spin dependent transport properties of MgO based MTJs with Co-Fe-B electrodes. These MTJs have gained tremendous importance in spintronic devices by showing large tunneling magnetoresistance (TMR) effects at room temperature.

In view of this, the emerging impact of these MTJS in various spintronics applications was obvious during the time of this thesis, as was the need for a thorough experimental and theoretical analysis of its dielectric stability and electronic transport, and their combined impact on its tunneling magnetoresistance. In Chapter 2 of this thesis few contemporary notions regarding spin dependent tunneling were portrayed and described coherent tunneling processes in MgO based MTJs. In Chapter 3, the main focus was on device fabrication methods and the various experimental analysis tools used.

Chapter 4 investigates the dielectric breakdown in MTJs. Due to very thin barrier thickness, large electric fields arise when voltage in the order of a few volts is applied. This may result in dielectric breakdown. Breakdown measurements under positive and negative bias were carried out for Mgo based MTJs. When comparing the results for the two bias directions, we found that for a positively biased top electrode, a larger breakdown voltage was generally observed. This points to an inhomogeneous defect distribution in the barrier. The observed higher breakdown voltage for positive bias result from the expected oxygen distribution asymmetry induced during the deposition process. By measuring the voltage at which breakdown occurs in a series of voltage ramp experiments, the results were analyzed in term of various expressions for the voltage dependent probabilities of breakdown, and estimation of the lifetime of junctions at lower voltages. In order to distinguish between the E and 1/E models, the extensions in many direction are required, e.g., measurement should be extended to a higher ramp rate than used in this study, and the statistical uncertainty should be decreased by the use of a large ensemble. Also, Frequency resolved electronic noise measurements are expected to be valuable and to be able to relate to the breakdown properties with the oxide and interface structure. On the other hand, TDDB measurement at lower bias provides an insight of the true model for the dielectric breakdown. Unfortunately, this type of measurement can take time in years, and is not possible in our case. The results of this chapter were published in the Journal of Applied physics[119].

In Chapter 5, we probed structural and transport properties of junctions and principally focussed on the temperature dependence of the TMR. The magnon-excitation model by Zhang[120], with integration of thermal smearing[121], can equally well account for the experimental data on temperature dependence of TMR for a 1.8 nm thick barrier. For increasing barrier thickness, this model has been successfully extended in this thesis by an unpolarized current contribution: depending on the barrier thickness, on the distribution of the electronic states localized in space and energy, the relative contribution of these additional channels to the total conductance of an MTJ may range from negligible to dominant. This mechanism may cause an additional reduction of TMR especially for higher barrier thickness. Moreover, it becomes clear, that magnon excitation is the second important inelastic non spin conserving which needs to be taken into account to explain the bias voltage and temperature dependence of TMR. Tailoring of both is crucial for getting less temperature dependence and, therefore, a higher TMR ratio at room temperature. In contrast to a recent study by Lu *et al.*[122] we did not find any hints regarding spin conserving inelastic current contributation in our data. Further comparitive studies are required to finally decide whether this inelastic spin conserving hopping is of general importance for MTJs

[119] A. A. Khan et al., J. Appl. Phys. **103**, 123705 (2008); and A. A. Khan et al., J. Appl. Phys. **105**, 083723 (2009)

[120] S. Zhang et al., Phys. Rev. Lett. **79**, 3744 (1997)

[121] V. Drewello et al., Phys. Rev. B **77**, 014440 (2008)

[122] Y. Lu et al., Phys. Rev. Lett. **102**, 176801 (2009)

or not. Our model was published in the journal Physical Review B.[123]

Finally, in chapter 6 we performed inelastic electron tunneling spectroscopy measurements on magnetic tunnel junction with three different architectures. In these measurements, different peaks were observed. Peaks in IETs spectra show the opening of transport channels due to specific inelastic excitations during the tunneling process. A magnon contribution was found, which strongly differs for the parallel and the anti-parallel magnetic state. These effects influence the tunnel current at elevated temperatures.

[123] A. A. Khan et al., Phys. Rev. B **82**, 064416 (2010)

References

A

Adler, J. Observation of the phonon spectra of MgO by inelastic electron tunneling in metal-insulator-metal junctions. Solid State Commun. **7**, 1635 (1969).

Anolick, E., and Nelson, G. Low field time dependent dielectric integrity. IEEE IRPS Proc. **17th Annual**, 8 (1979).

Appelbaum, J. A., and Shen, L. Y. L. Zero-bias-conductance-peak anomaly of Ta-i-Al tunnel junctions at 0.3 k and 90 kg. Phys. Rev. B **5**, 544 (1972).

B

Baibich, M. N., Broto, J. M., Fert, A., Dau, F. N. V., Petroff, F., Etienne, P., Creuzet, G., Friederich, A., and Chazelas, J. Giant magnetoresistance of (001)Fe/(001)Cr magnetic superlattices. Phys. Rev. Lett. **61**, 2472 (1988).

Berman, A. Time-zero dielectric reliability test by a ramp method. IEEE IRPS Proc. **19th Annual**, 204 (1981).

Bermon, S., Paraskevopoulos, D. E., and Tedrow, P. M. Ultrahigh magnetic field study of the kondo-type zero-bias conductance peak in magnetically doped metal-insulator-metal tunnel junctions. Phys. Rev. B **17**, 2110 (1978).

Binasch, G., Grünberg, P., Saurenbach, F., and Zinn, W. Enhanced magnetoresistance in layered magnetic structures with anti-ferromagnetic interlayer exchange. Phys. Rev. B **39**, 4828 (1989).

Bowen, M., Cros, V., Petroff, F., Fert, A., Boubeta, C. M., Costa-Krmer, J. L., Anguita, J. V., Cebollada, A., Briones, F., Teresa, J. M., Morelln, L., Ibarra, M. R., Gell, F., Peir, F., and Cornet, A. Large magnetoresistance in Fe/MgO/FeCo(001) epitaxial tunnel junctions on GaAs(001). Appl. Phys. Lett. **79**, 1655 (2001).

Brinkman, W. F., Dynes, R. C., and Rowell, J. M. Tunneling conductance of asymmetrical barriers. J. Appl. Phys. **41**, 1915 (1970).

Buchanan, D. A., DiMaria, D. J., Chang, C.-A., and Taur, Y. Defect generation in 3.5 nm silicon dioxide films. Appl. Phys. Lett. **65**, 1820 (1994).

Butler, W. H., Zhan, X.-G., and Schulthess, T. C. Spin-dependent tunneling conductance of Fe/MgO/Fe sandwiches. Phys. Rev. B **63**, 054416 (2001).

C

Chen, I. C., Holland, S., and Hu, C. Hole trapping and breakdown in thin SiO_2. IEEE Device Letter **3**, 164 (1986).

Chen, I. C., Holland, S. E., and Hu, C. Electrical breakdown in thin gate and tunneling oxides. IEEE Trans. Electron. Devices **32**, 413 (1985).

Chen, T. T., and Adler, J. G. Electron tunneling in clean Al-insulator-normal metal junction. Sol. Stat. Comm. **8**, 1965 (1970).

Choi, Y. S., Tsunekawa, K., Nagamine, Y., and Djayaprawira, D. Transmission electron microscopy study on the polycrystalline CoFeB/ MgO/ CoFeB based magnetic tunnel junction showing a high tunneling magnetoresistance, predicted in single crystal magnetic tunnel junction. J. Appl. Phys. **101**, 013907 (2007).

Crook, D. Method of determining reliability screens for thin gate oxide stressing. IEEE IRPS Proc. **17th Annual**, 1 (1979).

D

Degraeve, R., Ogier, J. L., Bellens, R., Roussel, P. J., Groeseneken, G., and H. E Maes IMEC, L. A new model for the field dependence of intrinsic and extrinsic time-dependent dielectric breakdown. IEEE Trans. Elec. Devices **45**, 472 (1998).

Degraeve, R., Roussel, P. H., Groeseneken, G., and Maes, H. E. A new analytic model for the description of the intrinsic oxide breakdown statistics of ultra-thin oxides. Microelectron. Reliab. **36**, 1639 (1996).

DiMaria, D. J., Cartier, E., and Buchanan, D. A. Anode hole injection and trapping in silicon dioxide. J. Appl. Phys. **80**, 304 (1996).

Djayaprawira, D. D., Tsunekawa, K., Nagai, M., Maehara, H., Yamagata, S., Watanabe, N., Yuasa, S., Suzuki, Y., and Ando, K. 230% room-temperature magnetoresistance in CoFeB/MgO/CoFeB magnetic tunnel junctions. Appl. Phys. Lett. **86**, 092502 (2005).

Drewello, V., Schmalhorst, J., Thomas, A., and Reiss, G. Evidence for strong magnon contribution to the TMR temperature dependence in MgO based tunnel junctions. Phys. Rev. B **77**, 014440 (2008).

Drewello, V., Schäfers, M., Schebaum, O., Khan, A. A., Münchenberger, J., Schmalhorst, J., Reiss, G., and Thomas, A. Inelastic electron tunneling spectra of MgO-based magnetic tunnel junctions with different electrode designs', Phys. Rev. B **79**, 174417 (2009).

E

Eilers, G., Ulrichs, H., Mnzenberg, M., Thomas, A., Thiel, K., and Seibt, M. Long-range order on the atomic scale induced at CoFeB/MgO interfaces. J. Appl. Phys. **105**, 073701 (2009).

Elshabini-Riad, A., and III, F. D. B. Thin film technology handbook', McGraw Hill, (1998).

F

Fert, A., and Campbell, I. A. Two-current conduction in nickel. Phys. Rev. Lett. **21**, 1190 (1968).

G

Ghibaudoa, G., Pananakakisa, G., Kiesa, R., Vincentb, E., and Papadasb, C. Accelerated dielectric breakdown and wear out standard testing methods and structures for reliability evaluation of thin oxides. Microelectron. Reliab. **39**, 597(1999).

Glazman, L., and Shekter, R. Inelastic tunneling across thin amorphous films. Sov. Phys. JETP **67**, 1276 (1988).

Glazman, L. I., and Matveev, K. A. hopping conductance through insulating barrier. Sov. Phys. JETP **67**, 163 (1988).

H

Han, X.-F., Andrew, Yu, C. C., Oogane, M., Murai, J., Daibou, T., and Miyazaki, T. Analyses of intrinsic magnetoelectric properties in spin-valve-type tunnel junctions with high magnetoresistance and low resistance. Phys. Rev. B **63**, 224404 (2001).

Hayakawa, J., Ikeda, S., Lee, Y. M., Matsukura, F., and Ohno, H. Effect of high annealing temperature on giant tunnel magnetoresistance ratio of CoFeB/MgO/CoFeB magnetic tunnel junctions. Appl. Phys. Lett. **89**, 232510 (2006).

Hertz, J. A., and Aoi, K. Spin-dependent tunnelling from transition-metal ferromagnets. Phys. Rev. B **8**, 3252 (1973).

I

Ikeda, S., Hayakawa, J., Ashizawa, Y., Lee, Y. M., Miura, K., Hasegawa, H., Tsunoda, M., Matsukura, F., and Ohno, H. Tunnel magnetoresistance of 604% at 300K by suppression of Ta diffusion in CoFeB/MgO/CoFeB pseudo-spin-valves annealed at high temperature. Appl. Phys. Lett. **93**, 082508 (2008).

J

Julliere, M. Tunneling between ferromagnetic films. Phys. Lett. **54A**, 225 (1975).

Jaklevic, R. C., and Lambe, J. Molecular Vibration Spectra by Electron Tunneling. Phys. Rev. Lett. **17**, 1139 (1966).

K

Khan, A. A., Schmalhorst, J., Reiss, G., Eilers, G., Mnzenberg, M., Schuhmann, H., and Seibt, M. Elastic and inelastic conductance in Co-Fe-B/MgO/Co-Fe-B magnetic tunnel junctions. Phys. Rev. B **82**, 064416 (2010).

Khan, A. A., Schmalhorst, J., Thomas, A., Drewello, V., and Reiss, G. Dielectric breakdown and inelastic electron tunneling spectroscopy of top and bottom pinned Co-Fe-B/MgO/Co-Fe-B magnetic tunnel junctions. J. Appl. Phys. **105**, 083723 (2009).

Khan, A. A., Schmalhorst, J., Thomas, A., Schebaum, O., and Reiss, G. Dielectric breakdown in Co-Fe-B/MgO/Co-Fe-B magnetic tunnel junction. J. Appl. Phys. **103**, 123705 (2008).

Khanna, S. K., and Lamnbe, J. Inelastic electron tunneling spectroscopy', Science 220, 1345 (1983).

Knoll, M., Brunig, D., and Fahrner, W. R. Comparative studies of tunnel injection and irradiation on metal oxide semiconductor structures. J. Appl. Phys. **53**, 6946 (1982).

L

Kimura, M., Koyama, H. Mechanism of time-dependent oxide breakdown in thin thermally grown SiO_2 films. J. Appl. Phys.**85**, 7671 (1999).

Lee, J., Chen, I., and Hu, C. Modeling and characterization of gate oxide. IEEE Trans. Electron. Devices **35**, 2268 (1988). 4.4

Larkin, A., and Matveev, K. Current-voltage characteristics of mesoscopic semiconductor contacts. Sov. Phys. JETP, **66**, 580 (1987).

Lu, Y., Tran, M., Jaffrs, H., Seneor, P., Deranlot, C., Petroff, F., George, J.-M., Lpine, B., Ababou, S., and Jzquel, G. Spin-polarized inelastic tunneling through insulating barriers', Phys. Rev. Lett. **102**, 176801(2009).

M

MacDonald, A. H., Jungwirth, T., and Kasner, M. Temperature dependence of itinerant electron junction magnetoresistance. Phys. Rev. Lett. **81**, 705 (1998).

Maissel, L. Handbook of Thin Film Technology. McGraw Hill, (1983).

Moodera, J. S., J. N., and van de Veerdonk, R. J. M. Interface magnetism and spin wave scattering in ferromagnet-insulator-ferromagnet tunnel junctions. Phys. Rev. Lett. **80**, 2941 (1998).

Martin, A., Sullivan, P., and Mathewson, A. Dielectric reliability measurement methods. Micro electron. Reliab. **38**, 37 (1998).

McPherson, J., Reddy, V., and le, H. Comparison of E and 1/E model for SiO_2 under long term low field test conditions. IEEE IEDM **98**, 171 (1998).

McPherson, J. W., Khamankar, R. B., and Shanware, A. Complementary model for intrinsic time-dependent dielectric breakdown in SiO_2 dielectrics. J. Appl. Phys. **88**, 5351 (2000).

McPherson, J. W., and Mogul, H. C. Underlying physics of the thermochemical E model in describing low-field time-dependent dielectric breakdown in SiO_2 thin films. J. Appl. Phys. **84**, 1513 (1998).

Meservey, R., and Tedrow, P. M. Spin-polarized electron tunneling. Phys. Rev. **238**, 173 (1994).

Meyerheim, H. L., Popescu, R., Kirschner, J., Jedrecy, N., Sauvage-Simkin, M., Heinrich, B., and Pinchaux, R. Geometrical and compositional structure at metal-oxide interfaces: MgO on Fe(001). Phys. Rev. Lett. **87**, 076102 (2001).

Miao, G. X., Chang, J. Y., van Veenhuizen, M. J., Thiel, K., Seibt, M., Eilers, G., Mnzenberg, M., and Moodera, J. S. Epitaxial growth of MgO and Fe/MgO/Fe magnetic tunnel junctions on (100)-Si by molecular beam epitaxy. Appl. Phys. Lett. **93**, 142511 (2008).

Miao, G.-X., Chetry, K. B., Gupta, A., Butler, W. H., Tsunekawa, K., Djayaprawira, D., , and Xiao, G. Inelastic tunneling spectroscopy of magnetic tunnel junctions based on Co-Fe-B/MgO/Co-Fe-B with Mg insertion layer. J. Appl. Phys. **99**, 08T305 (2006).

Mizuguchi, M., Hamada, Y., Matsumoto, R., Nishioka, S., Maehara, H., Tsunekawa, K., Djayaprawira, D. D., Watanabe, N., Nagahama, T., Fukushima, A., Kubota, H., Yuasa, S., Shiraishi, M., and Suzuki, Y. Tunneling spectroscopy of magnetic tunnel junctions: Comparison between Co-Fe-B/MgO/Co-Fe-B and Co-Fe-B/AlO/Co-Fe-B. J. Appl. Phys. **99**, 08T309 (2006).

Moodera, J. S., Kinder, L. R., Wong, T. M., and Meservey, R. Large magneto resistance at room temperature in feromagnetic thin films. Phys. Rev. Lett. **74**, 3273 (1995).

Moodera, J. S., Nowak, J., and van de Veerdonk, R. J. M. Interface magnetism and spin wave scattering in ferromagnet-insulator- ferromagnet tunnel junctions. Phys. Rev. Lett. **80**, 2941 (1998).

Mott, N. Electrons in transition metals. Adv. Phys., **13**, 325 (1964).

Mott, N., and Davis, E. Electronic processes in noncrystalline materials. Oxford Univ. Press, New York, 1979.

O

Oepts, W., Verhagen, H. J., de Jonge, W. J. M., and Coehoorn, R. Dielectric breakdown of ferromagnetic tunnel junctions. Appl. Phys. Lett. **73**, 2363 (1998).

Oepts, W., Verhagen, H. J., de Jonge, W. J. M., and Coehoorn, R. Analysis of breakdown in ferromagnetic tunnel junctions. J. Appl. Phys. **86**, 3863 (1999).

Oliver, B., He, Q., Tang, X., and Nowak, J. Dielectric breakdown in magnetic tunnel junctions having an ultra-thin barrier. J. Appl. Phys. **91**, 4348 (2002).

Osburn, C. M., and Ormond, D. W. Dielectric breakdown in silicon dioxide films on silicon. J. Electrochem. Soc. **119**, 591597 (1972).

Ohring, M. Reliability and Failure of Electronic Materials and Devices. Academic Press, (1998)

P

Panhorst, M. On-chip manipulation and positioning of biomolecules with magnetic beads. **PhD thesis**, Bielefeld university, (2005).

Parkin, S. S., Jiang, X., Kaiser, and Panchula. Magnetically engineered spintronic sensors and memory. Proc. IEEE **91**, 661 (2003).

Parkin, S. S. P., Kaiser, C., Panchula, A., Rice, P. M., Hughes,B, Samant, M., and Yang, H. Giant tunnelling magnetoresistance at room temperature with MgO(100) tunnel barriers. Nat. Mater. **3** 862 (2004).

R

Read, J. C., Mather, P. G., and Buhrman, R. A. X-ray photoemission study of CoFeB/MgO thin film bilayers. Appl. Phys. Lett. **90** 132503 (2007).

Rosenbaum, E., King, J. C., and Hu, C. Accelerated testing of SiO_2 reliability. IEEE Trans. Electron Devices **43** 70 (1996).

S

Schmalhorst, J., Brückl, H., Reiss, G., Gieres, G., and Wecker, J. Magnetotransport and microstructure of annealed magnetic tunnel junctions. J. Appl. Phys. **91** 6617 (2002).

Schmalhorst, J., Thomas, A., Reiss, G., Kou, X., and Arenholz, E. Influence of chemical and magnetic interface properties of Co-Fe-B/MgO/Co-Fe-B tunnel junctions on the annealing temperature dependence of the magnetoresistance. J. Appl. Phys. **102**, 053907 (2007).

Schmalhorst, J., and Reiss, G. Temperature and bias-voltage dependent transport in magnetic tunnel junctions with low energy Ar-ion irradiated barriers. Phys. Rev. B. **68**, 224437 (2003).

Schuegraf, K., and Hu, C. Reliability of thin oxide layer. Semiconductor Sci. Tech. **9**, 989 (1994).

Schuegraph, K. F., and Hu, C. Hole injection oxide breakdown model for very low voltage lifetime extrapolation. IEEE IRPS Proc. **31st Annual**, 7 (1993).

Seneor, P., Bernand-Mantel, A., and Petroff, F. Nanospintronics: when spintronics meets single electron physics. J. Phys.: Condens. Matter **19**, 165222 (2007).

Shang, C. H., Nowak, J., Jansen, R., and Moodera, J. S. Temperature dependence of magnetoresistance and surface magnetization in ferromagnetic tunnel junctions. Phys. Rev. B **58**, R2917 (1998).

Simmons, J. G. Generalized formula for the electric tunnel effect between similar electrodes separated by a thin insulating film. J. Appl. Phys. **34**, 1793 (1963).

Slonczewski, J. C. Current-driven excitation of magnetic multilayers. J. Magn. and Magn. Mater. **159**, L1 (1996).

Stearns, M. B. Simple explanation of tunneling spin-polarization of Fe, Co, Ni and its alloys. J. Magn. and Magn. Mater. **5**, 167 (1977).

Stratton, R. Volt-current characteristics for tunneling through insulating films. J. Phys. Chem. Solids **23**, 1177 (1962).

Suehle, J., and Chaparala, P. Low electric field breakdown of thin SiO_2 films under static and dynamic stress. IEEE Trans. Electron Devices **44**, 801 (1997).

Swagten, H. J. M. Spin tunneling in magnetic junctions. Elsevier, Oxford, UK, Vol. **17**, Chap. 1, (2007).

T

Thomas, A. Preparation and characterisation of magnetic single and double barrier junctions. **PhD thesis**, Bielefeld university, (2003).

Tsui, D. C., Dietz, R. E., and Walker, L. R. Multiple magnon excitation in nio by electron tunneling. Phys. Rev. Lett. **27**, 1729 (1971).

Tulapurkar, A. A., Suzuki, Y., Fukushima, A., Kubota, H., Maehara, H., Tsunekawa, K., Djayaprawira, D. D., Watanabe, N., and Yuasa, S. Spin-torque diode effect in magnetic tunnel junctions. Nature **438**, 339 (2005).

W

Wallis, R. H., and Wyatt, A. F. G. Exchange scattering in Ti-doped Al/Al-O/Ag tunnel junctions in magnetic field. J. Phys. C **7**, 1293 (1974).

Wei, H. X., Qin, Q. H., Ma, M., Sharif, R., and Han, X. F. magnetic tunnel junction with CoFeB as free and reference layers. J. Appl. Phys. **101**, 09B501 (2007).

Whited, R. C., Flaten, C. J., and Walker, W. C. Exciton thermoreflectance of MgO and CaO. Sol. St. Communications **13**, 1903 (1973).

Wolf, S. A., Awschalom, D. D., Buhrman, R. A., Daughton, J. M., von Molna, S., Roukes, M. L., Chtchelkanova, A. Y., and Treger, D. M. Spintronics: A spin-based electronics vision for the future. Science **294**, 1488 (2001).

Wyatt, A. F. G. Anomalous densities of states in normal tantalum and niobium. Phys. Rev. Lett. **13**, 401 (1964).

X

Xu, Y., Ephron, D., and Beasley, M. R. Directed inelastic hopping of electrons through metal-insulator-metal tunnel junctions. Phys. Rev. B **52**, 2843 (1995).

Y

Yassine, A., Nariman, H., and Olasupo, K. Field and temperature dependence of TDDB of ultra-thin gate oxide. IEEE Electron Device Lett. **20**, 390 (1999).

Yuasa, S., and Djayaprawira, D. D. Giant tunnel magnetoresistance in magnetic tunnel junctions with a crystalline MgO(001) barrier. J. Phys. D: Appl. Phys. **40**, R337 (2007).

Yuasa, S., Nagahama, T., Fukushima, A., Suzuki, Y., and Ando, K. MgO based MTJs. Nat. Mater **3**, 863 (2004).

Z

Zhang, S., Levy, P. M., Marley, A. C., and Parkin, S. S. P. Quenching of magnetoresistance by hot electrons in magnetic tunnel junctions. Phys. Rev. Lett. **79**, 3744 (1997).

Zutic, I., Fabian, J., and Sarma, S. D. Spintronics: Fundamentals and applications. Rev. Mod. Phys. **76**, 323 (2004).

Appendix A

The fraction F(t) of the junctions that have shown breakdown at a certain time t is related to the breakdown rate f(t) by

$$f(t) = \frac{dF(t)}{dt} = (1 - F(t))p(t) \tag{46}$$

where p(t) is the breakdown probability density[124]. In a voltage ramp experiment p(t)=p(V(t))= p(V), and equation 46 is written as:

$$f(t) = \frac{dF(t)}{dt} = (1 - F(t))p(V) \tag{47}$$

If p(t) reflects a monotonic increase of the breakdown probability density with increasing voltage V then we expact there is certain voltage V$_{max}$ at which breakdown rate is maximum, i.e. $\frac{df(t)}{dt}$= 0. Differentiating above Eq. 47 with respect to time t

$$\begin{aligned} \frac{df(t)}{dt} &= \frac{dp(V)}{dt}(1 - F(t)) + p(V)\frac{d}{dt}(1 - F(t)) \\ &= \frac{dp(V)}{dt}(1 - F(t)) - p(V)\frac{dF(t)}{dt} \\ &= \frac{dp(V)}{dt}(1 - F(t)) - [p(V)]^2 (1 - F(t)) \\ &= \left[\frac{dp(V)}{dt} - [p(V)]^2\right](1 - F(t)) \end{aligned} \tag{48}$$

from Eq.47
dF(t)/dt=(1-F(t))p(V)

Note that the f(t) peak occurs only when $\frac{df(t)}{dt}$=0 and V=V$_{max}$. Also the term (1-F(t)) represents the fraction of non-failed junctions. For the maximum breakdown rate Eq. 48 reduces to

$$\left[\frac{dp(V)}{dt} - [p(V)]^2\right]_{V=V_{max}} = 0 \tag{49}$$

[124] M. Ohring, *Reliability and Failure of Electronic Materials and Devices* (Academic Press, 1998); and W. Oepts et al., J. Appl. Phys. **86**, 3863 (1999)

Now from Eq.49 we can figure out the rate of maximum breakdown probability density in term of the ramp speed $\frac{dV}{dt}$ as:

$$\left(\frac{dp(V)}{dt}\right)_{V=V_{max}} = \left(\frac{dV}{dt}\frac{dp(V)}{dV}\right)_{V=V_{max}} = \left([p(V)]^2\right)_{V=V_{max}} \tag{50}$$

The breakdown probability density p(V) according to the E model and 1/E model is given by[125]

$$p(V) = Aexp\left(\frac{V}{B}\right) \tag{51}$$

and

$$p(V) = Cexp\left(\frac{-D}{V}\right) \tag{52}$$

If we use Eq. 50 together with the breakdown probability density of E and 1/E model expressed in Eq. 51 and 52 this leads to an expression for V_{max} as a function of the ramp speed. To derive the expression for V_{max} Eq. 51 can be written as: (after taking derivative and multiplying by ramp speed dV/dt)

$$\frac{dV}{dt}\frac{dp(V)}{dV} = \frac{dV}{dt}\frac{1}{B}p(V) \tag{53}$$

similarly for the 1/E model:

$$\frac{dV}{dt}\frac{dp(V)}{dV} = \frac{dV}{dt}\frac{D}{V^2}p(V) \tag{54}$$

At V= V_{max} the Eq. 53 and 54 can be analytically expressed as:

$$[p(V_{max})]^2 = \frac{dV}{dt}\frac{1}{B}p(V_{max}) \tag{55}$$

and

$$[p(V_{max})]^2 = \frac{dV}{dt}\frac{D}{V_{max}^2}p(V_{max}) \tag{56}$$

Now for the E-model the equation for maximal f(t) is written as:

$$V_{max} = Bln\left(\frac{dV}{dt}.\frac{1}{AB}\right) \tag{57}$$

and similarly foe 1/E model

$$V_{max} = D\left[ln\left(V_{max}^2\frac{C}{D}\right) - ln\left(\frac{dV}{dt}\right)\right]^{-1} \tag{58}$$

[125] W. Oepts et al., Appl. Phys. Lett. **73**, 2363 (1998)

Appendix B

Assuming that in the absence of an electric field the activation energy for bond breakage is ΔH_o^*, then in the presence of a field this required activation energy is reduced by[126]

$$\Delta H^* = \Delta H_o^* - p^*.E_{loc} \tag{59}$$

where p* is electric dipole moment and E$_{loc}$ is local field that a bond will experience when field is applied. In the presence of a field the dipole flipping will continue until the system comes in thermal equilibrium[127]. In the equilibrium state the number of dipoles in their respective states obey a Boltzman distributation. The rate of field enhanced thermal bond breakage can be described by a first order reaction rate.

$$\frac{dN}{dt} = -kN(t) \tag{60}$$

where N(t) is the week bond available for thermal breakage at time t and k is the reaction rate constant and is given by

$$k = \nu_o exp\left[-\frac{\Delta H_o^* - p^*.E_{loc}}{k_B T}\right] \tag{61}$$

The physical interpretation of the reaction rate constant (Eq. 61) is straightforward. ν_o is simply the number of times per second that a revelant bond can break while the exponential term is the Boltzmann probability that, on a given interaction bonds receive enough energy to activate breakage. Separating variables and intergrating Eq. 60 from t=0 to t=TF, one obtains:

$$TF = \frac{\frac{N(o)}{N(t=TF)}}{k} \tag{62}$$

[126] J. W. McPherson et al., J. Appl. Phys. **84**, 1513 (1998)

[127] J. W. McPherson et al., J. Appl. Phys. **88**, 5351 (2000)

The term in numerator of Eq. 62 represent the critical fraction fraction of the bonds needed to be broken to induced electric breakdown of dielectric. Using Eq. 61 the time to failure TF(breakdown probability) is written as:

$$TF = A_o exp\left[-\frac{\Delta H_o^* - p.E_{loc}}{k_B T}\right] = A_o exp\left(\frac{\Delta H_o^*}{k_B T}\right) exp\left(-\frac{p^*.E_{loc}}{k_B T}\right) \tag{63}$$

Since $p^*.E_{loc}=p^*(1+L\chi)E$ where E is applied field. The effective field acceleration parameter is given by

$$\gamma = \frac{p^*(1+L\chi)}{k_B T} \tag{64}$$

Using Eq. 64 the the breakdown probability density as a function of applied field Ecan be expressed as

$$TF = A_o exp\left(\frac{\Delta H_o^*}{k_B T}\right) exp\left(-\gamma E\right) \tag{65}$$

Appendix C:
Analysis of unpolarized conductance

The temperature dependence of the unpolarized conductance was analysed by the Glazman model[128]. The unpolarized conductance can be assumed to be dominated by hopping through localized states in the barrier. The first step of this approch is to fit the unpolarized conductace by a function of the form:

$$G_{UP}(0,T) = \sum_{N\geq 2}^{N_{max}} S_N T^{N-2/(N+1)} \tag{66}$$

where T is the temperature in K, N is the number of participating localized states, and S_N are prefactors depending on the density of localized states in the barrier. At higher temperature the distinctive power law temperature dependence for hopping favors chains with higher N. The unpolarized data can be fitted very well [see Fig. 56], if the term up to N= 6 were taken into account for a 4 nm thick barrier, whereas for t_B= 3.0 nm only terms up to N=5 are needed [Fig56(b)] to fit the data in the same temperature range. The thinner sample with t_B= 2.1 nm manifests very similar behavior and follows the trend that the entire fit of the data in the same temperature range takes place with lower order hopping channels as the thickness decreases, in agreement with the theory.

If N would be increased in comparison with the number given above, it was found that the parameters are strongly correlated and start to loose their physical meaning. The fitting parameters are summarized in Table 11

[128] L. I. Glazman et al., Sov. Phys. JETP **67**, 1276 (1988)

Figure 56: Unpolarized conductance as a function of temperature for sample with barrier thickness (a) 4.0 nm, (b) 3.0 nm and (c) 2.1 nm. The solid lines is the best fit to the data with the power exponents fixed to their theoretically predicted values.

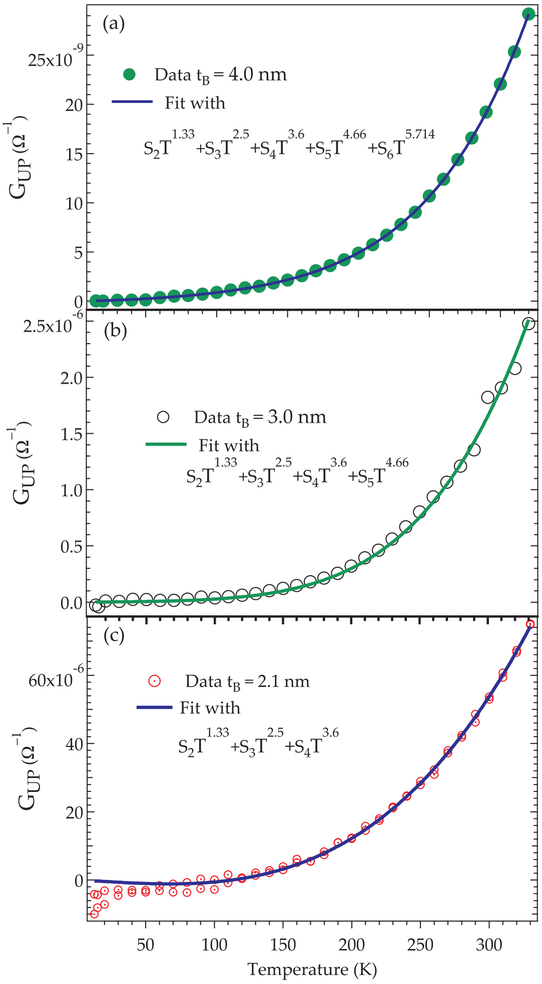

parameter	**MTJ with Barrier thickness**		
S_N	2.1 nm	3.0 nm	4.0 nm
S_1	$1.24 \pm 0.000 \times 10^{-11}$	$2.23 \pm 0.00 \times 10^{-11}$	$1.11 \pm 0.0 \times 10^{-12}$
S_2	$4.097 \pm 0.008 \times 10^{-12}$	$6.55 \pm 0.002 \times 10^{-14}$	$2.70 \pm 0.0024 \times 10^{-15}$
S_3	$1.737 \pm 1.07 \times 10^{-14}$	$1.31 \pm 0.001 \times 10^{-16}$	$4.49 \pm 0.0017 \times 10^{-18}$
S_4	XXXXXX	$4.0 \pm 0.0011 \times 10^{-18}$	$4.16 \pm 0.0007 \times 10^{-21}$
S_5	XXXXXX	XXXXXX	$7.37 \pm 0.019 \times 10^{-23}$

Table 11: Fitting parameters for samples with t_B=2.1-4.0 nm of unpolarized conductance

Appendix: Publications and manuscripts

Main author publications

Khan, A. A., Schmalhorst, J., Reiss, G., Eilers, G., Mnzenberg, M., Schuhmann, H., and Seibt, M. Elastic and inelastic conductance in Co-Fe-B/MgO/Co-Fe-B magnetic tunnel junctions. Phys. Rev. B **82**, 064416 (2010).

Khan, A. A., Schmalhorst, J., Thomas, A., Drewello, V., and Reiss, G. Dielectric breakdown and inelastic electron tunneling spectroscopy of top and bottom pinned Co-Fe-B/MgO/Co-Fe-B magnetic tunnel junctions. J. Appl. Phys. **105**, 083723 (2009).

Khan, A. A., Schmalhorst, J., Thomas, A., Schebaum, O., and Reiss, G. Dielectric breakdown in Co-Fe-B/MgO/Co-Fe-B magnetic tunnel junction. J. Appl. Phys. **103**, 123705 (2008).

Co-author publications

Drewello, V., Schäfers, M., Schebaum, O., Khan, A. A., Münchenberger, J., Schmalhorst, J., Reiss, G., and Thomas, A. Inelastic electron tunneling spectra of MgO-based magnetic tunnel junctions with different electrode designs', Phys. Rev. B **79**, 174417 (2009).

presentations

Khan, A. A., Schmalhorst, J., Thomas, A., and Reiss, G. Dielectric breakdown in Co-Fe-B/MgO/Co-Fe-B magnetic tunnel junction. (talk) **DPG Spring Meeting 2009**, Dresden.

Khan, A. A., Schmalhorst, J., Thomas, A., Rott, K., and Reiss, G. Dielectric breakdown and inelastic electron tunneling spectroscopy of top and bottom pinned Co-Fe-B/MgO/Co-Fe-B magnetic tunnel junctions. (poster) **DPG Spring Meeting 2009**, Dresden.

Khan, A. A., Schmalhorst, J., and Reiss, G. Temperature dependence of elastic and inelastic conductance in Co-Fe-B/MgO/Co-Fe-B magnetic tunnel junctions. (poster) **DPG Spring Meeting 2010**, Regensburg.

JOURNAL OF APPLIED PHYSICS **103**, 123705 (2008)

Dielectric breakdown in Co–Fe–B/MgO/Co–Fe–B magnetic tunnel junction

Ayaz Arif Khan,[a] J. Schmalhorst, A. Thomas, O. Schebaum, and G. Reiss
Thin Films and Nano Structures, Department of Physics, Bielefeld University, 33501 Bielefeld, Germany

(Received 20 February 2008; accepted 4 April 2008; published online 17 June 2008)

The time-dependent dielectric breakdown has been investigated in Co–Fe–B/MgO/Co–Fe–B junctions by voltage ramp experiments and focused on its dependence on the barrier thickness, junction area, polarity of the applied voltage, ramp speed, and annealing temperature. The results suggest that the breakdown voltage strongly depends both on the polarity of the applied voltage and the annealing temperature. Magnetic tunnel junctions (MTJs) with positive bias on the top electrode show higher breakdown voltage than MTJs with negative bias. We found that there is a significant decrease in the breakdown voltage when the annealing temperature is increased above 350 °C.

[DOI: 10.1063/1.2939571]

I. INTRODUCTION

Magnetic tunnel junctions (MTJs) have attracted considerable interest because of their potential in device applications such as magnetic memory cells or read heads in hard disk drives for density greater than 100 Gb/inch^2. The tunneling magnetoresistance (TMR) effect in magnetic tunnel junctions is a key to develop magnetoresistive random access memory (MRAM), magnetic read heads, and magnetic sensors.[1] In the conventional type of magnetic tunnel junction devices, which use amorphous Al_2O_3 as a tunnel barrier, one finds a magnetoresistive ratio of up to 70% at room temperature.[2] This low TMR ratio at room temperature is an obstacle to large capacity magnetoresistive random access memory. The recent development of magnetic tunnel junctions based on (001)-oriented MgO barriers and Co–Fe–B electrodes enabled TMR ratios of up to 361% at room temperature.[3] This high TMR is one key to realize a next-generation large-capacity MRAM and magnetic heads for ultrahigh-density recording. Before commercialization, MRAM faces several challenges, one of them related to the magnetic switching issue. Recently useful writing schemes (spin transfer switching)[4,5] have been demonstrated which enhance the scalability. Therefore most of the switching schemes require a high current that flows through the MTJ. Thus, dielectric breakdown of magnetic tunnel junctions has become one of the crucial factors for MTJ-based applications. Extensive tests involving a large number of devices are needed in order to determine their reliability.

In this article dielectric breakdown has been studied in Co–Fe–B/MgO/Co–Fe–B magnetic tunnel junctions. The key parameters for the oxide breakdown are barrier thickness, ramp speed, junction area, annealing temperature, and polarity of the applied voltage. The dielectric breakdown is characterized by a voltage ramp method. Among 400 breakdown measurements were conducted during this study. The results are discussed in the framework of the E-model,[6] which relates the breakdown to field-induced displacement of atomic bonds in the oxide barrier.

II. EXPERIMENT

The MTJ films were deposited in a dc magnetron sputtering system with a base pressure of 1×10^{-7} mbar on thermally oxidized Si(100) wafers. The MTJ stack sequence is as follows: Ta(5)/Ru(30)/Ta(10)/Ru(5)/MnIr(12)/Co–Fe–B(2.5)/MgO(t_B)/Co–Fe–B(2.5)/Ta(5)/Ru(20), where Co–Fe–B is a compound of $Co_{40}Fe_{40}B_{20}$. The numbers in parenthesis represent the nominal thickness of each layer in nanometers. The MgO barrier with a thickness (t_B) of 1.8 and 2.1 nm were deposited by rf magnetron sputtering in Ar atmosphere. In order to achieve the exchange bias of the MnIr/Co–Fe–B double layer, the MTJs were annealed up to 400 °C in the presence of a magnetic field (6.4 kOe) in a vacuum furnace with a pressure of 1×10^{-7} mbar. The optimum annealing temperature regarding TMR as well as breakdown voltage was 350 °C. The junctions with an area between 15×15 and 25×25 μm^2 were fabricated by laser lithography and ion-beam etching. The transport properties of the MTJs were measured using a two-probe method with dc bias voltage. Before measuring the dielectric breakdown, TMR and resistance of MTJ were measured at a bias voltage of 10 mV. The MTJs with a 1.8 and 2.1 nm thick MgO barrier showed TMR ratios of up to 174 and 155% at room temperature after optimum annealing, respectively. The corresponding resistance area (RA) product values of typically 96 kΩ μm^2 (1.8 nm) and 290 kΩ μm^2 (2.1 nm) were obtained depending on the barrier thickness. The breakdown experiment is conducted as a "voltage ramp" experiment. The ramping speed is varied between 5 and 20 mV/s.

III. RESULTS AND DISCUSSION

Two typical breakdown characteristics of MTJs that exhibited intrinsic breakdown are shown in Fig. 1. The intrinsic failure is then characterized by an abrupt decrease of resistance at the breaking point (see arrows in Fig. 1).[7] At breakdown, the voltage stays constant and the current shoots up. Afterward, no TMR effect was observed and, e.g., the resistance of MTJs with a junction size of 225 μm^2 was typically in the range of 75–10 Ω, corresponding to RA products of

---

[a] Electronic address: ayazarif@physik.uni-bielefeld.de.

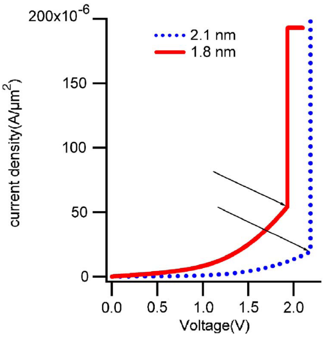

FIG. 1. (Color online) Typical $J-V$ curve for optimally annealed 400 μm^2 junctions in antiparallel magnetization state (AP) that break at 1.93 V (1.8 nm) and 2.18 V (2.1 nm), respectively. The ramp speed is 15 mV/s.

17–2.3 kΩ μm^2. This low resistance can be interpreted as a formation of microscopic shorts in the barrier at the moment of breakdown.[8]

Figure 2 shows the bias voltage dependence of the normalized TMR. As the bias voltage increases the TMR decreases. For the MTJ with 2.1 nm thick barrier the TMR drops to half at a bias voltage of 640 and 460 mV for positive and negative voltage, respectively. Similarly, the TMR for the 1.8 nm barrier drops to half at 755 and 532 mV for positive and negative bias voltages. The asymmetrical bias dependence can be interpreted as a result of an asymmetric tunneling barrier, e.g., because of asymmetric structural defect distribution such as the dislocations at the interfaces and lattice distortions.[9] From this we can expect an asymmetric breakdown behavior, which is indeed observed as discussed below.

The mean current density and voltage of MTJs at the breaking point are shown in Fig. 3 (the error bars represent the standard deviation for an ensemble of typically five nominally identical MTJs). It is found that the current density and breakdown voltage (V_B) of MTJs strongly depends on the polarity of the applied voltage. For positively biased top electrodes the current density and breakdown voltage is about 20 and 10% larger than for negatively biased top electrodes.

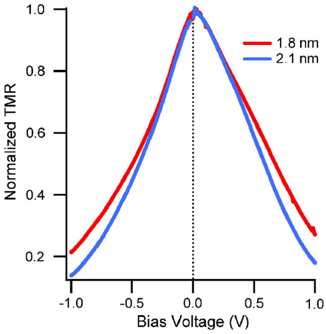

FIG. 2. (Color online) Bias voltage dependence of the TMR effect of MTJs at optimum annealed state.

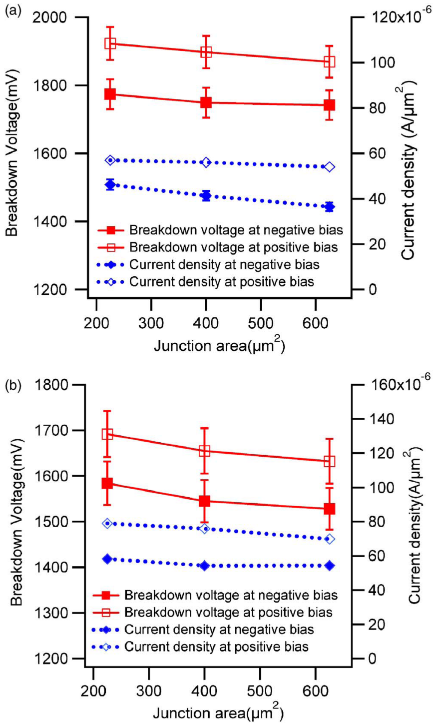

FIG. 3. (Color online) The current density (dotted line) and breakdown voltage (solid line) dependence on polarity of applied voltage for a barrier thickness of 1.8 nm: (a) antiparallel magnetization and (b) parallel magnetization state. The ramp speed is 15 mV/s.

In Fig. 4 the area and thickness dependence of the breakdown voltage is presented. It is seen that the breakdown voltage depends strongly on the thickness and weakly on the junction area in both parallel (P) and antiparallel (AP) magnetization state. An MTJ for negative bias in AP state with a 1.8 nm barrier and 225 μm^2 area typically breaks at 1.77 V. By increasing the barrier thickness by 0.3 nm, the breakdown voltage considerably increases to an average value of 1.93 V, i.e., by about 9.0%. Furthermore, the breakdown voltage of 1.8 nm thick barrier increases by 150 mV to 1.92 V when the polarity of the applied voltage is reversed, i.e., when the upper electrode is biased positively. The same trend is found for 2.1 nm thick barriers. Because of higher breakdown at positive bias, we speculate that the change of the junction reliability of MTJs under negative and positive bias is caused

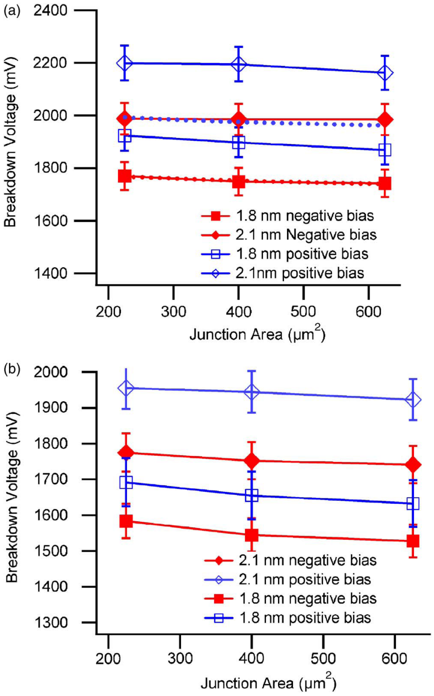

FIG. 4. (Color online) Breakdown voltage dependence on the area and barrier thickness for optimally annealed MTJs:(a) antiparallel magnetization and (b) parallel magnetization state. The ramp speed is 15 mV/s. The dotted lines represent the size dependence according to the E-model for 1.8 nm/2.1 nm thick barrier at negative bias in the antiparallel state (see Sec. IV).

by properties of the barrier, namely, an asymmetric defect density distribution at interface regions between the insulator and magnetic layer. By increasing the junction area from 225 to 625 μm^2 for a 1.8 nm thick barrier, the breakdown voltage decreases, e.g., by about 10% to an average of 1.74 V for antiparallel state and negative bias. In the parallel magnetization state the area and thickness dependence of breakdown voltage is shown in Fig. 4(b). It is evident that the breakdown voltage of 1.8 nm and 2.1 nm thick barriers in the parallel state decrease by about 210 and 250 mV, respectively, compared to the antiparallel magnetization state.

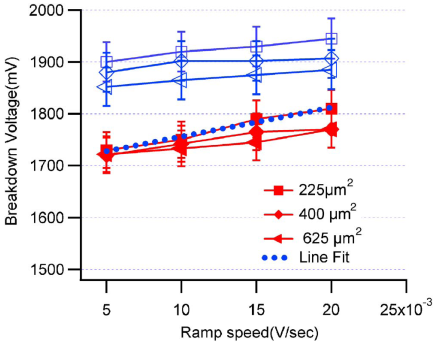

FIG. 5. (Color online) Breakdown voltage dependence on voltage ramp speed in AP state for optimally annealed MTJs with 1.8 nm thick barriers. Solid markers represent the breakdown when the upper electrode is negative biased, and hollow markers represent positive bias. Dotted lines represent the fit according to the E-model (see Sec. IV).

The current density at which the breakdown occurs is in general larger for the parallel than for the antiparallel state. Therefore, the breakdown voltage might not only be dominated by the voltage stress but even can be influenced by the current stress. However, it should be mentioned that the current density at the breakdown is about a factor of 3 smaller for 2.1 nm thick barriers than for 1.8 nm thick barriers, which favors that current density is not as important as bias voltage. We show below that all observed general trends are consistent with the E-model, which neglects the influence of the current.

The voltage ramp speed dependence of the breakdown voltage of MTJ is shown in Fig. 5. The devices which break intrinsically at V_B show a significant dependence on ramp speed, showing an increase of about 30–50 mV by increasing the voltage ramp speed from 5 to 20 mV/s. In Fig. 6 the annealing temperature dependence of the breakdown voltage is shown. The breakdown voltage increases with increasing annealing temperature and reaches a maximum value at an annealing temperature of 350 °C, and then decreases rapidly with further increase of annealing temperature. The largest value of V_B coincides with the largest TMR, again pointing to the barrier quality.

In Fig. 7 the dependence of V_B on the junction area is shown for different annealing temperatures. It is observed

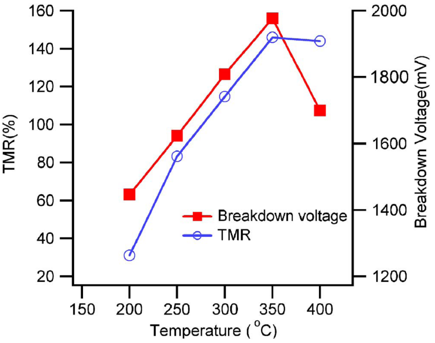

FIG. 6. (Color online) Variation of TMR and breakdown voltage (ramp speed is 15 mV/s) with annealing temperature. The junction area is 400 μm^2 and barrier thickness is 2.1 nm.

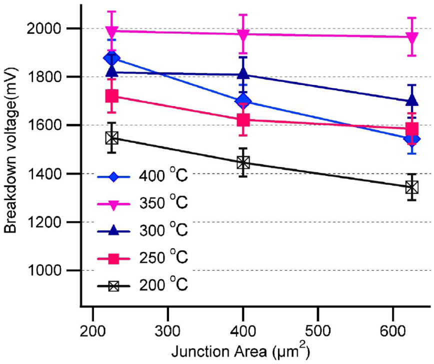

FIG. 7. (Color online) Breakdown voltage dependence on annealing temperature and junction size. The barrier thickness is 2.1 nm, the magnetization state is antiparallel (AP), and the ramp speed is 15 mV/s.

that the breakdown voltage depends strongly on the area for annealing temperature of 400 and 200 °C. For the optimum annealing temperature of 350 °C, the area dependence is smallest. A MTJ with a 2.1 nm thick barrier and 225 μm^2 area at 400 °C annealing temperature typically breaks at an average value of 1.87 V. By increasing the junction area to 625 μm^2 the breakdown voltage decreases by 18% to an average value of 1.54 V.

In our previous studies on Al–O-based junctions,[10,11] an increase of the breakdown voltage V_B with increasing annealing temperature was also found. It was attributed to a healing of barrier defects. However, a decrease of V_B above the optimal annealing temperature was only observed for junctions grown on Si wafers capped with native SiO_2 (Ref. 10) instead of 500 nm thick thermal SiO_2.[11] In this case a strong inhomogeneous temperature-induced crystallite growth was observed, resulting in high mechanical stress acting on the barrier and, accordingly, a reduced V_B. In our MgO-based MTJs investigated here we might also expect that the reduction of V_B above 350 °C is connected to additional mechanical stress as a result of recrystallization: it has been found that a recrystallization of the Co–Fe–B electrode at the MgO barrier takes place,[12,13] which results in "quasi-epitaxial" electrode-barrier interfaces, which is a prerequisite for coherent tunneling.

IV. INTRINSIC BREAKDOWN ANALYSIS

The experimental observations of the intrinsic breakdown can be interpreted using the E-model of dielectric breakdown.[6] This model was proposed previously for the breakdown of SiO_2 in metal-oxide-semiconductor (MOS) capacitors. As a dielectric is subjected to an electric field there is a net induced dipole moment which would cause a bond distortion. By the presence of an electric field, the effective activation energy E_A for a jump of an ion over a distance a in the direction of the field decreases, hence increasing the probability of a breakdown of the dielectric. The intrinsic breakdown is thus associated with the physical properties of the oxide and its microstructure. The junction area also affects the breakdown probability as the number of barrier defects which can act as "precursors" for the breakdown is proportional to the junction area. Oepts et al.[14] presented an analysis of Al–O-based MTJs which concluded that the observed intrinsic dielectric breakdown was well described with the use of the E-model.

In the following we will apply this model to our MgO-based MTJs: If $F(t)$ denotes the fraction of devices that break intrinsically after a time t, the breakdown probability density is defined as

$$p(t) = \frac{dF/dt}{1 - F}. \qquad (1)$$

For the E-model $p(t)$ is defined as

$$p(t) = A \exp\left(\frac{V(t)}{B}\right), \qquad (2)$$

where $V(t) = E(t) * t_B$ is the time-dependent voltage with $E(t)$ being the electric field and t_B is the barrier thickness. If no explicit time dependence is assumed for $p(t)$ (no wear out), A is proportional to the junction area and depends on the activation energy for dielectric breakdown. An external electric field $E(t)$ lowers the activation energy for the breakdown process, which is described by the field accelerating parameter $1/B$. For an experiment with constant ramp speed dV/dt, the intrinsic failure is given by

$$F(t) = 1 - \exp[-p(t)B(dV/dt)^{-1} + AB(dV/dt)^{-1}]. \qquad (3)$$

The maximum breakdown rate for a large number of devices is found at

$$V_{max} = B \ln\left(\frac{dV/dt}{AB}\right). \qquad (4)$$

We have generally observed a very small scattering of the breakdown voltage for our ensemble of nominally identical MTJs. Therefore, the mean breakdown voltage shown in all figures is nearly identical to V_{max}. For a large number of devices V_{max} varies linearly with $\ln(dV/dt)$ [see Eq. (4)] and hence, B can be extracted by fitting the ramp speed dependence of the breakdown voltages shown in Fig. 5 by Eq. (4).[8,15] For 1.8 and 2.1 nm thick barriers (225 μm^2 junction area), we have found B to be 0.028 ± 0.002 and 0.030 ± 0.01 V, respectively. For 1.8 nm thick barriers the fit is plotted as a dotted line in Fig. 5. The parameter A is also obtained by fitting the model according to Eq. (4) to the data. The values of A for 1.8 and 2.1 nm thick barriers (225 μm^2 junction area) in antiparallel magnetic state are 2.6×10^{-28} and 7.32×10^{-29} s^{-1}, respectively. The fitted results (the activation voltage B and the attempt frequency A) of a junction with 1.8 nm thick barrier in antiparallel magnetic state along with attempt frequency per unit area is summarized in Table I. The ratios of attempt frequency to the junction area are appear to be a constant, indicating that the fitted results are consistent with the E-model. A certain junction area dependence is even expected from Eq. (4). As shown as dotted lines in Fig. 4, these area dependencies are consistent with

TABLE I. E-model results for a 1.8 nm thick barrier in antiparallel state.

Polarity on top electrode	Junction area (μm^2)	Activation voltage B (mV)	Attempt frequency A (s^{-1})	Attempt frequency/Area $(\mu m^2\ s)^{-1}$
Negative	225	28.023 ± 2	2.60×10^{-28}	1.16×10^{-30}
Negative	400	27.874 ± 3	4.58×10^{-28}	1.15×10^{-30}
Negative	625	27.894 ± 3	7.18×10^{-28}	1.15×10^{-30}
Positive	225	28.889 ± 3	8.69×10^{-30}	3.86×10^{-32}
Positive	400	29.325 ± 2	1.48×10^{-29}	3.70×10^{-32}
Positive	625	28.832 ± 3	2.40×10^{-29}	3.84×10^{-32}

our experimental results. For time-independent breakdown probability density $p(t)$ the mean lifetime is then given by

$$\tau_{1/2} = \ln(2)/p(t), \tag{5}$$

where $\tau_{1/2}$ is the time when 50% of the devices have experienced breakdown. In Fig. 8 we show $\tau_{1/2}$ (years) as function of the applied bias voltage using the values of A and B for $t_B = 1.8$ and 2.1 nm, respectively. For a typical operating voltage of 300 mV, the lifetime for MTJs with 1.8 and 2.1 nm thick barriers can be estimated to 1.8×10^{16} and 1.4×10^{16} years, respectively.

V. SUMMARY

In summary, we have investigated the dielectric breakdown in MgO-based magnetic tunnel junctions with Co–Fe–B electrodes. Breakdown measurements under positive and negative bias were carried out for MTJs with 2.1 and 1.8 nm thick MgO barriers. When comparing the results for the two bias directions, we found a striking difference: for a positively biased top electrode a larger breakdown voltage was generally observed. This points to an inhomogeneous defect distribution in the barrier and is consistent with the observed asymmetric bias voltage dependence of the magnetoresistance. With respect to the annealing temperature, both the TMR as well as the breakdown voltage show a distinct maximum at 350 °C. Possible reasons for the decrease of breakdown voltage with further increasing annealing temperature were discussed. Finally, we were able to apply the E-model for dielectric breakdown consistently to the ramp speed as well as the junction area dependence of the breakdown voltage. In addition to these facts, the current density at the breakdown is considerably smaller for 2.1 nm compared to 1.8 nm thick barriers, and we can suggest that the breakdown process is dominated by the voltage stress rather than by current stress.

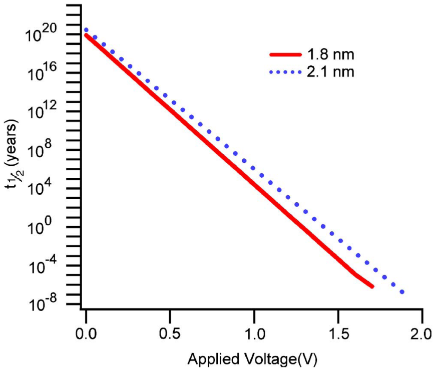

FIG. 8. (Color online) Estimated life time extracted from the E-model of dielectric breakdown for optimally annealed MTJs with 1.8 and 2.1 nm thick barriers.

ACKNOWLEDGMENTS

The authors gratefully acknowledge Volker Drewello, Ning-Ning Liu, Karsten Rott, Camelia Albon, and Daniel Ebke for assisting the sample preparation. Ayaz Arif Khan acknowledges financial support by the University of Azad Jammu & Kashmir Muzaffarabad. Financial support by the Deutsche Forschungsgemeinschaft (DFG) and the Bundesministerium für Bildung und Forschung (BMBF) is gratefully acknowledged.

[1] S. A. Wolf, D. D. Awschalom, R. A. Buhrman, J. M. Daughton, S. von Molnar, M. L. Roukes, A. Y. Chtchelkanova, and D. M. Treger, Science 294, 1488 (2001).
[2] D. Wang, C. Nordman, J. M. Doughton, Z. Qian, and J. Fink, IEEE Trans. Magn. 40, 2269 (2004).
[3] Y. M. Lee, J. Hayakawa, S. Ikeda, F. Matsukura, and H. Ohno, Appl. Phys. Lett. 89, 042506 (2006).
[4] J. C. Slonczewski, J. Magn. Magn. Mater. 159, L1 (1996).
[5] L. Berger, Phys. Rev. B 54, 9353 (1996).
[6] J. W. McPherson and H. C. Mogul, J. Appl. Phys. 84, 1513 (1998).
[7] B. Oliver, Q. He, X. Tang, and J. Nowak, J. Appl. Phys. 91, 4348 (2002).
[8] W. Oepts, H. J. Verhagen, W. J. M. de Jonge, and R. Coehoorn, Appl. Phys. Lett. 73, 2363 (1998).
[9] S. Yuasa, T. Nagahama, A. Fukushima, Y. Suzuki, and K. Ando, Nat. Mater. 3, 868 (2004).
[10] J. Schmalhorst, H. Brueckl, M. Justus, A. Thomas, G. Reiss, M. Vieth, G. Gieres, and J. Wecker, J. Appl. Phys. 89, 586 (2001).
[11] J. Schmalhorst, H. Brueckl, G. Reiss, G. Gieres, and J. Wecker, J. Appl. Phys. 91, 6617 (2002).
[12] J. Schmalhorst, A. Thomas, G. Reiss, X. Kou, and E. Arenholz, J. Appl. Phys. 102, 053907 (2007).
[13] Y. S. Choi, K. Tsunekawa, Y. Nagamine, and D. Djayaprawira, J. Appl. Phys. 101, 013907 (2007).
[14] W. Oepts, H. J. Verhagen, W. J. M. de Jonge, and R. Coehoorn, J. Appl. Phys. 86, 3863 (1999).
[15] B. Oliver, G. Tuttle, Q. He, X. Tang, and J. Nowak, J. Appl. Phys. 95, 1315 (2004).

JOURNAL OF APPLIED PHYSICS 105, 083723 (2009)

Dielectric breakdown and inelastic electron tunneling spectroscopy of top and bottom pinned Co–Fe–B/MgO/Co–Fe–B magnetic tunnel junctions

Ayaz Arif Khan,[a] J. Schmalhorst, A. Thomas, V. Drewello, and G. Reiss
Department of Physics, Thin Films and Physics of Nano Structures, Bielefeld University, P.O. Box 100131, 33501 Bielefeld, Germany

(Received 19 May 2008; accepted 10 March 2009; published online 30 April 2009)

The time dependent dielectric breakdown in Co–Fe–B/MgO/Co–Fe–B magnetic tunnel junctions was investigated by voltage ramp experiments. The measurements were done for two types of junctions: one set of junctions had exchange biased (pinned) bottom electrodes and one set had exchange biased (pinned) top electrodes with an additional artificial ferrimagnet. We found a significant polarity dependence in the dielectric breakdown: top as well as bottom pinned tunnel junctions showed higher breakdown voltage when the top electrode was biased positively compared to negative bias. In contrast to this the differential resistance $(dV/dI)-V$ spectra revealed an asymmetry for the top pinned junctions which was reversed in comparison to the bottom pinned system. This indicates that both asymmetries have different origins. Additionally the bottom pinned junctions showed in general slightly lower breakdown voltages and stronger magnon excitation in the inelastic electron tunneling $(d^2I/dV^2)-V$ spectra than the top pinned junctions. Possible reasons for these correlations are discussed. © 2009 American Institute of Physics.

[DOI: 10.1063/1.3116554]

I. INTRODUCTION

Magnetic random access memory (MRAM) is a promising candidate for universal memory in high-performance and mobile computing as it is faster and consumes less power than existing technologies.[1] To realize such a MRAM, it is strongly desired that magnetic tunnel junctions (MTJs), which essentially consist of two ferromagnetic electrodes separated by a thin insulating layer[2,3] and constitute the memory cells, show high reliability. Currently, MTJs with MgO barrier and Co–Fe–B electrodes[4] are the most promising candidates for high density MRAM, because they have very high tunneling magnetoresistance (TMR) ratios, probably because of a spin filtering effect originally predicted for fully epitaxial Fe/MgO/Fe junctions.[5,6] Especially, low resistive MgO based MTJs are interesting for application, because their magnetization state can be switched from antiparallel to parallel and vice versa by spin-polarized currents (spin torque effect[7]) without the help of an external magnetic field.

The intrinsic reliability of a MTJ under voltage stress can be characterized by its breakdown voltage U_{BD}. This is typically measured by applying a ramped voltage to the MTJ: when U_{BD} is reached the resistance of the MTJ is suddenly strongly reduced in an irreversible breakdown process. The majority of all MTJs show only one abrupt decrease in the junction resistance. This type of breakdown is likely to be caused by an intrinsic failure of the oxide barrier. As it was shown for Al–O based junctions before,[8] the resistance after breakdown is limited by the current limit of the power supply used for the voltage ramp experiment and the resistance of the leads.

In our previous study,[9] we investigated MTJs with MgO barrier and Co–Fe–B electrodes with respect to their dielectric stability. Their magnetically hard bottom electrode was pinned by an adjacent antiferromagnetic Mn–Ir layer because of the exchange-bias effect[10] (these junctions will be called BAF-MTJ in the following). The results were consistent with the E-model,[11] which neglects the influence of the electrical current and relates the breakdown to an electric field-induced displacement of atomic bonds in the oxide barrier. In this study, we investigated the bias polarity dependence of time dependent dielectric breakdown (TDDB) in Co–Fe–B/MgO/Co–Fe–B junctions whose bottom electrode was the "free" layer and top electrode was an artificial ferrimagnet, Co–Fe–B/Ru/Co–Fe, pinned by an antiferromagnetic Mn–Ir layer (this system will be called TAF-MTJ). The results will be compared to the BAF- MTJs. Furthermore, inelastic electron tunneling spectroscopy (IETS) was also applied to investigate the spin dependent tunneling process for both top and bottom pinned tunnel junctions.

II. EXPERIMENT

The MTJ stacks were deposited at room temperature (RT) by dc and radio frequency (rf) magnetron sputtering on thermally oxidized Si wafer. The layer stack of the bottom pinned BAF-MTJ system was $Si-SiO_2(50)/Ta(5)/Ru(30)/Ta(10)/Ru(5)/Mn-Ir(12)/Co-Fe-B(2.5)/MgO(t_B)/Co-Fe-B(2.5)/Ta(5)/Ru(20)$. The top pinned TAF-MTJs consist of $Si-SiO_2(50)/Ta(5)/Ru(30)/Ta(10)/Ru(5)/Co-Fe-B(2.5)/MgO(t_B)/CoFeB(2.5)/Ru(0.85)/Co-Fe(1.5)/MnIr(12)/Ta(5)/Ru(20)$, where the atomic composition of the sputter targets were $Co_{70}Fe_{30}$, $Mn_{83}Ir_{17}$, and $Co_{40}Fe_{40}B_{20}$, respectively. The numbers in parentheses represent the nominal thicknesses of each layer in nanometers. All metallic layers were deposited by dc magnetron sputtering at an Ar pressure of 1×10^{-3} mbar. The

---

[a] Electronic mail: ayazarif@physik.uni-bielefeld.de.

TABLE I. Summary of TMR ratios and area resistance product for BAF-MTJs and TAF-MTJs with 1.8 and 2.1 nm thick MgO barriers. All measurements were performed prior to the breakdown experiments at RT with 10 mV bias voltage.

Sample	t_B (nm)	RA (average) (kΩ μm^2)	TMR (average) (%)	TMR (maximum) (%)
BAF-MTJ	2.1	291.3 ± 2.1	149.4 ± 6.0	155.0
	1.8	96.8 ± 2.5	168.0 ± 3.0	174.0
TAF-MTJ	2.1	307.3 ± 4.8	155.4 ± 4.0	160.0
	1.8	106.3 ± 3.7	164.0 ± 2.7	168.4

MgO barrier of thickness t_B of 1.8 or 2.1 nm was deposited by rf magnetron sputtering at an Ar pressure of 2.4 $\times 10^{-2}$ mbar. In order to activate the exchange bias of the hard electrode, the MTJs were annealed at 350 °C in the presence of a magnetic field (6.5 kOe) in a vacuum furnace with a base pressure of 1×10^{-7} mbar. The junctions with an area between 15×15 and 25×25 μm^2 were patterned by laser lithography and ion beam etching. The transport properties of the MTJs were measured using a two-probe method with constant dc bias voltage for temperatures between 12 K and RT. The breakdown measurements were performed by voltage ramp experiments with a ramp speed of 15 mV/s at RT for parallel as well as antiparallel alignments of the magnetic electrodes. Prior to the dielectric breakdown, the TMR and resistance of each MTJ were measured at RT with a bias voltage of 10 mV. The MTJs showed TMR ratios of up to 174% at RT. The mean values and standard deviation of the area resistance product in the antiparallel state and the TMR as well as the maximum TMR ratios are summarized in Table I.

The typical TMR major loops of both types of MTJs are shown in Fig. 1. The hysteresis loops of the hard electrodes of BAF-MTJ and TAF-MTJ, respectively, are shifted in opposite directions because in TAF-MTJs the Co–Fe–B and Co–Fe layers are antiferromagnetically coupled via the Ru spacer in the investigated field range with a net magnetic moment of the artificial ferrimagnet aligned in parallel to the magnetization of the Co–Fe–B layer. The differential conductance dI/dV of the MTJs was measured directly at 12 K using a standard lock-in technique with a modulation amplitude of 1 mV for parallel and antiparallel alignments of the Co–Fe–B electrodes. From these data the differential resistance dV/dI as well as the inelastic electron tunneling d^2I/dV^2 spectra were calculated numerically. The polarity of the applied voltage was defined with respect to the bottom electrode, i.e., for positive bias voltage the electrons tunnel from the bottom into the top electrode.

III. RESULTS AND DISCUSSION

The intrinsic failure due to voltage stress-induced degradation of an insulator is characterized by an abrupt decrease in resistance at the breakdown voltage U_{BD},[12] e.g., this can be seen in Fig. 2. During breakdown a highly conducting path is created which shunts the current.[13]

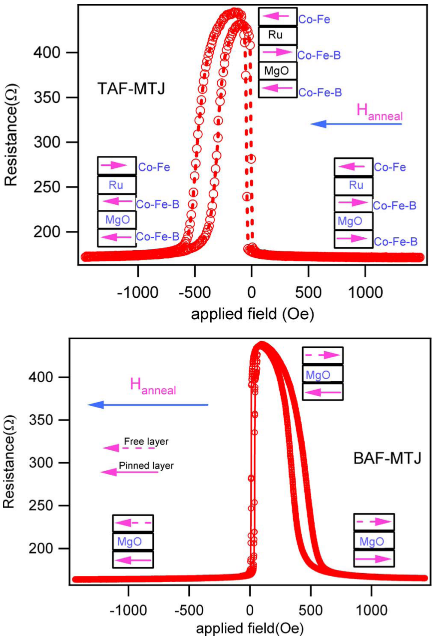

FIG. 1. (Color online) Typical major loops for BAF-MTJ and TAF-MTJ of 1.8 nm thick barrier. The orientation of the magnetic field H_{anneal} applied during vacuum annealing at 350 °C and the magnetization of free and pinned layers are indicated by arrows. The loops were taken at RT with 10 mV bias voltage. The junction area was 225 μm^2.

A comparison of dielectric breakdown for TAF-MTJs and BAF-MTJs with 1.8 nm thick barrier as a function of junction area and voltage polarity is shown in Fig. 3. It is

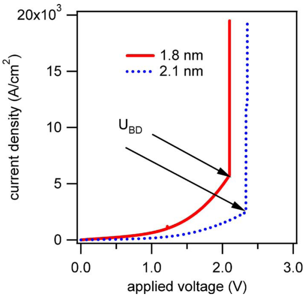

FIG. 2. (Color online) Variation of the current with applied voltage for TAF-MTJs with 1.8 and 2.1 nm thick MgO barriers, respectively. The MTJ with 1.8 nm (2.1 nm) thick barrier broke abruptly at $U_{BD} = +2.11$ V (+2.3 V). The magnetization state was antiparallel, and the junction area was 225 μm^2.

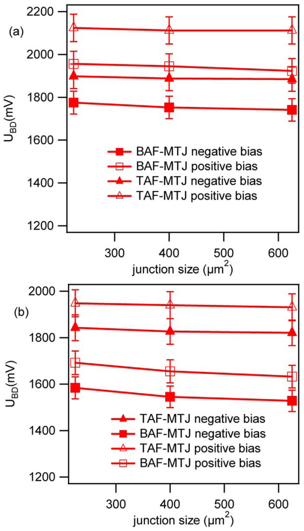

FIG. 3. (Color online) A comparison of the breakdown voltage dependence on the junction area and the polarity of the applied voltage of BAF-MTJ and TAF-MTJ for (a) antiparallel and (b) parallel magnetization alignments. Each point is an average over five individual measurements, and the error bars represent the standard deviation. The ramp speed was 15 mV/s.

evident that for the antiparallel (AP) as well as the parallel (P) magnetization states TAF-MTJs had higher breakdown voltages than BAF-MTJs. For example, a BAF-MTJ in antiparallel magnetization state with a junction area of 225 µm^2 under negative bias typically broke at $U_{BD} = -1.72$ V compared to $U_{BD} = -1.89$ V for a TAF-MTJ having the same junction area. Furthermore, all MTJs showed a higher breakdown voltage for positive than for negative bias; this trend holds for parallel as well as for antiparallel magnetization alignments. As summarized in Table II, the difference in breakdown voltage of BAF-MTJ and TAF-MTJ in parallel magnetization state is higher than in antiparallel state. These general trends found for MTJs with a 1.8 nm thick barrier are also valid for TAF-MTJs and BAF-MTJs with a barrier thickness of 2.1 nm. Because of the thicker barrier, the breakdown voltages are increased as expected from the E-model.[11] The latter can be seen, e.g., by comparing Figs. 4 and 3(a).

Differential resistance measurements and IETS have been applied to further investigate this puzzling behavior.

TABLE II. $(U_{BD})^{\text{TAF-MTJ}} - (U_{BD})^{\text{BAF-MTJ}}$ in antiparallel and parallel states with voltage bias polarities for 1.8 nm thick barrier.

Polarity	Parallel state (mV)	Antiparallel state (mV)
Negative bias	260–292	123–143
Positive bias	270–299	168–189

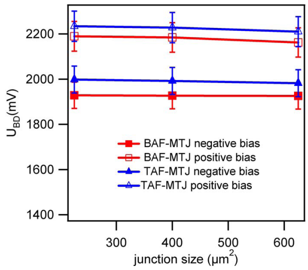

FIG. 4. (Color online) The breakdown voltage dependence on the junction area and voltage polarity for TAF-MTJ and BAF-MTJ with 2.1 nm thick barrier. Each point is an average of five individual measurements, and the error bars represent the standard deviation. The data were taken in the antiparallel magnetization state.

Figure 5 shows the typical (dV/dI)−V spectra for BAF-MTJ and TAF-MTJ, respectively. Obviously, the asymmetry in the spectra marked by arrows is reversed when both systems are compared. As discussed above, BAF-MTJs and TAF-MTJs as well show in general larger breakdown voltages for positive than for negative bias voltage, i.e., the polarity dependence of the breakdown voltage does not change by chang-

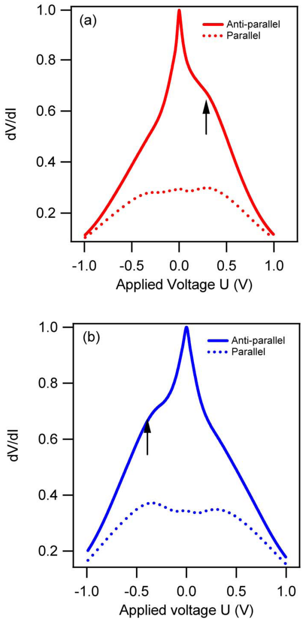

FIG. 5. (Color online) Differential resistance dV/dI−V spectra for parallel and antiparallel magnetization states measured at 12.5 K for (a) BAF-MTJ and (b) TAF-MTJ. The barrier thickness was 1.8 nm.

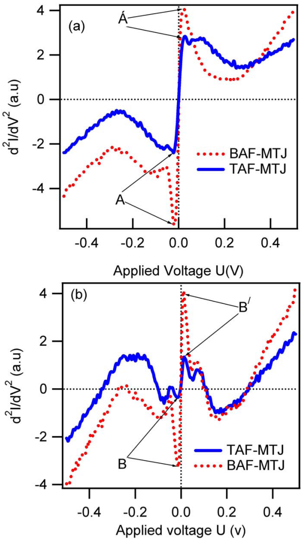

FIG. 6. (Color online) (a) Inelastic electron tunneling (d^{2}I/dV^2)−V spectra for BAF-MTJ and TAF-MTJ with 1.8 nm thick barrier in antiparallel magnetic state. (b) Inelastic electron tunneling (d^{2}I/dV^2)−V spectra for both systems in parallel magnetic states. The measurements were taken at 12.5 K, and the junction size was 225 μm^2.

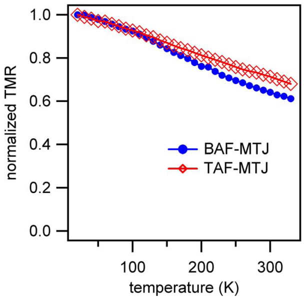

FIG. 7. (Color online) Typical normalized temperature dependence TMR for BAF-MTJ and TAF-MTJ measured with 10 mV bias voltage. The data are normalized to the TMR ratio at 20 K (BAF-MTJ: 244% and TAF-MTJ: 216%).

ing the layer stack. This indicates that the asymmetries of the transport properties and of the breakdown voltage with respect to the bias voltage polarity have different origins.

Before possible origins for this different behavior are discussed, the results of the inelastic tunneling spectroscopy shall be presented. Figure 6 shows the (d^{2}I/dV^2)−V spectra for BAF-MTJ and TAF-MTJ in parallel and antiparallel states. The peaks around zero bias (A, A′, B, and B′) can be attributed to magnon excitation at the barrier-electrode interface and their energy positions can be interpreted as energy with maximum probability for magnon excitation.[14] Usually the intensity of these peaks in the antiparallel state is larger than in parallel state; this holds for BAF-MTJ as well as for TAF-MTJ, indicating stronger magnon excitation in the antiparallel state. However, there is a striking difference between the IETS spectra of both systems: both in parallel and antiparallel configurations, the intensities of the magnon peaks are much weaker for TAF-MTJ than for BAF- MTJ, indicating that the magnon excitation is stronger in BAF-MTJ. This is further supported by the weaker temperature dependence of the TMR for TAF-MTJ, as shown in Fig. 7. More information on the TMR temperature dependence of our MgO based MTJs can be found in Ref. 15. With respect to the generally higher breakdown voltages for TAF-MTJs, we like to emphasize the correlation with the generally weaker magnon excitation for this junction type, whether the scattering events leading to magnon excitation do directly influence the breakdown process (which is certainly not included in the E-model) or whether both effects resulting from the same structural differences between BAF-MTJ and TAF-MTJ require further systematic studies of both breakdown and inelastic transport properties.

In the following, the structural properties of the samples, especially differences between TAF-MTJ and BAF-MTJ, shall be discussed with respect to the experimental results of the breakdown and transport properties.

The first aspect results from a symmetry breaking because of the deposition process itself: the MgO barrier is directly deposited on top of the lower Co–Fe–B electrode by rf sputtering from a MgO target. Therefore, the surface of the lower ferromagnetic electrode can be oxidized by oxygen originating from the target.[16,17] In contrast the interfacial Co–Fe–B at the upper barrier-electrode interface cannot be oxidized in this way. Accordingly, different oxygen concentrations are expected for both interfaces. As mentioned above, the dielectric breakdown is believed to be initialized by a field-induced break of an atomic bond in the oxide. As discussed by McPherson and Mogul[11] in detail for thin SiO$_2$ films, oxygen vacancies are thought to dominate the breakdown process as precursors for the initial bond breakage. Because it is not possible to determine the atomic arrangement of cobalt, iron, boron, magnesium, and oxygen atoms on an atomic level in our junctions, it is difficult to identify the precursors for the breakdown. However, taking the discussion on SiO$_2$ into account an influence of a small oxygen distribution asymmetry in the barrier region on the breakdown process is very reasonable. Because this oxygen distribution asymmetry must be expected for both TAF-MTJ and BAF-MTJ, it is reasonable that the, in general, observed higher breakdown voltages for positive bias compared to negative bias result from the expected oxygen distribution asymmetry.

The second aspect concerns the different stackings of BAF-MTJs and TAF-MTJs, more precisely the location of the Mn–Ir layer in the samples. A diffusion of Mn from the antiferromagnetic layer to the electrode-barrier interface is often observed in the annealed MTJs (e.g., reported for Co–Fe–B/MgO/Co–Fe–B MTJs by Hayakawa et al.[18]). For

BAF-MTJ (TAF-MTJ), the Mn is below the bottom electrode (above the top electrode). Because the bias polarity asymmetry of the breakdown process does not change for TAF-MTJ compared to BAF-MTJ, it is not likely that Mn diffusion is the origin of the bias polarity asymmetry of U_{BD}. On the other hand, the Mn diffusion to the barrier might be needed to explain the asymmetry of the transport properties because of the obvious correlation of this asymmetry and the location of the Mn–Ir layer. Such an influence is reasonable because Mn oxides have different gap energies compared to MgO and, therefore, the formation of an asymmetric potential barrier leading to asymmetric transport characteristics can be expected.

As a third aspect regarding the structural properties of our MTJs, we like to refer to the work by Yuasa et al.[19] They also observed an asymmetry in the TMR bias voltage dependence measured at RT (see Fig. 3 in Ref. 19) for epitaxial Fe/MgO/Fe junctions and suggested that this results from asymmetric structural defects such as dislocations at the interface and lattice distortions in the Fe and MgO layers, which was identified by cross-sectional transmission electron microscopy (see Fig. 1 in Ref. 18). It can be expected that this kind of structural defects are also present in our polycrystalline junctions. Because of the current lack of further experimental investigations on the structural properties of our junctions, e.g., by high resolution transmission electron microscopy, we can only speculate if such defects show an asymmetry with respect to the upper and the lower barrier-electrode interface and if such an asymmetry reverses if we compare BAF-MTJ with TAF-MTJ. However, from the experimentally found asymmetries of the transport and the dielectric breakdown properties and their dependencies on the stack sequence, it becomes clear that the details of the microstructure of our junctions responsible for the breakdown and the transport properties of our junctions must have according symmetry properties.

IV. CONCLUSION

The dielectric breakdown of Co–Fe–B/MgO/Co–Fe–B MTJs showing a TMR of up to 174% at RT was investigated. For one set of samples, BAF-MTJ, the bottom electrode was magnetically hard (Mn–Ir/Co–Fe–B); in the other case, TAF-MTJ, the hard Co–Fe–B/Ru/Co–Fe/Mn–Ir electrode was on top of the barrier. In general, larger breakdown voltages were observed, when the electrons tunnel from the bottom into the top electrode and when the magnetic electrodes were aligned antiparallel. The correlation to an expected asymmetric oxygen distribution induced during the deposition process was discussed. In contrast to this observation, the asymmetry of the differential resistance for BAF-MTJ was reversed compared to the results for TAF-MTJ suggesting that these properties have a different origin than the polarity dependence of the breakdown voltage. They might be correlated with the diffusion of Mn from the antiferromagnetic Mn–Ir layer to the barrier during vacuum annealing. However, because of the lack of highly resolving investigations of the structural properties, other aspects such as an asymmetry of interfacial defects (e.g., dislocations and lattice distortions) might be important for the understanding of our results. This also holds for a further interesting correlation between transport and breakdown properties. Namely, the breakdown voltage for a certain bias voltage polarity and magnetic alignment of the electrode was generally smaller for BAF-MTJ compared with TAF-MTJ, which was correlated with a stronger magnon excitation for the bottom pinned BAF-MTJs although both sets of samples showed very similar area resistance products and TMR amplitudes at RT.

ACKNOWLEDGMENTS

The authors gratefully acknowledge Volker Höink, Ning-Ning Liu, Karsten Rott, Camelia Albon, and Daniel Ebke for assisting the sample preparation. Financial support by the Deutsche Forschungsgemeinschaft (DFG) and the Bundesministerium für Bildung und Forschung (BMBF) is gratefully acknowledged. Ayaz Arif acknowledges financial support of the University of Azad Jammu and Kashmir Muzaffarabad.

[1] J. Akerman, Science 308, 508 (2005).
[2] J. S. Moodera, L. R. Kinder, T. M. Wong, and R. Meservey, Phys. Rev. Lett. 74, 3273 (1995).
[3] T. Miyazaki and N. Tezuka, J. Magn. Magn. Mater. 139, L231 (1995).
[4] D. D. Djayaprawira, K. Tsunekawa, M. Nagai, H. Maehara, S. Yamagata, S. Yuasa, Y. Suzuki, K. Ando, and N. Watanabe, Appl. Phys. Lett. 86, 092502 (2005).
[5] W. H. Butler, X.-G. Zhang, T. C. Schulthess, and J. M. MacLaren, Phys. Rev. B 63, 054416 (2001).
[6] J. Mathon and A. Umersky, Phys. Rev. B 63, 220403 (2001).
[7] G. D. Fuchs, J. A. Katine, S. I. Kiselev, D. Mauri, K. S. Wooley, D. C. Ralph, and R. A. Buhrman, Phys. Rev. Lett. 96, 186603 (2006).
[8] J. Schmalhorst, H. Bruekl, M. Justus, A. Thomas, and G. Reiss, J. Appl. Phys. 89, 586 (2001).
[9] A. A. Khan, J. Schmalhorst, A. Thomas, O. Schebaum, and G. Reiss, J. Appl. Phys. 103, 123705 (2008).
[10] W. H. Meiklejohn and C. P. Bean, Phys. Rev. 105, 904 (1957).
[11] J. W. McPherson and H. C. Mogul, J. Appl. Phys. 84, 1513 (1998).
[12] B. Oliver, Q. He, X. Tang, and J. Nowak, J. Appl. Phys. 91, 4348 (2002).
[13] W. Oepts, H. J. Verhagen, W. J. M. de Jonge, and R. Coehoorn, Appl. Phys. Lett. 73, 2363 (1998).
[14] X.-F. Han, A. C. C. Yu, M. Oogane, J. Murai, T. Daibou, and T. Miyazaki, Phys. Rev. B 63, 224404 (2001).
[15] V. Drewello, J. Schmalhorst, A. Thomas, and G. Reiss, Phys. Rev. B 77, 014440 (2008).
[16] J. Schmalhorst, A. Thomas, X. Kou, G. Reiss, and E. Arenholz, J. Appl. Phys. 102, 053907 (2007).
[17] J. C. Read, P. G. Mather, and R. A. Buhrman, Appl. Phys. Lett. 90, 132503 (2007).
[18] J. Hayakawa, S. Ikeda, Y. M. Lee, F. Matsukura, and H. Ohno, Appl. Phys. Lett. 89, 232510 (2006).
[19] S. Yuasa, T. Nagahama, A. Fukushima, Y. Suzuki, and K. Ando, Nature Mater. 3, 868 (2004).

PHYSICAL REVIEW B 82, 064416 (2010)

Elastic and inelastic conductance in Co-Fe-B/MgO/Co-Fe-B magnetic tunnel junctions

Ayaz Arif Khan, J. Schmalhorst,* and G. Reiss
Thin Films and Physics of Nanostructures, Department of Physics, Bielefeld University, P.O. Box 100131, 33501 Bielefeld, Germany

G. Eilers and M. Münzenberg
I. Physikalisches Institut, Georg-August-Universität Göttingen, Friedrich-Hund-Platz 1, 37077 Göttingen, Germany

H. Schuhmann and M. Seibt
IV. Physikalisches Institut, Georg-August-Universität Göttingen, Friedrich-Hund-Platz 1, 37077 Göttingen, Germany
(Received 8 April 2010; revised manuscript received 8 June 2010; published 13 August 2010)

A systematic analysis of the bias voltage and temperature dependence of the tunneling magnetoresistance (TMR) in Co-Fe-B/MgO/Co-Fe-B magnetic tunnel junctions with barrier thickness t_B between 1.8 and 4.0 nm has been performed. The resistance measured at low temperature in the parallel state shows the expected exponential increase with increasing barrier thickness. The low-temperature TMR amplitude of about 300% is quite similar for all MgO thicknesses. This is in accordance with microstructural investigations by transmission electron microscopy, which do not give hints to a reduction in the barrier quality with increasing MgO thickness. Both the junction resistance and TMR decrease with increasing temperature and bias voltage. In general, the decrease is much stronger for thicker barriers, e.g., a decrease in the TMR by a factor of 13.4 from 293% at 15 K to 21.9% at 300 K was observed for $t_B = 4.0$ nm compared to a reduction by only a factor of 1.6 for $t_B = 1.8$ nm. This behavior can be described self-consistently for all barrier thicknesses within a model that extends the magnon-assisted tunneling model by adding an inelastic, unpolarized tunneling contribution. Furthermore we discuss our results in the framework of a recent model by Lu et al. [Phys. Rev. Lett. 102, 176801 (2009)] claiming that polarized hopping conductance becomes important for larger MgO thickness.

DOI: 10.1103/PhysRevB.82.064416 PACS number(s): 85.30.Mn

I. INTRODUCTION

The tunnel magnetoresistance (TMR) effect in magnetic tunnel junctions (MTJs) has been the subject of intensive research in both fundamental and applied physics. Investigating the TMR effect is very important for developing magnetic random access memory, magnetic sensors, and novel programmable logic devices.[1] This stimulated tremendous activity in the experimental and theoretical investigation of electronic, magnetic, and transport properties of MTJs. The TMR effect in MTJs has been known from the experiment of Julliere for almost 35 years.[2] Basing on the pioneering work by Parkin et al.,[3] Yuasa et al.,[4] and Djayaprawira et al.[5] nowadays well-oriented (001) MgO-based MTJs show a TMR ratio of more than 1000% at low temperature and 600% at room temperature (RT),[6,7] which accords with theoretical predictions basing on coherent tunneling.[8,9] In this type of junction the as-deposited Co-Fe-B electrodes are amorphous. They recrystallize[10,11] during a postannealing process using the MgO as a template for forming a (001) out-of-plane-oriented quasiepitaxial structure, which is crucial for coherent tunneling processes. It is well know that the diffusion of boron out of Co-Fe-B is necessary for proper crystallization of the electrode.[12,13] It has been reported in literature that B diffusion in MgO during postannealing process forms an intermediate MgB_xO_y oxide, where the B has an oxidation state close to B^{3+}.[13–15] Localized electronic states in the barrier may arise from these ionized boron species or even from oxygen vacancies.[16]

In addition to direct spin-polarized tunneling through the oxide, localized state (LS) in the barrier can lead to new current channels such as resonant tunneling or inelastic hopping via chains of localized states.[17–19] Depending on the barrier thickness, on the distribution of the electronic states localized in space and energy and on the temperature and bias voltage the relative contribution of these additional channels to the total conductance of an MTJ may range from negligible to dominant. With respect to the TMR amplitude it is of special importance, whether new current channels are spin conserving or not.

In this paper, we present a systematic study of the area resistance (RA) product and the TMR in Co-Fe-B/MgO/Co-Fe-B MTJs showing a maximal TMR of about 300% as a function of temperature and bias voltage. We show that in addition to direct spin-polarized and magnon-assisted tunneling dominating the transport for a barrier thickness of 1.8 nm the relative contribution of inelastic, unpolarized hopping becomes much more important with increasing barrier thickness. Our results will also be compared to results recently published by Lu et al.[14] on Co-Fe-B/MgO/Co-Fe-B MTJs showing a maximal TMR of 136%.

II. EXPERIMENT

The MTJ stacks were prepared in a magnetron sputtering system with a base pressure of 1×10^{-7} mbar. The layer stack is Ta(5)/Ru(30)/Ta(10)/Ru(10)/Mn-Ir(12)/Co-Fe-B(2.5)/MgO(t_B)/Co-Fe-B(2.5)/Ta(5)/Ru(20) on top of thermally oxidized (50 nm) silicon (100) wafers, where the target compositions of Mn-Ir and Co-Fe-B were $Mn_{83}Ir_{17}$ and $Co_{40}Fe_{40}B_{20}$, respectively. The numbers in parenthesis represent the nominal thickness of each layer in nanometer. All metallic layers were deposited by dc magnetron sputtering at

1098-0121/2010/82(6)/064416(8)

TABLE I. Typical RA_P and RA_{AP} products in the parallel and antiparallel magnetization state and the corresponding TMR measured with a bias voltage of 5 mV at 15 K and 300 K, respectively.

t_B (nm)	RA_P @ 15 K	RA_{AP} @ 15 K	TMR @ 15 K (%)	RA_P @ 300 K	RA_{AP} @ 300K	TMR @ 300K (%)
1.8	110 kΩ μm^2	421 kΩ μm^2	283	105 kΩ μm^2	291 kΩ μm^2	177
2.1	346 kΩ μm^2	1.34 MΩ μm^2	287	312 kΩ μm^2	843 kΩ μm^2	170
3.0	77.2 MΩ μm^2	311 MΩ μm^2	303	44.5 MΩ μm^2	76.7 MΩ μm^2	72.4
4.0	27.5 GΩ μm^2	108 GΩ μm^2	293	7.13 GΩ μm^2	8.69 GΩ μm^2	21.9

an Ar pressure of 1.2×10^{-3} mbar. The MgO barrier was deposited by rf magnetron sputtering at an Ar pressure of 2.4×10^{-2} mbar. Five wafers with different MgO thickness (t_B) were prepared ($t_B=1.8$, 2.1, 3.0, 4.0, and 5.0 nm). In order to activate the exchange bias of the hard electrode and the partial recrystallization of the electrodes the MTJs were annealed at 350 °C in the presence of a magnetic field (6.5 kOe) in a vacuum furnace with a base pressure of 1×10^{-7} mbar. The junctions with a size of 15×15 and 20×20 μm^2 were patterned by laser lithography and ion-beam etching. The transport properties of the MTJs were measured using the conventional two-probe technique with constant dc bias voltage in a closed cycle helium cryostat (Oxford Cryo drive 1.5) with a temperature range of 13–330 K. We also measured the dielectric stability of the MTJs at room temperature by performing time-dependent voltage ramp experiments.[20,21] At the breakdown voltage U_{BD}, the resistance of the MTJ shows an abrupt decrease because a highly conducting path is irreversibly produced.

The average values and statistical errors of the TMR amplitudes and area resistance products in the parallel state measured at room temperature are 173±5 % and 106 ± 10 kΩ μm^2 for $t_B=1.8$ nm, 167±4 % and 323 ± 18 kΩ μm^2 for $t_B=2.1$ nm, 73.2±4.0 % and 43.4 ± 3.2 MΩ μm^2 for $t_B=3.0$ nm, and 22.5±2.3 % and 6.09 ± 1.04 GΩ μm^2 for $t_B=4.0$ nm. The resistance of the sample with 5.0 nm barrier thickness was just too high (it was estimated to be about 30 TΩ μm^2 at low temperature) to perform reliable TMR measurements.

Structural analysis was carried out by using high-resolution transmission electron microscopy (HRTEM). The HRTEM cross-sectional samples were prepared by conventional focused ion-beam technique with a FEI NOVA NANOLAB 600, which allows sample preparation out of any desired region of our MTJs. The TEM work was done using a Philips CM200-FEG-UT operated at an acceleration voltage of 200 kV.[22]

III. RESULTS AND DISCUSSION

A. Transport properties

The resistance area product in the parallel (antiparallel) magnetic state RA_P (RA_{AP}) and the TMR of typical MTJs acquired at 15 and 300 K with a bias voltage of 5 mV are listed in Table I. These MTJs will be analyzed in detail with respect to their temperature and bias voltage dependence below. Exemplary TMR loops for $t_B=1.8$ and 4.0 nm measured at 15 and 300 K are shown in Fig. 1. The low-temperature TMR is very similar for all barrier thicknesses but the TMR temperature dependence becomes stronger with increasing t_B as can be seen in Fig. 2(b): whereas for $t_B=1.8$ nm the TMR drops from 283% at 15 K to 177% at 300 K, a decrease from 293% down to 21.9% is observed for $t_B=4.0$ nm. For $t_B=3.0$ nm an intermediate behavior (303% at 15 K to 72.4% at 300 K) was found. With respect to the TMR temperature dependence it is worth to note that the reduction in RA products for elevated temperature is always larger for antiparallel than for parallel magnetic state: whereas R^P is reduced by a factor of 1.05 only for $t_B=1.8$ nm between 15 and 300 K, it goes down by a factor of about 12.4 for $t_B=4.0$ nm in the antiparallel state. The low-temperature bias voltage dependence of TMR [see Fig. 2(a)] shows the same trend as the TMR temperature dependence, it becomes much stronger with increasing barrier thickness. Particularly, for $t_B=4.0$ nm the TMR nearly vanishes for bias voltage $|V|\geq500$ mV.

Another hallmark for the junction quality is its dielectric stability under voltage stress. The breakdown voltage listed in Table II increases nearly linearly with barrier thickness as it is expected by the E model.[23] Therefore, the intrinsic dielectric properties of the oxide are conserved at least up to $t_B=5$ nm. Finally, as expected the low-temperature RA product depends exponentially on barrier thickness: by fitting the logarithm of RA_P with a linear function ($\ln[RA_P(t_B)]=\gamma+\alpha t_B$, RA_P given in Ω μm^2) an exponential prefactor of $\alpha=6.1\pm0.2$ nm^{-1} ($\gamma=0.2\pm0.6$) was found which matches quite well with the data of Yuasa et al.[4] ($\alpha=6.41$ nm^{-1}) who deposited their MgO barriers by electron-beam evaporation instead of rf sputtering.

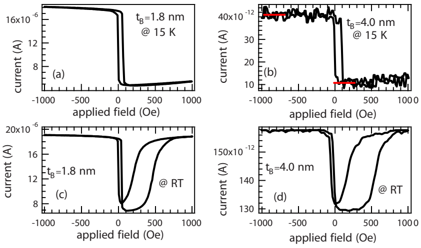

FIG. 1. (Color online) Typical dependence of the current on the applied magnetic field acquired with 5 mV bias voltage measured at 15 and 300 K for $t_B=1.8$ and 4.0 nm.

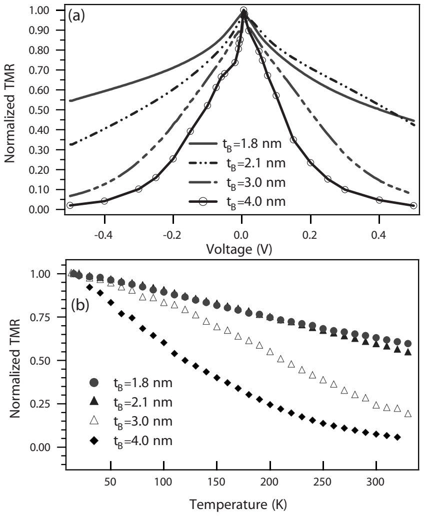

FIG. 2. (a) Typical normalized bias voltage dependence of the TMR for $t_B = 1.8-4.0$ nm measured at 15 K and (b) typical normalized TMR temperature dependence measured with 5 mV bias voltage.

B. Microstructural investigation

To understand the origin for the different bias voltage and temperature dependences for different MgO thickness, microstructural investigations have been performed for $t_B = 2.1$ and 4.0 nm. The transmission electron micrographs of Figs. 3(a) and 3(c) show a good morphology of the MTJ structures with quite smooth interfaces in the overviews. The enlarged HRTEM images in Figs. 3(b) and 3(d) indicate partial crystallization of Co-Fe-B during the postannealing at 350 °C.[24] The MgO tunnel barrier grown on the Co-Fe-B layer showed a good crystalline structure. Moire fringes are observed that point to growth in 5–20 nm sized epitaxial columns with small tilting angles out of plane of the MgO(001)-oriented crystallites.[25] The crystal lattice of the MgO can be clearly identified from the lower interface up to the upper interface for both samples. Therefore, the tunnel barrier and the electrode-barrier interfaces of both junctions seem to be of almost the same quality, which is in accordance with the similar low-temperature/low bias voltage TMR amplitudes of both sample and with the linear barrier thickness dependence of the dielectric breakdown voltage.

TABLE II. Average breakdown voltage U_{BD} (including the statistical error, five MTJs for each barrier thickness) measured at RT in the parallel magnetization state of 225 μm^2 large MTJs for positive bias voltage and a ramp speed of 15 mV/s.

t_B (nm)	U_{BD} (mV)
1.8	1696 ± 13
2.1	1990 ± 15
3.0	2685 ± 20
4.0	3434 ± 22
5.0	4124 ± 38

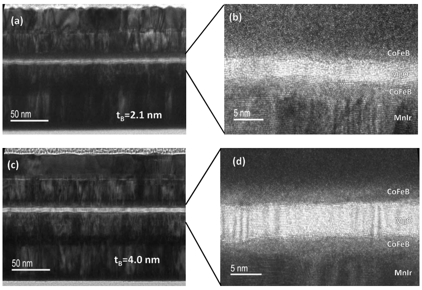

FIG. 3. Transmission electron micrographs of magnetic tunnel junctions. [(a) and (c)] Low magnification image for $t_B = 2.1$ and 4.0 nm. [(b) and (d)] High resolution images for $t_B = 2.1$ and 4.0 nm.

C. Comparison of the experimental data with theoretical models

The bias voltage and temperature dependence of the TMR and the RA products shall now be compared to theoretical models. Drewello et al.[26] extended the magnon-assisted tunneling model developed by Zhang et al.[27] by thermal smearing and applied it successfully to MgO-based MTJs although coherent tunneling is not explicitly taken into account in this model. The motivation for the extension was the very general experimental result, that the temperature dependence of the resistance in the parallel state in MgO-based junction was so small, that the thermal smearing cannot be assumed to be a second-order process any more. This model is the starting point for our data analysis here. The total conductance for a given temperature T and bias voltage V is described as a sum of the contribution from direct elastic tunneling and from magnon-assisted tunneling,

$$G^{\gamma}(V,T) = G^{\gamma}_{\mathrm{dir}}(V,T) + G^{\gamma}_{\mathrm{mag}}(V,T), \qquad (1)$$

where $\gamma = (AP, P)$ describes the magnetic state of the MTJ, $G^{\gamma}_{\mathrm{dir}}(V,T)$ is the direct elastic tunneling conductance and $G^{\gamma}_{\mathrm{mag}}(V,T)$ is the magnon-assisted inelastic conductance. The TMR amplitude is defined as $\mathrm{TMR}(V,T) = [G^{P}(V,T) - G^{AP}(V,T)]/G^{AP}(V,T)$. Taking thermal smearing into account the temperature dependence of the total conductance in the limit of zero bias is then given as

$$G^{\gamma}(0,T) = G^{\gamma}(0,0)\frac{CT}{\sin CT}\left[1 + Q\beta^{\gamma}\ln\left(\frac{k_B T}{E_c}\right)\right]. \qquad (2)$$

C characterizes the strength of the thermal smearing and is related to the effective barrier thickness d (in Å) and the effective barrier height ϕ (in eV) by $C = 1.387\times10^{-4} d/\sqrt{\phi}$. E_c is the low-energy magnon cut-off energy. The parameter β^{γ} is defined as $\beta^{P} = 2Sk_B T\xi/E_m$ and $\beta^{AP} = 2Sk_B T/(\xi E_m)$ for the parallel and the antiparallel magnetic configuration, respectively, with S being the spin parameter and E_m being related to the Curie temperature T_C $[E_m = 3k_B T_C/(S+1)]$ of the ferromagnetic electrode. ξ is the ratio of conductance in both states $\xi = G^{AP}(0,0)/G^{P}(0,0) = R_P(0,0)/R_{AP}(0,0)$. The parameter Q describes the probability that magnons are involved in the tunneling process, it directly depends on the ratio of the squares of the transfer matrix elements for direct (T^d) and magnon-assisted transfer (T^J): $Q = [(|T^d|^2/|T^J|^2) + 2S^2]^{-1}$. The bias voltage dependence of the TMR in the limit of zero temperature is given accordingly as

$$\mathrm{TMR}\,(V,0) = \mathrm{TMR}\,(0,0) - Q\frac{SeV}{E_m}\frac{R_{AP}(0,0)}{R_P(0,0)}\left(\frac{1}{\xi} - \xi\right). \qquad (3)$$

As mentioned above the temperature and bias voltage dependence becomes much stronger with increasing barrier thickness. More precisely it was not possible to fit the data for $t_B = 2.1$, 3.0, and 4.0 nm self-consistently by Eqs. (2) and (3) only. Therefore, we propose to take an additional unpolarized conductance $G_{UP}(V,T)$ (hopping via localized states) into account, which will lead to very reasonable results. A similar ansatz has been proposed by Shang et al.[18] for Al-O-based MTJs. For this, Eq. (1) is amended by an additional term,

$$G^{\gamma}(V,T) = G^{\gamma}_{dir}(V,T) + G^{\gamma}_{mag}(V,T) + G_{UP}(V,T). \qquad (4)$$

In contrast to the TMR it is obvious that the difference $\Delta G(V,T)$ between the total conductance in the parallel and in the antiparallel state is not changed by this additional unpolarized term. In the limit of zero bias it is given by

$$\Delta G(T) = \frac{CT}{\sin CT}\left\{[G^{P}(0,0) - G^{AP}(0,0)] + \frac{2QSk_B}{E_m}T\left[\xi G^{P}(0,0) - \frac{G^{AP}(0,0)}{\xi}\right]\ln\left(\frac{k_B T}{E_c}\right)\right\}. \qquad (5)$$

The self-consistent fitting procedure of our data will now be described. Equation (5) was used to fit $\Delta G(0,T)$ for all four samples *simultaneously* under the constraint that the measured bias voltage dependence of the TMR (average of data for positive and negative bias voltage) for $t_B = 1.8$ nm is reproduced best by Eq. (3) (for this barrier thickness it is known that the magnon-assisted tunneling model can nicely explain the temperature and the bias voltage dependence of the TMR,[26] see also Fig. 4(a). Because of the very similar MgO-barrier interface quality in all junctions (see Sec. III B) the low-energy cut-off energy E_c is expected to be identical for all samples. Furthermore, C is expected to show the mentioned linear dependence on the barrier thickness d and can therefore be rewritten as $C = C'\times d$ with C' being identical for all samples. Furthermore, we use individual values of QS/E_m for all samples to account for a possible thickness dependence of this parameter describing the magnon-assisted processes. The results of the self-consistent fits are summarized in Table III.

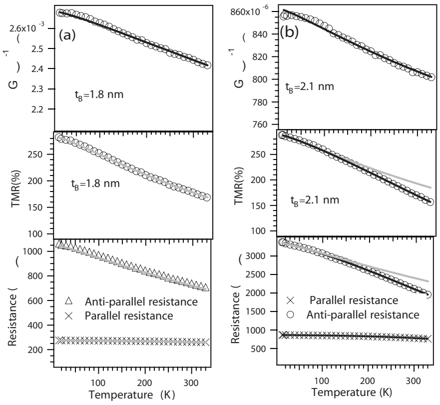

FIG. 4. Typical temperature dependence of ΔG, the TMR, and the resistance for (a) $t_B = 1.8$ nm and (b) 2.1 nm. The junction area is 400 μm^2. The black solid lines are the fits of ΔG according to Eq. (5) and of $R_{P,AP}$ according to Eq. (4). The gray solid lines are the resulting simulations according to Eq. (2), e.g., if only direct and magnon-assisted tunneling would be taken into account.

The fits of Eq. (5) to the experimental $\Delta G(0,T)$ data for $t_B = 1.8$–4.0 nm are shown in the top panels of Figs. 4 and 5. Please note that in contrast to the work by Lu et al.[14] all of our samples show an decreasing $\Delta G(V,T)$ with increasing temperature, we will come back to this below. Finally, please note that the extracted C' value corresponds to a mean barrier height of 4.1 eV which is close to the half of the MgO

TABLE III. Parameters for fitting $\Delta G(0,T)$ by Eq. (5) under the constraint that the bias voltage dependence of the TMR, described by Eq. (3), is reproduced best for $t_B = 1.8$ nm. Technically this was achieved by fixing C' to different values, fitting $\Delta G(0,T)$ for all four samples *simultaneously* and finally checking if the corresponding QS/E_m value for $t_B = 1.8$ nm can reproduce the measured bias voltage dependence of the TMR at low temperature. The best fit of the bias voltage dependence for $t_B = 1.8$ nm and $\Delta G(0,T)$ for all samples was achieved for $C' = 6.85\times10^{5}$ K^{-1} m^{-1}. The corresponding value for the low-energy cut-off energy was $E_c = 0.16 \pm 0.15$ meV.

t_B (nm)	QS/E_m (eV^{-1})
1.8	0.035 ± 0.006
2.1	0.029 ± 0.005
3.0	0.034 ± 0.006
4.0	0.050 ± 0.009

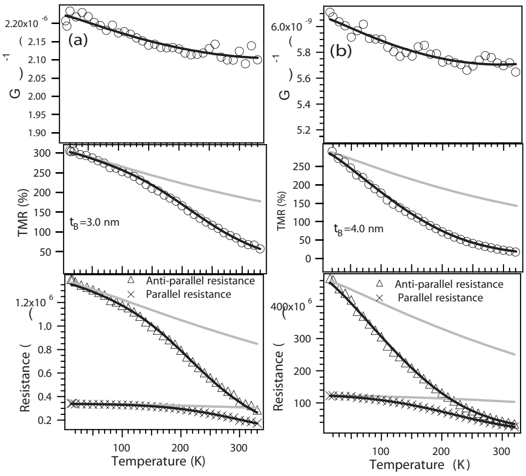

FIG. 5. Typical temperature dependence of ΔG, the TMR, and the resistance for (a) $t_B=3.0$ nm and (b) 4.0 nm. The junction area is 225 μm^2. The black solid lines are the fits of ΔG according to Eq. (5) and of $R_{P,AP}$ according to Eq. (4). The gray solid lines are the resulting simulations according to Eq. (2), e.g., if only direct and magnon-assisted tunneling would be taken into account.

band gap of 7.8 eV.[28] This gives additional support for the self-consistency of our model.

For $t_B=1.8$ nm the fitting parameters given in Table II can be inserted in Eq. (2) to reproduce the total conductance $G^{P,AP}(0,T)$ in the parallel and the antiparallel state very well [see black lines in Fig. 4(a)]. This shows that direct spin-polarized and magnon-assisted tunneling dominates the transport for a barrier thickness of 1.8 nm. For $t_B \geq 2.1$ nm the experimental data for $G^{P,AP}(0,T)$ cannot be reproduced in this way (see gray lines Figs. 4 and 5), an additional temperature-dependent current contribution needs to be taken into account now. Because the magnon-assisted tunneling model can self-consistently reproduce ΔG for all samples, this additional current contribution should be unpolarized. It can be calculated by subtracting $G^{P,AP}(0,T)$ according to Eq. (5) from the experimental data. As expected, these differences are nearly identical for parallel and antiparallel alignment (see Fig. 6). In other words this is the justification for the extra term $G_{UP}(V,T)$ in Eq. (4) and the resulting fits can very well reproduce the observed temperature dependence of the TMR and the area resistance products (see black lines in Figs. 4 and 5). The relative contribution of inelastic unpolarized hopping becomes much more important with increasing barrier thickness, as obvious from Fig. 6(d) showing the typical temperature dependence of $G_{UP}(0,T)$ for $t_B=2.1$, 3.0, and 4.0 nm normalized by $G^P(15\ K)$. This is therefore the reason for the strong decrease in the TMR in these MTJs. In summary, we have shown that the experimental data can be very well explained on the base of direct and magnon-assisted tunneling with an extension by unpolarized hopping conductance. Now we come back to the recent work by Lu et al.[14] They have suggested a spin-polarized extension of the inelastic hopping conductance to explain the temperature dependence of the TMR in Co-Fe-B/MgO/Co-Fe-B MTJs. Their main motivation for the assumption of spin-polarized hopping conductance was the experimental observation that $\Delta G(T)$ increased with increasing temperature for MTJs with 4-nm-thick MgO barrier. We have also applied this model to our data. Details of the procedure can be found in the Appendix. The main results are, that although the temperature-dependent TMR data could be reproduced for all samples quite well, the fit quality for $\Delta G(0,T)$ was worse compared to the extended magnon-assisted tunneling model discussed above. Especially, for $t_B=4.0$ nm the fit showed a significant deviation from the experimental data for $T>240$ K and, furthermore, the extracted spin-wave parameters α were different for all samples. The latter would be in contradiction to our microstructural investigations which showed the same quality of the electrode barrier interface for the different samples and, therefore, one would expect the same magnetic interface properties for the different samples.

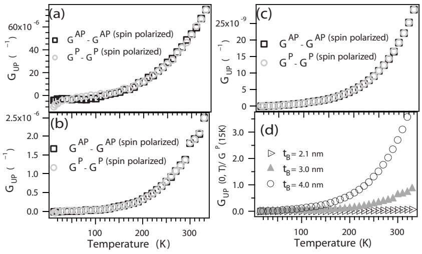

FIG. 6. Typical temperature dependence of $G_{UP}(0,T)$ for (a) $t_B=2.1$ nm, (b) 3.0 nm, and (c) 4.0 nm. The gray circles (black squares) correspond to the calculation starting with conductance in the parallel (antiparallel) state. In (d) the data resulting from $G^P(0,T)$ are shown after normalization by $G^P(15\ K)$.

Therefore our data cannot be described conclusively by the model by Lu et al.[14] Accordingly, the existence of such a polarized conductance channel is not supported by our experiments. On the other hand our model cannot explain the data by Lu et al.[14] because in general magnon-assisted tunneling reduces ΔG with increasing temperature. The difference between the samples is not clear at the moment. Especially, differences in the interface quality may be present because the maximal TMR amplitudes at low temperature are different in the two studies. To decide, whether spin-polarized inelastic hopping is of general importance for MgO-based MTJs or not, further comparative studies by other groups are required.

IV. CONCLUSION

We have investigated structural and transport properties of Co-Fe-B/MgO/Co-Fe-B junctions with a barrier thickness of up to 5 nm. HRTEM investigation on junction with barrier thickness $t_B = 2.1$ and 4.0 nm showed a good crystalline quality of the MgO barrier and the electrode-barrier interface for both junction in accordance with the similar low-temperature TMR amplitudes, with the linear dependence of the dielectric breakdown voltage on the barrier thickness and the expected exponential increase in the resistance area product on the barrier thickness. We have demonstrated that direct spin-polarized and magnon-assisted tunneling can explain the bias voltage and temperature-dependent transport properties for a barrier thickness of 1.8 nm, for increasing barrier thickness this model has been successfully extended by an unpolarized current contribution. This additional unpolarized conductance can describe very well the very strong temperature dependence of the TMR for MTJs with 4-nm-thick MgO barrier, and we have not found any hints to spin-polarized inelastic tunneling as observed by Lu et al.[14]

ACKNOWLEDGMENTS

The authors gratefully acknowledge financial support by the Deutsche Forschungsgemeinschaft (DFG) and the Bundesministerium für Bildung und Forschung (BMBF). Ayaz Arif Khan acknowledges financial support by the University of Azad Jammu & Kashmir Muzaffarabad (Pakistan). Some of the authors (G.E., M.M., H.S., and M.S.) gratefully acknowledge financial support by the Sonderfoschungsbereich SFB-602.

APPENDIX

In the following we describe the application of the model by Lu et al.[14] to our data. This model is based on the spin conserving hopping transport through chains of N LSs. The first step was to fit the conductance in the antiparallel state by a function of the form

$$G_{AP}(0,T) = \sigma_0 + \sum_{N\geq 2}^{N_{max}} \sigma_N T^{N-2/(N+1)}. \qquad (A1)$$

The parameters σ_N describing the contribution of hopping via N localized states to $G_{AP}(0,T)$ were used as free parameters. For $t_B = 1.8$ and 2.1 nm the data could be fitted by taking chains up to $N=2$ and $N=3$, respectively. For $t_B = 3.0$ nm and 4.0 nm higher-order hopping chains were required: for this we have adopted the fitting procedure as Xu et al.,[17] i.e., first we restricted the fit to a temperature range that could be fitted best by taking chains up to $N=2$ only into account. Then the temperature range has been increased so far that it can be best fitted by a function with one additional term and so on. By doing this the data for $t_B = 3.0$ and 4.0 nm in the entire temperature range up to 330 K were fitted with a function containing terms up to $N=6$ and $N=7$, respectively. Exemplary results for $t_B = 1.8$ and 4.0 nm are shown in Figs. 7(c) and 7(d). The according relative contribution W_N of different N-LS chains to the antiparallel conductance are shown in Figs. 7(a) and 7(b). Please note that resonant tunneling $(N=1)$ is expected to be T independent and can therefore not be distinguished from direct tunneling $(N=0)$. In this sense the parameter σ_0 must be interpreted as an average value for direct and resonant tunneling.

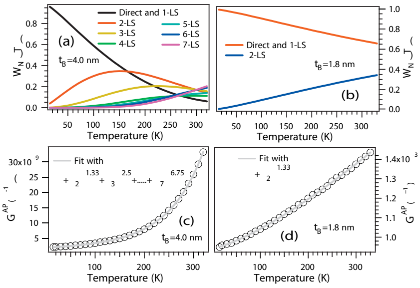

FIG. 7. (Color) Temperature dependence of the tunnel conductance in antiparallel state for (c) $t_B = 4.0$ nm and (d) 1.8 nm and relative contribution W(N) of the different N-LS chains to the antiparallel conductance for (a) $t_B = 4.0$ nm and (b) 1.8 nm.

The expression for $\Delta G(0,T)$ due to the activation of spin conserving inelastic hopping through chains of N localized state at zero bias is given by

TABLE IV. Parameters for fitting $\Delta G(0,T)$ of all samples simultaneously by Eqs. (A2) and (A3). The best simultaneous fits were achieved for $C' = 4.0 \times 10^5$ K^{-1} m^{-1}.

t_B (nm)	P_0	α (K$^{-3/2}$)
1.8	0.7658 ± 0.0004	$5.71 \times 10^{-6} \pm 1.9 \times 10^{-7}$
2.1	0.7681 ± 0.0004	$4.54 \times 10^{-6} \pm 1.8 \times 10^{-7}$
3.0	0.7799 ± 0.0004	$6.85 \times 10^{-6} \pm 1.7 \times 10^{-7}$
4.0	0.7796 ± 0.0004	$1.86 \times 10^{-5} \pm 2.0 \times 10^{-7}$

$$\Delta G(0,T) = \sigma_0 \frac{CT}{\sin CT} \mathrm{TMR}_0 + \sum_{N \geq 1}^{N_{max}} \sigma_N T^{N-2/(N+1)} \mathrm{TMR}(N,T) \tag{A2}$$

and the TMR(N,T) assigned to a different variety of chains is given as

$$\mathrm{TMR}(N,T) = \frac{(1+P)^{2\beta_N} + (1-P)^{2\beta_N}}{2(1-P^2)^{\beta_N}} - 1 \tag{A3}$$

with $\beta_N = 1/N+1$ and a T-dependent effective spin polarization $P = P_0(1-\alpha T^{3/2})$, α is the spin-wave parameter related to the interfacial Curie temperature and P_0 is the effective spin polarization at $T=0$ K. The total temperature dependent TMR (T) is then given as the sum of TMR(N,T) weighted by their fractional contribution W_N,

$$\mathrm{TMR}(T) = \sum_N W_N(T) \times \mathrm{TMR}(N,T). \tag{A4}$$

Then we fitted the data of all four samples simultaneously by using Eqs. (A2) and (A3), whereas the spin-wave parameters α and the polarizations P_0 were considered as free parameters, and the thermal smearing was taken into account by $C = C' \times d$ with keeping C' identical for all samples. The resulting parameters for $t_B = 1.8 - 4.0$ nm are given in Table IV, Fig. 8 shows exemplary results for sample A and D. Although the fitting parameters in Table IV can reproduce the temperature-dependent TMR data for all four samples quite well, the fit quality for $\Delta G(0,T)$ was not in all cases as satisfying as by fitting the data by the extended magnon-assisted tunneling model (see Sec. III C). Particularly, for $t_B = 4.0$ nm the fit showed a rising trend of $\Delta G(0,T)$ for T > 240 K. Second, the spin-wave parameters α being related to the temperature dependence of the interfacial magnetization and polarization seemed to be different for all samples. But this would be in contradiction to our microstructural investigations which showed the same quality of the electrode barrier interface for junctions with thin and thick barriers.

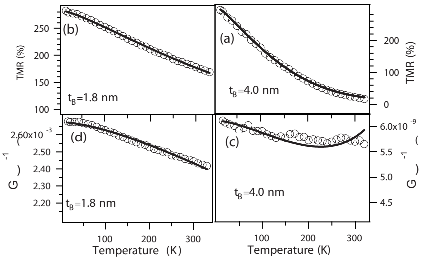

FIG. 8. Typical temperature dependence of $\Delta G(0,T)$ for (c) $t_B = 4.0$ nm and (d) 1.8 nm, the black lines represent fits using Eqs. (A2) and (A3). The black solid lines represent the computed values of TMR (T) for (a) $t_B = 4.0$ nm and (b) 1.8 nm by inserting the parameters listed in Table IV into Eq. (A4).

---

*jschmalh@physik.uni-bielefeld.de
[1] S. A. Wolf, D. D. Awschalom, R. A. Buhrman, J. M. Daughton, S. von Molnar, M. L. Roukes, A. Y. Chtchelkanova, and D. M. Treger, Science 294, 1488 (2001).
[2] M. Julliere, Phys. Lett. A 54, 225 (1975).
[3] S. S. P. Parkin, C. Kaiser, A. Panchula, P. M. Rice, B. Hughes, M. Samant, and S.-H. Yang, Nature Mater. 3, 862 (2004).
[4] S. Yuasa, T. Nagahama, A. Fukushima, Y. Suzuki, and K. Ando, Nature Mater. 3, 868 (2004).
[5] D. D. Djayaprawira, K. Tsunekawa, M. Nagai, H. Maehara, S. Yamagata, N. Watanabe, S. Yuasa, Y. Suzuki, and K. Ando, Appl. Phys. Lett. 86, 092502 (2005).
[6] Y. M. Lee, J. Hayakawa, S. Ikeda, and H. Ohno, Appl. Phys. Lett. 90, 212507 (2007).
[7] S. Ikeda, J. Hayakawa, Y. Ashizawa, Y. M. Lee, K. Miura, H. Hasagawa, M. Tsunoda, F. Matsukura, and H. Ohno, Appl. Phys. Lett. 93, 082508 (2008).
[8] W. H. Butler, X.-G. Zhang, T. C. Schulthess, and J. M. MacLaren, Phys. Rev. B 63, 054416 (2001).
[9] J. Mathon and A. Umerski, Phys. Rev. B 63, 220403 (2001).
[10] S. Yuasa, Y. Suzuki, T. Katayama, and K. Ando, Appl. Phys. Lett. 87, 242503 (2005).
[11] Y. S. Choi, K. Tsunekawa, Y. Nagamine, and D. Djayaprawira, J. Appl. Phys. 101, 013907 (2007).
[12] J. Y. Bae, W. C. Lim, H. J. Kim, T. D. Lee, and T. W. Kimm, J. Appl. Phys. 99, 08T316 (2006).
[13] J. Schmalhorst, A. Thomas, G. Reiss, X. Kou, and E. Arenholz, J. Appl. Phys. 102, 053907 (2007).
[14] Y. Lu, M. Tran, H. Jaffres, P. Seneor, C. Deranlot, F. Petroff, J. M. George, B. Lepine, S. Ababou, and G. Jezequel, Phys. Rev. Lett. 102, 176801 (2009).
[15] J. C. Read, P. G. Mather, and R. A. Buhrman, Appl. Phys. Lett. 90, 132503 (2007).
[16] G. X. Miao, Y. J. Park, J. S. Moodera, M. Seibt, G. Eilers, and M. Münzenberg, Phys. Rev. Lett. 100, 246803 (2008).
[17] Y. Xu, D. Ephron, and M. R. Beasley, Phys. Rev. B 52, 2843 (1995).
[18] C. H. Shang, J. Nowak, R. Jansen, and J. S. Moodera, Phys. Rev. B 58, R2917 (1998).
[19] J. Zhang and R. M. White, J. Appl. Phys. 83, 6512 (1998).
[20] A. A. Khan, J. Schmalhorst, A. Thomas, O. Schebaum, and G. Reiss, J. Appl. Phys. 103, 123705 (2008).
[21] A. A. Khan, J. Schmalhorst, A. Thomas, V. Drewello, and G. Reiss, J. Appl. Phys. 105, 083723 (2009).
[22] A. Thomas, V. Drewello, M. Schäfers, A. Weddemann, G. Reiss, G. Eilers, M. Münzenberg, K. Thiel, and M. Seibt, Appl. Phys. Lett. 93, 152508 (2008).
[23] J. W. McPherson and H. C. Mogul, J. Appl. Phys. 84, 1513 (1998).
[24] G. Eilers, H. Ulrichs, M. Münzenberg, A. Thomas, K. Thiel, and

---

M. Seibt, J. Appl. Phys. 105, 073701 (2009).
[25] G. X. Miao, J. Y. Chang, M. J. van Veenhuizen, K. Thiel, M. Seibt, G. Eilers, M. Münzenberg, and J. S. Moodera, Appl. Phys. Lett. 93, 142511 (2008).
[26] V. Drewello, J. Schmalhorst, A. Thomas, and G. Reiss, Phys. Rev. B 77, 014440 (2008).
[27] S. Zhang, P. M. Levy, A. C. Marley, and S. S. P. Parkin, Phys. Rev. Lett. 79, 3744 (1997).
[28] R. C. Whited, C. J. Flaten, and W. C. Walker, Solid State Commun. 13, 1903 (1973).